

# Analysis of Magnetic Gear End-Effects to Increase Torque and Reduce Computation Time

Thesis

Presented in Partial Fulfillment of the Requirements for the Degree  
Master of Science in the Graduate School of The Ohio State  
University

By

Bradley Losey, B.S.

Graduate Program in Department of Mechanical Engineering

The Ohio State University

2020

Thesis Committee:

Professor Marcelo Dapino, Advisor

Professor Rebecca Dupaix

© Copyright by

Bradley Losey

2020

## Abstract

Magnetically geared machines perform gearing operations by utilizing magnetic force interactions between the rotors as opposed to mechanical force interactions. Many benefits of magnetic gears derive from the fact that there is no contact between the rotors. Contactless gearing allows for quieter operation, eliminates the need for lubrication outside the bearings, decreases the need for maintenance, and provides inherent overload protection. Another benefit is that the magnetic gear design lends itself to direct implementation in motors as opposed to having a separate mechanical gearbox. A magnetic gear has three fundamental components: a high speed rotor, a low speed rotor, and a flux modulator. These components work in tandem to generate magnetic field harmonics which scale the torque and speed of the input shaft. There are many magnetic gear designs that accomplish this task, but this thesis focuses on coaxial magnetic gears (CMGs) that utilize Halbach array magnet rotors and no back iron. In this design, the flux modulator is radially nested within the low and high speed rotors with the high speed rotor typically positioned at the inner most layer.

Inherent to magnetic gear behavior is a 3D inefficiency known as end-effect loss. This loss causes flux to leak over the axial ends of the gear and back to its source. This flux never makes it to the flux modulator and never contributes to torque. End-effect losses can cause a significant decrease in output torque (10% to 40% depending on the design) and can only be modeled with large 3D simulations.

The first aspect of this research involves the development of a reduced length modeling method which accounts for the axial variation of end-effect losses within the gear to shorten the computation time of magnetic gearing models. It has been shown for the models in this thesis that computation time can be cut in half while the torque results stay within 5% of their true value. Several magnetic gear design variables have been correlated to the severity of end-effect losses to guide general implementation of the modeling technique to CMGs.

The second aspect involves the creation of a novel magnetic gear design for the purpose of mitigating end-effect losses. This cladding magnet-coaxial magnetic gear (CM-CMG) utilizes axially oriented magnets on the axial ends of the gear to mitigate flux leakage over the ends of the gear. It has been found that a CM-CMG can generate up to 12.4% more torque than an equally massive CMG design. Theory has been developed to guide the application of cladding magnets to general CMG designs.



## Acknowledgments

I would like to start off by thanking my advisor Professor Marcelo Dapino and Professor Rebecca Dupaix for serving on my committee. Thank you to Professor Dapino for providing me with both the opportunity to work in the SMSL lab and also the guidance to navigate my engineering studies and research. Including undergraduate research, I have now worked in the lab for over five years, and the experience I've gained during these five years has been invaluable. The difference in my understanding of engineering principles, technical communication, and professional relationships is night and day from when I first started, and much of that development can be directly attributed to Professor Dapino's mentorship.

I would also like to thank the graduate researchers that I worked for as an undergraduate. The counsel and patience given to me by Matt Scheidt when I was first beginning work in the lab will always be appreciated. I knew nearly nothing about electromagnetics before meeting Zhangxian Deng (Dan), but thankfully he was patient enough to teach me. Dan was an incredible example of a hard working graduate student, and I am very grateful to have had him as a role model.

Thank you to Ismail Nas and Martin Moore for being great magnetic gearing teammates. Ismail has been an invaluable resource for letting me know when I'm

making no sense and then telling me how to make sense. Your friendship and chauffeuring skills are always appreciated. Thank you to my labmates and a special thank you to Yitong for chipping in to drive me to and from work after my knee surgery.

I want to give a big thank you to the NASA team who sponsors our research. Vivake, Justin, Zac, and Tom have all been great mentors, and it's been a lot of fun working with you both at Ohio State and up in Cleveland. A special thank you to Vivake for igniting my passion for research.

Finally, I'd like to acknowledge the support of my friends and family. Collin, Destiny, Humza, and many more that I don't have space to name have been an incredible support network throughout graduate studies. Thank you to Collin for not getting upset that the dirty dishes have piled up while I've been writing this thesis. To my grandparents, parents, and brothers, I'll forever be indebted to you for your unconditional love and support.

## Vita

May 16, 1995 ..... Born - Akron, USA

2018 ..... B.S. Aeronautical and Astronautical  
Engineering,  
The Ohio State University.

2018-present ..... Graduate Research Associate,  
The Ohio State University.

## Fields of Study

Major Field: Department of Mechanical Engineering

Studies in Magnetic Gearing: Professor Marcelo Dapino

# Table of Contents

	Page
Abstract . . . . .	ii
Acknowledgments . . . . .	iv
Vita . . . . .	vi
List of Tables . . . . .	x
List of Figures . . . . .	xi
1. Introduction . . . . .	1
1.1 Magnetic Gearing . . . . .	2
1.1.1 Motivation . . . . .	2
1.1.2 Principles of Operation . . . . .	5
1.2 Principles of Static Magnetism . . . . .	10
1.3 Halbach Arrays . . . . .	13
1.3.1 Linear Array . . . . .	13
1.3.2 Halbach Cylinder . . . . .	15
1.4 End Effects . . . . .	16
1.4.1 Leakage . . . . .	17
1.4.2 Fringing . . . . .	18
1.4.3 Escaping . . . . .	18
1.5 Objectives . . . . .	19
1.5.1 Reduce Computation Time . . . . .	19
1.5.2 Increase Specific Torque . . . . .	19
1.6 Thesis Organization . . . . .	20

2.	COMSOL Model Summary . . . . .	21
2.1	COMSOL FEM Theory . . . . .	21
2.2	Physical/Geometric Features . . . . .	23
2.2.1	Symmetry . . . . .	24
2.2.2	Axial Air Domain . . . . .	27
2.2.3	Magnetic Considerations . . . . .	29
2.3	Mesh Summary . . . . .	30
2.4	Modeling Verification and Validation . . . . .	34
2.4.1	Gear Ratio Check . . . . .	35
2.4.2	Pseudo 2D Model . . . . .	35
2.4.3	Experimental Validation . . . . .	37
3.	Reduced Length Modeling of Magnetic Gears . . . . .	38
3.1	Reduced Length Modeling Theory . . . . .	38
3.2	Variable Sensitivity . . . . .	43
3.2.1	Axial Length . . . . .	45
3.2.2	Magnetic Air Gap Thickness . . . . .	48
3.2.3	Outer Radius . . . . .	57
3.2.4	Pole-Pair Scaling Factor . . . . .	65
3.3	Reduced Length Modeling Application . . . . .	71
3.3.1	PT-1 Time Savings and Error . . . . .	72
3.3.2	Modified PT-1 Time Savings and Error . . . . .	73
3.4	Discussion . . . . .	76
3.4.1	Summary of Results . . . . .	76
3.4.2	General Application of Findings . . . . .	77
4.	Cladding Magnet-Coaxial Magnetic Gear Design . . . . .	79
4.1	Cladding Magnet Theory . . . . .	79
4.2	Variable Sensitivity . . . . .	82
4.2.1	Height . . . . .	85
4.2.2	Depth . . . . .	86
4.2.3	Tilt . . . . .	90
4.2.4	Miscellaneous Variables . . . . .	93
4.3	Cladding Magnet Designs . . . . .	95
4.3.1	PT-1 Iteration 1 . . . . .	96
4.3.2	PT-1 Iteration 2 . . . . .	98
4.3.3	PT-5 . . . . .	100
4.4	Discussion . . . . .	103

4.4.1	Summary of Results . . . . .	103
4.4.2	General Application of Findings . . . . .	104
5.	Concluding Remarks . . . . .	105
5.1	Conclusions . . . . .	105
5.2	Future Work . . . . .	107
	Appendices	110
A.	Caged Flux Modulator . . . . .	110
B.	1000 Gear Ratio Magnetic Gear . . . . .	114
C.	COMSOL Tutorial: Magnetic Gears . . . . .	124
	Bibliography . . . . .	145

## List of Tables

Table	Page
2.1 Torque results for PT-4 model variations. . . . .	37
2.2 Current COMSOL and experimental torque results for all NASA PTs. . . . .	37
3.1 Design and performance characteristics for the NASA PT-1. . . . .	45
4.1 Torque results for the PT-1 CM-CMG when tilt of the inner and outer rotors are decoupled. . . . .	92
4.2 Torque results for the PT-1 CM-CMG when cladding magnets are divided into an upper and lower magnet with distinct tilt angles. . . . .	95
4.3 Design and performance characteristics for the PT-1 Iteration 1 CM-CMG. . . . .	98
4.4 Design and performance characteristics for the PT-1 Iteration 2 CM-CMG. . . . .	99
4.5 Design and performance characteristics for the NASA PT-5. . . . .	100
4.6 Design and performance characteristics for the PT-5 CM-CMG. . . . .	103
A.1 Torque results for various caged modulator geometries as compared to the baseline PT-3. . . . .	112
B.1 Torque and approximate length results for the 1000 gear ratio trials. . . . .	116
B.2 FFT amplitude results for the outer rotor magnets at the inner air gap. . . . .	121
B.3 Design and performance characteristics for each stage of a 1000 gear ratio, 50 N*m output torque magnetic gear. . . . .	123

## List of Figures

Figure		Page
1.1	Fundamental magnetic gear components and an illustration of the coordinate system to be used. The origin of the coordinate system is the center of the gear. . . . .	2
1.2	(a) Mechanical spur gear with teeth that transfer rotation via mechanical force; (b) magnetic spur gear with pole-pairs that transfer rotation via magnetic force. . . . .	6
1.3	A 4 pole-pair outer rotor, 1 pole-pair inner rotor configuration is shown: (a) If the iron pieces are aligned with the south poles then the modulated flux is of south orientation; (b) if the iron pieces are aligned with the north poles then the modulated flux is of north orientation; (c) realistic representation of a flux modulator where the modulated flux is spatially periodic with the frequency of the opposite rotor. . . . .	7
1.4	(a) Mechanical planetary gear system; (b) equivalent components of a CMG. . . . .	9
1.5	Electrical-magnetic circuit analogy. . . . .	10
1.6	(a) Halbach array with four magnets per pole-pair offset at 90° angles; (b) Halbach array with six magnets per pole-pair offset at 60° angles; (c) Halbach array with eight magnets per pole-pair offset at 45° angles. . . . .	14
1.7	A Halbach cylinder with four pole-pairs and four magnets per pole-pair. . . . .	15
1.8	A cross-section of a magnetic gear which shows the flux paths for both leaking and fringing which cause decreased flux density at the rotors and flux modulator. Only flux from the outer rotor is shown, but equivalent paths exist for the inner rotor. . . . .	17



2.1	Central x-y plane of symmetry shown on a radial cut plane. . . . .	25
2.2	An axis of symmetry for a magnetic gear with angular periodicity. . .	26
2.3	Boundary orientation for the source boundary on the left and the destination boundary on the right. . . . .	27
2.4	Convergence study on the necessary length of the axial air domain for accurate modeling of end-effects. The maximum length is 1.5" (38.1 mm). . . . .	28
2.5	Nonlinear B-H curve for 0.01" (0.254 mm) HF-10 electrical steel laminate. The red arrow indicates around where magnetic saturation begins to occur. . . . .	29
2.6	Standard mesh refinement for a 2D magnetic gear model. The air gap is highlighted in blue. . . . .	31
2.7	Convergence of output torque as mesh resolution of the air gaps becomes finer. . . . .	32
2.8	Convergence of the simulated gear ratio as compared to the theoretical gear ratio when air gap element size is decreased. The theoretical gear ratio is 4.25. . . . .	33
2.9	(a) Mesh close-up showing stage 1 of the meshing process that defines the air gaps; (b) full mesh that has been filled in by stage 2. . . . .	34
2.10	Generic pseudo 2D model with no axial air domain. The magnetically active components are highlighted in blue. . . . .	36
3.1	Sections of the magnetic gear that are estimated by each step of the reduced length modeling method. The two symmetric sections that experience end-effects in the first step are brought together to create a symmetric reduced length 3D model. . . . .	39
3.2	Flux density profile that displays the constant linear region and the decreasing nonlinear region. Radial flux density of the outer air gap is shown, but this trend exists to some extent at all locations for both radial and tangential flux density. . . . .	40

3.3	Example of the computation time scaling trend as the size or mesh refinement of a magnetic gear model is increased. This plot was created using the default COMSOL solver and fixed computational resources.	41
3.4	Cross-sectional geometry for NASA's PT-1 magnetic gear design. All magnetically active components are highlighted in blue. . . . .	44
3.5	Scaling of output torque for 2D and 3D models per unit of axial length modeled up to 2" (50.8 mm). . . . .	46
3.6	End-effect factor scaling of a coaxial magnetic gear as the axial length is increased. . . . .	48
3.7	Comparison of the standard PT-1 flux density profile to a version of PT-1 that has 1.5x thicker air gaps. . . . .	50
3.8	Contour of the magnetic flux density norm shown on an axial cross section of the original PT-1. . . . .	51
3.9	Contour of the magnetic flux density norm shown on an axial cross section of a modified PT-1 with 1.5x thicker magnetic air gaps. . . . .	52
3.10	Scaling of output torque for 2D and 3D models as the inner and outer magnetic air gaps are equally scaled. . . . .	53
3.11	Scaling of the end-effect factor as the inner and outer magnetic air gaps are equally scaled. . . . .	54
3.12	(a) Original square magnets used for PT-1; (b) modified curved magnets used for scaling analysis. . . . .	55
3.13	Comparison of torque results for 2D and 3D models when using square vs curved magnets. . . . .	55
3.14	Comparison of end-effect factor results for 2D and 3D models when using square vs curved magnets. . . . .	56
3.15	Average radius of the flux modulator and slip force of the flux modulator shown to conceptualize the elements that contribute to output torque. . . . .	58

3.16	Illustration of how the magnetic gear radius is scaled. The outer radius of the outer rotor is varied while the component and air gap thicknesses are kept fixed. . . . .	60
3.17	2D and 3D torque results as the outer radius of the gear was scaled with no change to pole-pair number. . . . .	61
3.18	End-effect factor results as the outer radius of the gear was scaled with no change to pole-pair number. . . . .	62
3.19	(a) Discretized magnet geometry for one of the radius model; (b) non-discretized magnet geometry for the same radius model; (c) flux lines associated with “a”; (d) flux lines associated with “b”. . . . .	63
3.20	2D and 3D torque results for magnetic gears with discretized and non-discretized Halbach arrays. . . . .	64
3.21	End-effect factor results for magnetic gears with discretized and non-discretized Halbach arrays. . . . .	65
3.22	All magnetically active components are highlighted in blue; (a) Base model for the following pole-pair trials with 2 inner rotor pole-pairs and 8 outer rotor pole-pairs (4 magnets per pole-pair); (b) pole-pair model with a pole-pair scaling factor of 2. The model has 4 inner rotor pole-pairs and 16 outer rotor pole-pairs. . . . .	66
3.23	2D and 3D torque results as the pole-pair scaling factor of the gear was varied with no change to any radii or thicknesses. . . . .	67
3.24	End-effect factor results as the pole-pair scaling factor of the gear was varied with no change to any radii or thicknesses. . . . .	69
3.25	2D and 3D torque results for magnetic gears with discretized and non-discretized Halbach arrays as pole-pair scaling factor was varied. . . .	70
3.26	End-effect factor results for magnetic gears with discretized and non-discretized Halbach arrays as pole-pair scaling factor was varied. . . .	71

3.27	Illustration of the torque summation used for the reduced length scaling method. The plot is for a gear with a base axial length of 1.0" (25.4 mm). . . . .	73
3.28	Scaling of percent error and computation time as reduced 3D model length is varied for a magnetic gear that had an original axial length of 1.0" (25.4 mm). . . . .	74
3.29	Illustration of the torque summation used for the reduced length scaling method. The plot is for a gear with a base axial length of 2.0" (50.8 mm). . . . .	75
3.30	Scaling of percent error and computation time as reduced 3D model length is varied for a magnetic gear that had an original axial length of 2.0" (50.8 mm). . . . .	76
4.1	Representation of the cladding magnet capping effect. The red lines show the flux path from the outer rotor magnet. . . . .	80
4.2	Radial cross-section of a CM-CMG. The three variables shown were the variables determined to be the most consequential to torque production. . . . .	82
4.3	Top view of the Halbach array cladding magnet orientations. . . . .	83
4.4	Illustration of the length adjustment made to the standard gear portion to make mass constant. . . . .	84
4.5	Radial cross-section with height and depth highlighted. . . . .	86
4.6	Specific torque as height ratio and depth are varied. The red line highlights the height ratio scaling trend. Maximum specific torque occurs at a height ratio of 50% and a depth of 0.2" (5.08 mm). . . . .	87
4.7	Specific torque as inner and outer cladding magnet depths are varied. Torque would show the same trend because mass is constant. Maximum specific torque occurs at an inner depth of 0.22" (5.59 mm) and an outer depth of 0.2" (5.08 mm). . . . .	88
4.8	Specific torque results as depth is swept for magnetic gears of different base lengths. Base length is varies from 0.5" (12.7 mm) to 3.0" (76.2 mm) and optimal varies from 0.16" (4.06 mm) to 0.22" (5.59 mm). . . . .	89

4.9	Radial cross-section with tilt highlighted. . . . .	91
4.10	Progression of Halbach structures that incorporate increasing variation of magnetization vectors. . . . .	92
4.11	(a) Output torque of a CM-CMG as tilt is varied; (b) a close-up of “a” showing that there is very little difference in output torque around 45°. . . . .	93
4.12	Radial cross-section to display offset. . . . .	94
4.13	Radial cross-section to display $Tilt_1$ and $Tilt_2$ . . . . .	95
4.14	Top view of the PT-1 iteration 1 CM-CMG. The cladding magnets are highlighted in blue. . . . .	96
4.15	Top view of the PT-1 iteration 2 CM-CMG. The cladding magnets are highlighted in blue. . . . .	99
4.16	Top view of the PT-5 CM-CMG. The cladding magnets are highlighted in blue. . . . .	101
4.17	Depth trials performed for PT-5 CM-CMG that eventually converge on the depth of maximum specific torque. Optimal depth occurs around 0.09” (2.29 mm). . . . .	102
A.1	(a) Front view of a standard flux modulator; (b) front view of a caged flux modulator. The modulator material is highlighted in blue while the structural material is colored gray. Only one axial half of the gear is shown. . . . .	111
A.2	Design variables that define the caged modulator geometry. . . . .	112
B.1	Four COMSOL trials are run for a magnetic gear with a gear ratio of 1000. Each trial has a different outer diameter. . . . .	115
B.2	A close-up on the mesh of Trial D. The magnetically active components are highlighted in blue. . . . .	116
B.3	Location of the flux density measurement and the source of interest. . . . .	117

B.4	Radial and tangential flux density waveforms at the inner air gap of Trial A. . . . .	118
B.5	FFT for the radial flux density waveform of Trial A. . . . .	118
B.6	FFT for the tangential flux density waveform of Trial A. . . . .	119
B.7	Radial and tangential flux density waveforms at the inner air gap of Trial D. . . . .	120
B.8	FFT for the radial flux density waveform of Trial D. . . . .	120
B.9	FFT for the tangential flux density waveform of Trial D. . . . .	121
B.10	Torque and angular velocity behavior for a multi-stage magnetic gear with a gear ratio of 1000 that produces 50 N*m of output torque. . .	122
C.1	The tree that defines all geometric, physical, mesh, solver, and post-processing characteristics of a COMSOL magnetic gear model. . . . .	124
C.2	Parameter tab where magnetic gear design parameters are defined. . .	125
C.3	Explicit definition of “All magnets”. . . . .	126
C.4	Explicit definition of the “Input torque” region. . . . .	127
C.5	Explicit definition of the “Output torque” region. . . . .	127
C.6	Definition of a Cartesian boundary system. . . . .	128
C.7	Command to create a circular array of flux modulator pieces. “Resulting objects selection” is checked to make the resulting object selectable in the material and physics sections. . . . .	129
C.8	The entire simulation is initially defined as air. . . . .	130
C.9	The flux modulator material is assigned to the flux modulator using the selection defined in the “Geometry tab”. This overrides the initial air definition. . . . .	131
C.10	The B-H curve for flux modulator material is defined using a local table.	131

C.11 The out-of-plane thickness and dependent variable discretization scheme is defined. . . . .	132
C.12 Ampère’s Law is set for the permanent magnets using a remanent flux density vector. . . . .	133
C.13 Ampère’s Law is set for the flux modulator pieces using the specified H-B curve. . . . .	134
C.14 Torque is calculated at the “Output torque” selection. . . . .	134
C.15 A continuous periodic boundary condition is defined for a magnetic gear.	135
C.16 The destination boundary is explicitly defined and set to use a boundary system with a reversed normal. . . . .	135
C.17 A mesh is defined on the source boundary and copied to the destination boundary. . . . .	136
C.18 Tetrahedral mesh resolution is defined for the air gaps. . . . .	137
C.19 A tetrahedral mesh is defined for the rest of the model geometry. . . .	137
C.20 Statistics of “Compile Equations: Stationary” which show the model DOFs. . . . .	138
C.21 Parametric sweep of tilt for Study 1. . . . .	139
C.22 Global evaluation of input and output torque as defined in the physics section. . . . .	140
C.23 Geometric locations of interest that have been defined for post-processing.	141
C.24 Arrow surface of a plane to visualize flux lines. . . . .	142
C.25 Line graph of flux components at the periodic boundary condition. . . .	142
C.26 Boundary systems used at the source and destination faces of the periodic boundary condition. . . . .	143

C.27 Export feature used to extract raw data from the COMSOL simulation. 144



## Chapter 1: Introduction

This chapter includes:

- An introduction to the field of magnetic gearing and an explanation of how they work
- A basic overview of magnetic theory that will be helpful in understanding concepts presented in this thesis
- An explanation of Halbach structures and their relevance to magnetic gears
- An overview of the types of end-effects and how they affect flux density
- Objectives for this thesis's contribution to the field of magnetic gearing
- A summary of the thesis structure

Make note that this thesis always refers to torque in Metric units because the  $\text{N}\cdot\text{m}$  is the universally accepted unit for magnetic gear torque; however, units of length are referred to as either English or Metric depending on which is native. When a length unit is mentioned in the text, both English and Metric variations are given with the non-native unit in parenthesis. Figures only include the native length unit.

## 1.1 Magnetic Gearing

The contribution of this thesis is to the field of magnetic gearing. As such, Figure 1.1 has been included to introduce the most fundamental components of a common magnetic gear design and to show the coordinate system that will be used. These

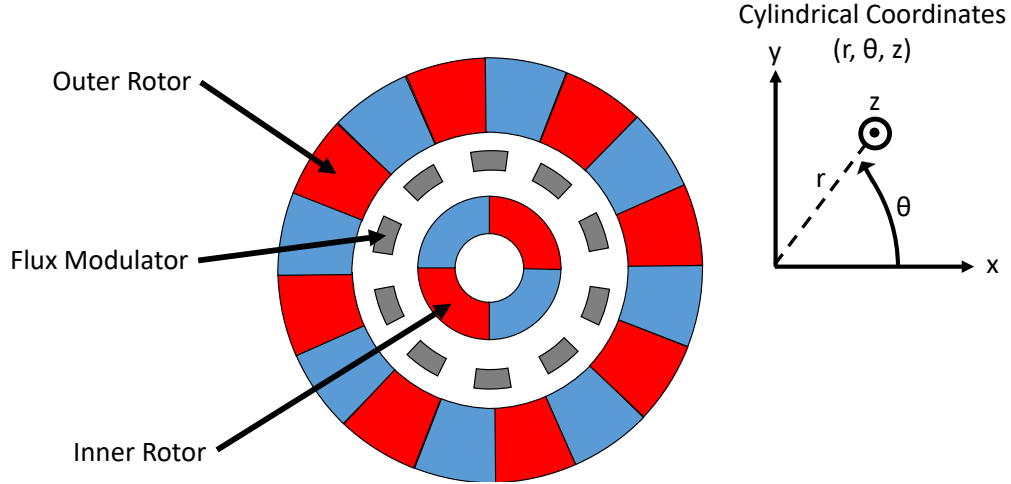


Figure 1.1: Fundamental magnetic gear components and an illustration of the coordinate system to be used. The origin of the coordinate system is the center of the gear.

components will be frequently referred to throughout the thesis and will be explained more rigorously in 1.1.2. The cylindrical coordinate system will often be used to describe locations and vector orientations.

### 1.1.1 Motivation

The need for magnetic gearing has largely emerged as a result of mechanical gearing deficiencies when applied to modern aerospace challenges. For example, short-range electrical aircraft are a budding field in the aerospace industry, but the noise

and maintenance of the mechanical gears in these aircraft are a major obstacle in the way of actualizing this technology commercially [26]. Many cities have strict noise pollution requirements that prove difficult to meet while using traditional aircraft designs that utilize mechanical gearing. Magnetic gears have the potential to be quieter than mechanical gears because the only physical contact between the rotors takes place at the bearings.

Another benefit derived from this minimal contact is that there is no need for transmission fluid to lubricate the contact between gear teeth. This is of particular interest for space applications as transmission fluid does not operate well in zero gravity conditions. Other advantages to contact-less gearing include inherent overload protection and increased operational reliability. Improvements to reliability mean that magnetic gears have the potential to require less maintenance than traditional mechanical gears. Superior reliability has made magnetic gears appealing for wind turbine and offshore drilling applications where a high premium is placed on low maintenance requirements [11, 23]. Interest in low maintenance from these fields stems from the difficulty associated with reaching the operational locations.

It is noted that magnetic gears have shown the potential to be integrated directly into motors to create what is known as a “pseudo-direct drive motor” [4]. This style of motor is able to produce geared rotation in a single device without the use of a gearbox because both motors and magnetic gears operate on principles of rotating magnetic machinery. The input rotational magnetic field from a motor can be easily incorporated into a magnetic gear to drive the magnetic rotors. Combining components greatly simplifies the design required to generate geared rotation and makes the specific torque (torque per unit mass) of magnetic gears comparable to that of a

standard motor with a gearbox. It is noted that temperature becomes an important factor of consideration when implementing magnetic gears in this way because of the heat generated by the motor's stator. Stator windings can typically handle temperatures up to several hundred degrees Fahrenheit depending on the insulation, but the magnetic material used in this thesis begins to experience permanent demagnetization effects above 176°F. Demagnetization of rotor magnets decreases output torque and is not sustainable for long term use.

Specific torque is an important metric for magnetic gears because the cost and design of aerospace projects revolve heavily around the payload of the vehicle [31]. A smaller payload can lead to greater fuel efficiency and design flexibility due to lower lift requirements. Certain magnetic gear designs have shown comparable specific torque to mechanical gears, and this technology has even shown the potential to exceed the specific torques reached by some mechanical gears. Improving the specific torque of magnetic gears is a necessary step towards widespread commercial use.

This thesis is focused on improving the specific torque of magnetic gears with a small axial length and large radius. The rationale behind this geometry is that magnetic gear torque and specific torque scale better with radius than with axial length, for reasons that will be explained later in Subsection 3.2.3.

Modeling improvements are necessary as magnetic gear simulations increase in complexity by adding size and dynamics to the simulations. Magnetic gear research has mostly focused on small and medium sized gears because these are easier to model and prototype. Smaller designs are attractive because a faster design time means that magnetic gear design theories can be tested faster. However, at some point, magnetic gearing theory will become robust enough that the field will turn to

larger magnetic gears. Much of the NASA work cited in this thesis is based around medium sized magnetic gears with an output power of roughly 10 kW, but larger gear models will be necessary to simulate high power applications like wind turbines [26]. Larger magnetic gear simulations require more sophisticated modeling techniques for accurate results because element number increases with model size. More elements will require more computational resources, and depending on available computational resources, these simulations could become impossible to solve.

Another contributor to increased computation time in magnetic gear simulations is the addition of dynamics. Early magnetic gear research focused on torque because for many projects torque requirements are the primary concern, and also torque optimization only requires static simulation. As the field advances, more interest will be given to matters of efficiency as this is a secondary requirement for many projects. To be accurate, most efficiency metrics require the development and implementation of dynamic models capable of quantifying eddy current losses. Dynamic models often take far longer to solve than static models because they require solution at multiple time steps. Reductions in simulation size can have a large impact on the computation time because each time step will have to solve for fewer elements. It is for these reasons that this thesis provides a method to reduce the model size of large magnetic gear models.

### **1.1.2 Principles of Operation**

The operating principle of magnetic gears shares common aspects with mechanical gears with the exception that the forces are applied via magnetic energy as opposed to mechanical contact. Early designs of the magnetic gear were very similar to spur

gears in that there is a singular point of contact between the gears at all times, as shown in Figure 1.2 [1, 30]. As with all gears, the change in rotational speed and

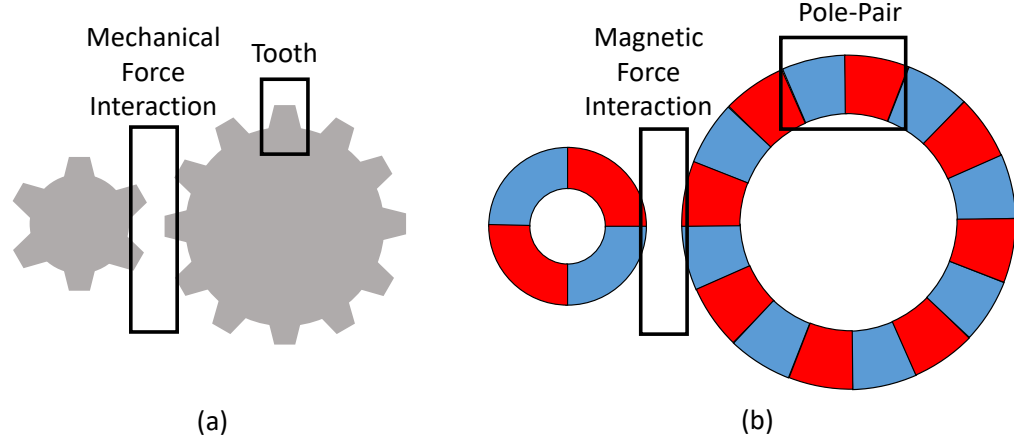


Figure 1.2: (a) Mechanical spur gear with teeth that transfer rotation via mechanical force; (b) magnetic spur gear with pole-pairs that transfer rotation via magnetic force.

torque comes from the differing angular spacing of engagement points between the rotors. For mechanical gears this means the differing angular spacing of gear teeth, and for magnetic gears this means the differing angular spacing of pole-pairs.

The magnetic spur gear is an effective tool for demonstrating the feasibility of magnetic gears, but this design produces very little torque because most of the magnet volume offers no contribution to torque at any given moment. Spur gear torque deficiency gave rise to the coaxial (concentric) magnetic gear (CMG) [22, 3]. The CMG gear design nests the smaller magnet rotor within the larger rotor such that all magnets are contributing to torque at all times. However, without an additional modification, the inner rotor simply spins with the outer rotor, and no gearing is achieved. Rotor nesting requires the addition of a component between the inner and

and outer rotors that modifies the spatial flux harmonics of each rotor. By modifying flux harmonics in the right way, the inner and outer rotors can be made to spin at speeds which reflect the intended gear ratio while remaining magnetically engaged around the entire circumference of the gear.

Harmonic manipulation is achieved by introducing a ring of segmented iron pieces known as a flux modulator. Figure 1.3 shows for a linear example how the high permeability iron pieces of the flux modulator direct flux such that the rotors move at different frequencies while still remaining fully engaged. When comparing (a) and

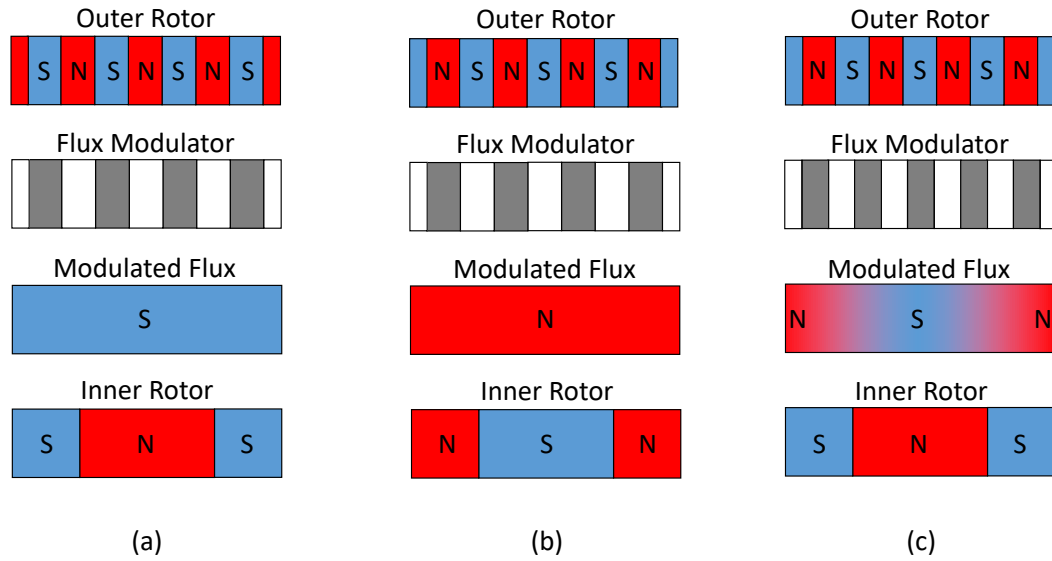


Figure 1.3: A 4 pole-pair outer rotor, 1 pole-pair inner rotor configuration is shown: (a) If the iron pieces are aligned with the south poles then the modulated flux is of south orientation; (b) if the iron pieces are aligned with the north poles then the modulated flux is of north orientation; (c) realistic representation of a flux modulator where the modulated flux is spatially periodic with the frequency of the opposite rotor.

(b) it can be seen that a small movement of the outer rotor can generate an entirely

different modulated field which in turn causes a large movement of the inner rotor. Figure 1.3 (c) shows how iron pieces are spaced in a practical flux modulator to create a spatially variant flux orientation. The configuration shown maintains the principle that small movement of the outer rotor generates large movement of the inner rotor, but allows for magnetic attraction along the entire length of the array. This example can be related to a CMG by imagining that the linear rotors are wrapped into rings (with appropriate length scaling depending on the radius).

The number of pieces used by the flux modulator is determined by the number of pole-pairs on the inner and outer rotors. To properly modulate the magnetic flux harmonics, the number of flux modulator pieces  $Q$  must be defined according to,

$$Q = p_{OR} \pm p_{IR} \quad (1.1)$$

where  $p_{OR}$  is the number of outer rotor or ring rotor pole-pairs and  $p_{IR}$  is the number of inner rotor or sun rotor pole-pairs. If the sum of (1.1) is used, then the input and output rotors spin in opposite directions. If the difference is used, then the input and output rotors spin in the same direction. For most designs, the circumferential length of these flux modulator pieces should be adjusted such that the circumferential fill factor is roughly 50% [10]. Small variations can be made from this number to account for saturation effects and weight considerations.

This style of magnetic gear is very similar in operating principle to a mechanical planetary gear system [17]. Figure 1.4 shows the analogous components. The flux modulator works very similarly to the planet gears in that it provides an intermediate coupling for an inner and outer rotor of different spatial frequencies. “Sun gear”, “planets”, and “ring gear” are terms that are sometimes used to refer to the inner rotor, flux modulator, and outer rotor because of this analogy.



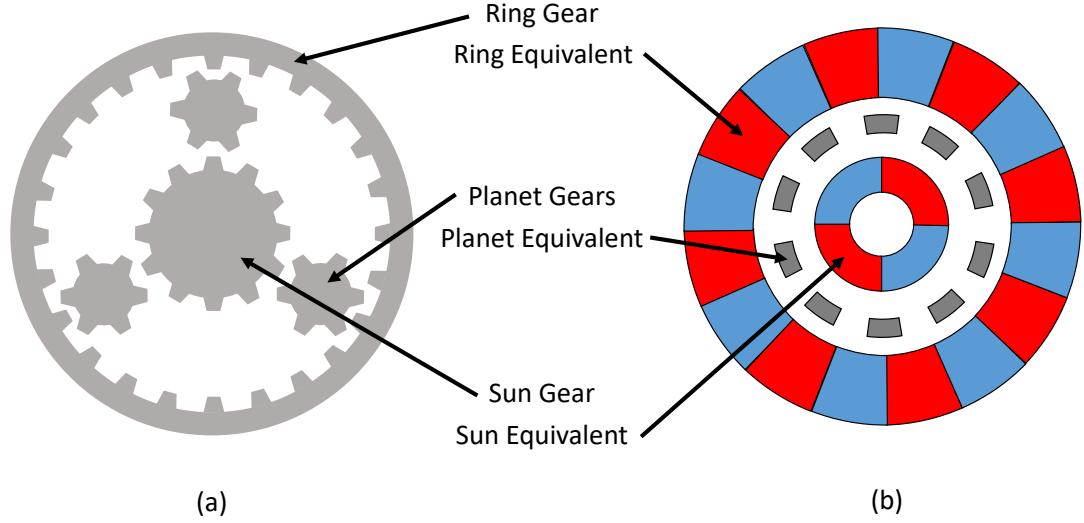


Figure 1.4: (a) Mechanical planetary gear system; (b) equivalent components of a CMG.

All magnetic gear applications discussed in this thesis involve gearing speed down to increase torque. For this reason, the inner rotor will always be taken as the input, leaving the outer rotor and flux modulator as options for the output. The flux modulator can be used as the output rotor because relative motion is the only requirement for proper gear operation. That means that the gear will still operate properly if the outer rotor is fixed and the flux modulator moves relative to the outer rotor. In the case where the flux modulator is fixed and the outer rotor is free to move as the output, the gear ratio is defined as,

$$G_{OR} = \frac{p_{OR}}{p_{IR}}. \quad (1.2)$$

In the case where the outer rotor is fixed and the flux modulator is free to move as the output, the gear ratio is defined as,

$$G_{FM} = \frac{Q}{p_{IR}} = \frac{p_{OR}}{p_{IR}} \pm 1 \quad (1.3)$$

where (1.1) has been used to eliminate  $Q$ . By comparing (1.2) and (1.3) it can be seen that maximum gear ratio is achieved by taking the flux modulator as the output and using a number of flux modulator pieces equal to the sum of inner and outer rotor pole-pairs.

## 1.2 Principles of Static Magnetism

This thesis often deals with concepts that require a firm understanding of static magnetism. The equations in this section will serve as a refresher to some and an introduction to others on the basic magnetic principles that will be used to navigate the field of magnetic gears [5]. These magnetic principles have an analogous relationship with electric circuit theory, so Figure 1.5 has been included to illustrate these similarities. It can be seen that both domains share an effort, flow, and resistive variable: voltage and magnetomotive force, current and magnetic flux, and resistance and reluctance. The interaction of these variables in the electrical domain can be

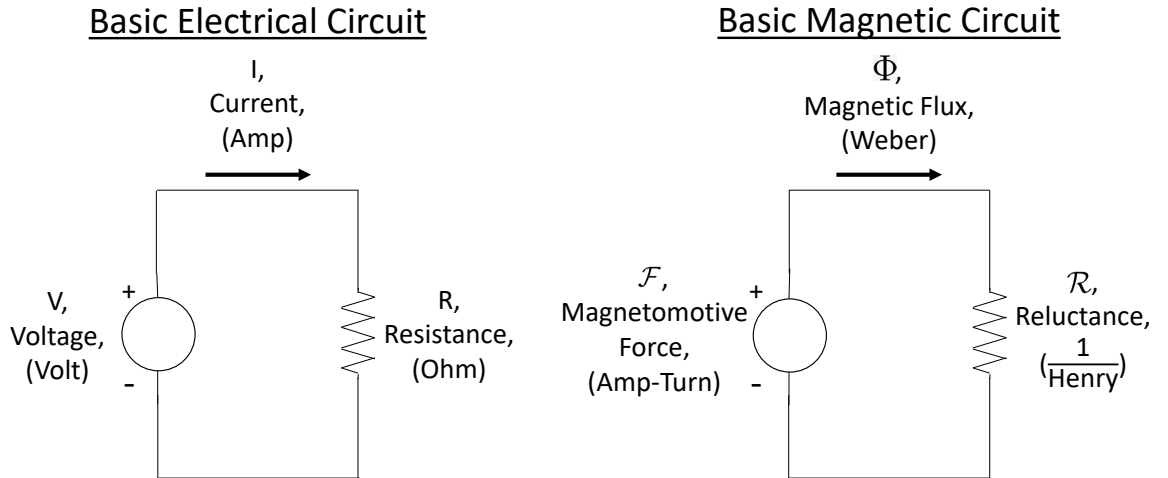


Figure 1.5: Electrical-magnetic circuit analogy.

described by Ohm's Law,

$$V = I * R \quad (1.4)$$

where  $V$  is the voltage,  $I$  is the current, and  $R$  is the resistance. An equivalent equation exists for the magnetic domain and is known as Hopkinson's Law,

$$\mathcal{F} = \Phi * \mathcal{R} \quad (1.5)$$

where  $\mathcal{F}$  is the magnetomotive force,  $\Phi$  is the magnetic flux, and  $\mathcal{R}$  is the reluctance.

The most important terms used in the field of magnetic gearing include: magnetic field, magnetic flux density, and permeability. Magnetic field is related to magnetomotive force through (1.6),

$$\mathcal{F} = \oint \vec{H} \cdot d\vec{l} \quad (1.6)$$

where  $\vec{H}$  is the magnetic field, and  $d\vec{l}$  is an infinitesimal length of a contour. This means that the magnetic field can be thought of as a distribution of many magnetomotive forces throughout a 2D or 3D space. Magnetic flux density is related to magnetic flux through,

$$\Phi = \oiint \vec{B} \cdot d\vec{A} \quad (1.7)$$

where  $\vec{B}$  is the magnetic flux density and  $d\vec{A}$  is the infinitesimal area of a surface. This means that magnetic flux density can be thought of as a distribution of magnetic flux concentration throughout a 2D or 3D space. Finally, magnetic permeability is related to reluctance through,

$$\mathcal{R} = \frac{l}{\mu * A} \quad (1.8)$$

where  $l$  is the length of the magnetic path,  $\mu$  is the magnetic permeability of the material, and  $A$  is the cross-sectional area of the magnetic path. This means that permeability can be thought of as a metric for material reluctance in 2D or 3D space.

These three variables have a relationship to each other that is analogous to (1.5). This relationship is described by,

$$\vec{B} = \mu \vec{H}. \quad (1.9)$$

$\vec{H}$  is the effort variable,  $\vec{B}$  is the flow variable, and  $\mu$  is the resistive variable. In simple terms, (1.9) is a modified version of (1.5) that is used to describe magnetic behavior using vector fields in multi-dimensional space.

The final consideration of this section is how this magnetic behavior generates torque within the magnetic gear. As discussed earlier, magnetic flux density is the resultant flow based on various potential and resistive elements in a magnetic gear. This is an important conceptual point that the  $\vec{B}$  field, not the  $\vec{H}$  field, is the physical manifestation of magnetic behavior that can be observed in the real world. Magnetic flux density is related to torque through equations provided in the COMSOL documentation [8]. First magnetic flux density is converted into shear stress using the Maxwell stress tensor in the absence of an electric field,

$$\hat{n}\tau = \frac{1}{\mu}(\hat{n} \cdot \vec{B})\vec{B}^T - \frac{1}{2\mu}(\vec{B} \cdot \vec{B})\hat{n} \quad (1.10)$$

where  $\hat{n}$  is the unit vector that is normal to and outward from the component surface, and  $\tau$  is the shear stress. Torque is then calculated from shear stress according to

$$\vec{T} = \int_{\partial S} (\vec{r} - \vec{r}_0) \times (\hat{n}\tau) dS \quad (1.11)$$

where  $\vec{T}$  is the input/output torque,  $\vec{r}_0$  is the origin,  $dS$  is an infinitesimal area on the surface of the component, and  $\vec{r}$  is the length vector from  $\vec{r}_0$  to  $dS$ . The torque vector is then converted to the relevant scalar component with,

$$T_{ax} = \frac{\vec{r}_{ax}}{|\vec{r}_{ax}|} \cdot \vec{T} \quad (1.12)$$

where  $T_{ax}$  is torque around the central axis of the gear and  $r_{ax}^{\rightarrow}$  is the direction vector for the central axis.  $T_{ax}$  may be referred to as  $T$  throughout this thesis because torque around the central gear axis is the only relevant torque. This torque is calculated for both the output and input components and the ratio of these torques is expected to match the gear ratio.

### 1.3 Halbach Arrays

A Halbach array is an arrangement of permanent magnets with specific magnetization vectors that concentrate flux density towards one side of the array. The result is both an increase in magnitude of the flux density waveform on that side of the array, and also a waveform that is closer to sinusoidal. These improvements are of particular interest to the field of magnetic gearing because the permanent magnet rotors must project large, sinusoidal flux density waveforms towards the flux modulator to generate maximum torque.

#### 1.3.1 Linear Array

The first mention of a Halbach structure was in 1973 by Mallinson who was interested in the concept for the improvement of tape recording performance [21]. Mallinson presented the idea of a linear magnet structure in which the magnetization vector was a rotating function of the linear position. It was found that for an ideal case, flux could be nearly completely eliminated from one side of the array while being increased on the other side of the array. This concept has limitations however, as it is currently not practical to create permanent magnets with gradient magnetization vectors. The solution is to use discrete magnets that approximate the magnetization

vector gradient. The magnetization vector of these magnets is determined by,

$$\phi_{HB} = \frac{360 * n}{n_{PP}} \quad (1.13)$$

where  $\phi_{HB}$  is the magnetization angle of a magnet in the Halbach array,  $n$  is an integer number indicating the sequential position of a magnet in the Halbach array, and  $n_{PP}$  is the number of magnets per pole-pair. Note that the initial value of  $n$  can be tailored to suit the circumstance. (1.13) is depicted in Figure 1.6. The red lines in the image show the path of flux as it exits the array into free space. Note that the array structure can be repeated to create an array of many pole-pairs.

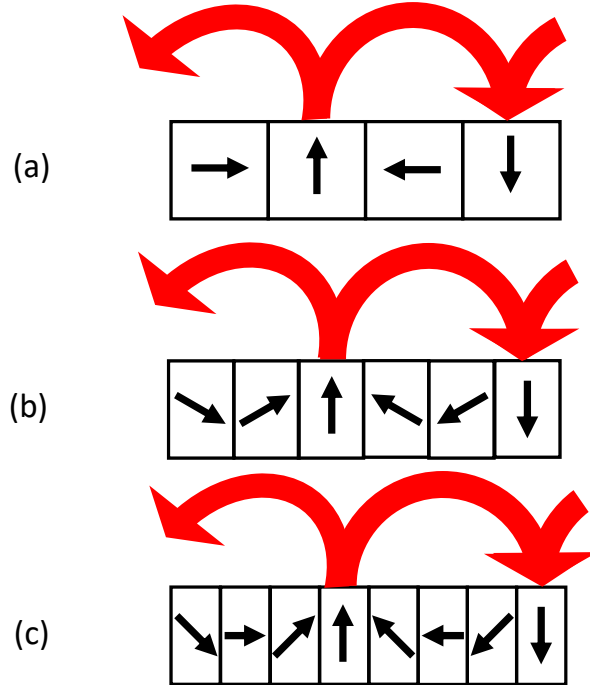


Figure 1.6: (a) Halbach array with four magnets per pole-pair offset at 90° angles; (b) Halbach array with six magnets per pole-pair offset at 60° angles; (c) Halbach array with eight magnets per pole-pair offset at 45° angles.

### 1.3.2 Halbach Cylinder

It wasn't until Halbach in 1980 that a depiction of a Halbach cylinder was presented in the literature for the purpose of focusing particle accelerator beams [18]. A Halbach cylinder is effectively a linear Halbach array that has been wrapped into a circular shape. Figure 1.7 shows the magnetization vectors of a Halbach cylinder with four pole-pairs and four magnets per pole-pair. Again, the red lines show the flux path through free space.

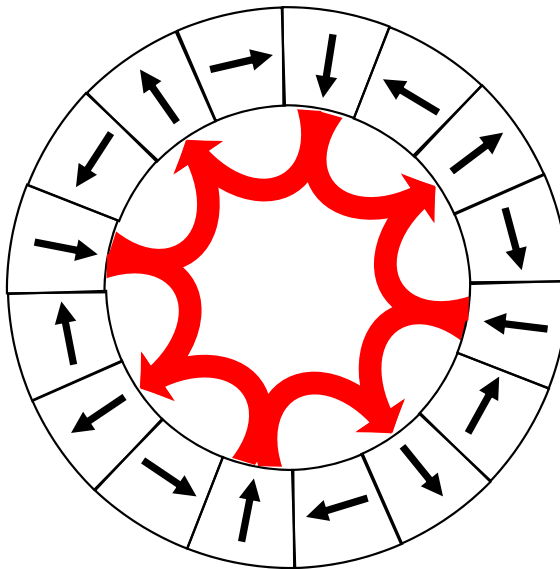


Figure 1.7: A Halbach cylinder with four pole-pairs and four magnets per pole-pair.

Halbach cylinders have been shown to provide significant improvement to magnitude of the flux density waveform on the inner portion of the cylinder. The mechanism for this improvement is that one side of the cylinder has north and south poles that are relatively close to each other while the other side has north and south poles that

are relatively far apart. The discrepancy in distance means that flux density waveform will have a small magnitude on the side of the magnet with close north and south poles because flux has very near options for returning to the magnets. On the other hand, the flux density waveform on the side with distant north and south poles will be large in magnitude because flux has no near options for returning the magnets, and thus will penetrate deep into the air while searching for a return path. Note that the magnet arrangement shown in Figure 1.7 can be reversed to increase flux density on the outer portion of the cylinder. The inner rotor is reversed in such fashion to concentrate flux outwards.

## 1.4 End Effects

Improvements to magnetic gear torque and computation time of magnetic gear simulations shown in this thesis derive from the inclusion of end-effect considerations when tackling design and modeling problems. For this reason, it is necessary to discuss the nature of magnetic gear end-effects and their contribution to performance and computational inefficiency. End-effects are reductions in magnetic flux density that result from flux density loss to an axial air domain. Description of end-effect behavior in this section will be based on the findings of Gerber and Wang [16].

End-effect losses reduce torque because flux density lost to the air domain either cannot contribute to torque, or contributes less to torque than flux density in an ideal case. In an ideal case, magnetic flux would only be free to travel in the radial and tangential directions as this would not allow for flux to travel over the axial ends of the gear. Unfortunately, flux only behaves this way in 2D models which is why 3D models with axial air domains must be constructed to observe these end-effects via



simulation. Figure 1.8 illustrates two methods by which flux density is lost to the axial air domain. This figure will be used in the following subsections to expound upon the nature of these end-effects.

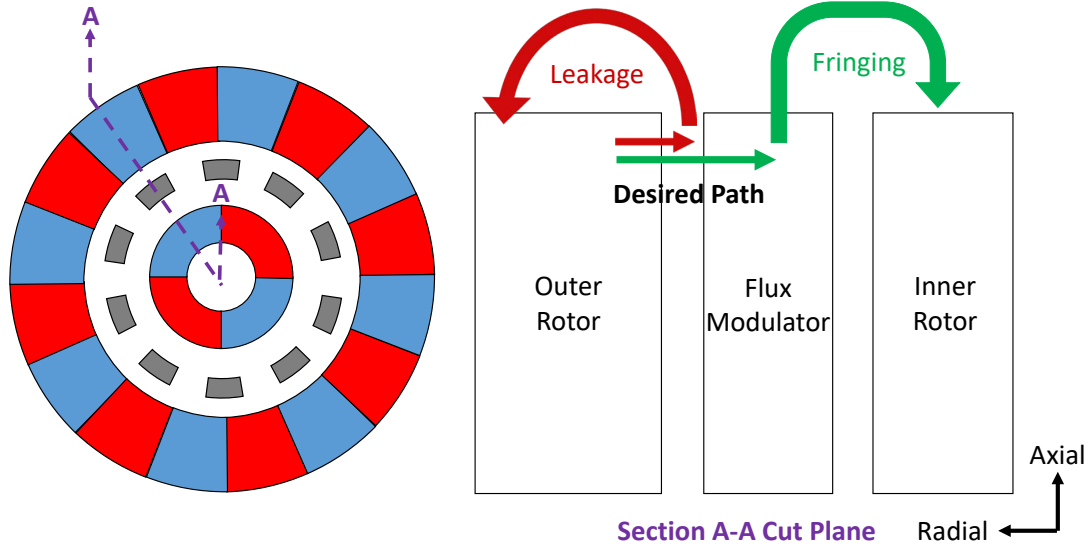


Figure 1.8: A cross-section of a magnetic gear which shows the flux paths for both leaking and fringing which cause decreased flux density at the rotors and flux modulator. Only flux from the outer rotor is shown, but equivalent paths exist for the inner rotor.

### 1.4.1 Leakage

All magnets in a magnetic gear exhibit an inefficiency known as leakage. This is when flux that should be contributing to torque, instead leaks to the back end of its source magnet. Figure 1.8 shows this path in red. It is noted that flux density lost to this end effect contributes nothing to output torque because it does not couple in the flux modulator.

### 1.4.2 Fringing

Even some of the flux that makes it to the flux modulator and contributes to torque can display an inefficiency known as fringing. Fringing is when flux couples with both the flux modulator and the axial air domain which reduces magnetic flux density in the flux modulator. This reduces magnetic flux density because the increased distance traveled through the axial air domain increases reluctance of the circuit. The increase of distance traveled through the axial air domain is known as bulging because the flux lines take the path of a semicircle to couple with the opposite rotor as shown in Figure 1.8 which creates the appearance of a bulge.

### 1.4.3 Escaping

Certain sections of a magnetic gear where inner rotor and outer rotor magnets of the same pole orientation align radially exhibit a behavior known as escaping. This scenario is shown in Figure 1.8 where two south poles have aligned radially. Alignment of magnets with the same pole orientation causes additional flux to escape to the axial domain because of the repulsive forces. Escaping is classified as an extreme version of leakage where repulsive forces direct additional flux back to its source magnet through the axial air domain. It has been proven that this sort of end-effect can have a significant effect on end-effect torque reduction. Escaping has been quantified by breaking up a magnetic gear model into two sections, one where only magnets of the same orientation are aligned radially and one where only magnets of opposite orientation are aligned radially [16]. The study found that the repulsive section showed a 19.2% decrease in torque when considering end-effects, and that

the attractive section showed only a 6.3% decrease in torque when considering end-effects. This shows that escaping can be a significant contributor to torque loss due to end-effects.

## **1.5 Objectives**

### **1.5.1 Reduce Computation Time**

The first goal of this thesis is to reduce the size and computation time of magnetic gear simulations. These improvements are made possible by accounting for axial variation of flux density caused by the prevalence of end-effects. By accounting for these end-effects, the central portion of a 3D magnetic gear model can effectively be removed and replaced by 2D simulation. The torque contributions of a shortened 3D model and supplementary 2D model are then combined to generate a comprehensive estimate of torque for the given magnetic gear design. Another objective related to this goal is to determine the relevant magnetic gear design variables that contribute to the significance of end-effects for a certain gear design. Design variables will be used to make recommendations for appropriate length reduction of the 3D model such that accurate results can be obtained while still making significant reductions to computation time.

### **1.5.2 Increase Specific Torque**

The second goal of this thesis is to increase the specific torque performance of magnetic gears. Specific torque improvement is made possible by working to minimize the drop off in magnetic flux density near the axial ends of the magnetic gear that results from end-effects. This drop off can be minimized by utilizing magnets on the axial ends of the gear that have a non-zero axial component within their magnetization

vector. In other words, they discourage magnetic flux density from leaking over the end of the magnetic gear by directing flux towards the axial center of the gear. Another objective related to this goal is to determine optimal geometric and magnetic design variables for axially oriented magnets such that they maximize specific torque. These design variables will be used to inform axial magnet additions to other magnetic gear designs.

## **1.6 Thesis Organization**

This thesis presents methods for both decreasing the computation time of magnetic gear COMSOL simulations and increasing the specific torque of CMGs by accounting for end-effects. Chapter 2 provides an overview of the COMSOL modeling process and explains modeling features that are used for all simulations in this thesis. Chapter 3 applies the reduced length modeling process and explores trends that are useful for implementing this style of modeling. Chapter 4 retrofits CMGs with cladding magnets to improve specific torque and lays out theory for the retrofitting of generic CMGs with cladding magnets. Chapter 5 summarizes the findings of this thesis and provides direction for future research.

## Chapter 2: COMSOL Model Summary

This chapter includes:

- An explanation of the COMSOL FEM solution process
- Physical and geometric features of the COMSOL models that reduce computation time and increase solution accuracy
- An overview of mesh characteristics used by models in this thesis
- The verification and validation methods that build confidence in the modeling results of this thesis

### 2.1 COMSOL FEM Theory

This section serves as an explanation of the COMSOL FEM process and the equations solved during the FEM process. The explanation provided is not a step-by-step guide to COMSOL FEM solution, but rather a brief overview of the concepts involved. It is necessary to begin by defining the solution goal of the simulation. For all simulations carried out in this thesis, the goal is to determine the  $\vec{B}$  field such that torque can be calculated.

The rotating magnetic machinery COMSOL module used for all simulations in this thesis does not actually solve for the  $\vec{B}$  field directly. Instead, it solves for the

magnetic vector potential as shown by Wimmer et al. [28]. The derivation for the magnetic vector potential equation begins with two of Maxwell's equations,

$$0 = \vec{\nabla} \cdot \vec{B} \quad (2.1)$$

where  $\vec{B}$  is the magnetic flux density vector and,

$$\vec{\nabla} \times \vec{H} = \vec{J} + \frac{\partial \vec{D}}{\partial t} \quad (2.2)$$

where  $\vec{H}$  is the magnetic field intensity,  $\vec{J}$  is the current density, and  $\vec{D}$  is the electric displacement. Models in this thesis are static and contain no electric sources so  $\vec{J}$  and  $\vec{D}$  are 0. The magnetic vector potential is introduced through,

$$\vec{B} = \vec{\nabla} \times \vec{A} \quad (2.3)$$

where  $\vec{A}$  is the magnetic vector potential. Eq (2.3) satisfies the condition of (2.1) according to vector calculus theory. This is also how the final magnetic vector potential solution is related back to the  $\vec{B}$  field. The material relation,

$$\vec{B} = \mu(\vec{H} + \vec{M}) \quad (2.4)$$

where  $\mu$  is the material permeability and  $\vec{M}$  is the magnetization, is introduced to eventually be plugged into (2.2). Magnetization is simply another way of express remanence as it relates to remanent flux density through,

$$\vec{M} = \frac{1}{\mu_{mag}} * \vec{B}_r \quad (2.5)$$

where  $\vec{B}_r$  is the remanent flux density and  $\mu_{mag}$  is the permeability of the permanent magnet material. Plugging (2.5) and (2.3) into (2.4), which is then plugged into (2.2) gives,

$$\vec{\nabla} \times \left( \frac{1}{\mu} \vec{\nabla} \times \vec{A} \right) = \vec{\nabla} \times \frac{1}{\mu_{mag}} * \vec{B}_r. \quad (2.6)$$

Eq (2.6) is what COMSOL satisfies to determine the magnetic vector potential.

COMSOL documentation outlines the process for solution of (2.6) [20]. The first step is to divide the geometric domain of the simulation into discrete elements. Next, a shape function must be chosen to describe solution behavior over the element. Choosing a higher order shape function increases degrees of freedom for the model, but lower order functions compromise solution accuracy. A quadratic tetrahedral element has 7x the degrees of freedom of a linear tetrahedral element [7]. All 3D models in this thesis utilize linear tetrahedral elements because limited computational resources do not allow for the use of quadratic tetrahedral elements while still accurately representing the geometry of the magnetic gear. All 2D models in this thesis utilize quadratic triangular elements.

Eq (2.6) must be written in its weak form and discretized over each element to generate a local matrix. The final step before solution is to assemble these local matrices into a global matrix. The default stationary solver employed by COMSOL to solve global matrices operates on principles of the damped Newton method. In other words, a damped instantaneous rate of change for the solution variable is used to better approximate future solution guesses.

## **2.2 Physical/Geometric Features**

There are important components of COMSOL models presented in this thesis that fall outside the realm of the FEM solution process and the mesh characteristics. In this section, these physical and geometry related features will be discussed to highlight some of the modeling attributes that are specific to the modeling of magnetostatic systems and even more specific to the modeling of magnetic gears.

### 2.2.1 Symmetry

One essential feature of well-posed magnetic gear models is the exploitation of symmetry. The computational resources required to run these models with proper mesh refinement can be quite high, so it is necessary to reduce model size by accounting for any possible symmetry that may exist. Given the nonlinear scaling of computation time with respect to model size, even reducing the model size by half can cause a much greater reduction in computation time.

Symmetry about the central xy-plane is one such symmetry that is utilized in every model presented in this thesis. The exact location of this plane is shown in Figure 2.1. The symmetry allows for only one axial half of the magnetic gear to be modeled by implementing a boundary condition along the plane of symmetry. The COMSOL models in this thesis use a magnetic insulation boundary condition along this plane which acts according to,

$$\hat{n} \cdot \vec{B} = 0 \tag{2.7}$$

where  $\hat{n}$  is the normal vector (unit vector in the z-direction for this case). This boundary condition assigns the magnetic flux density in the z-direction to be zero which must be true at this plane if the gear is completely symmetrical about the plane in question.



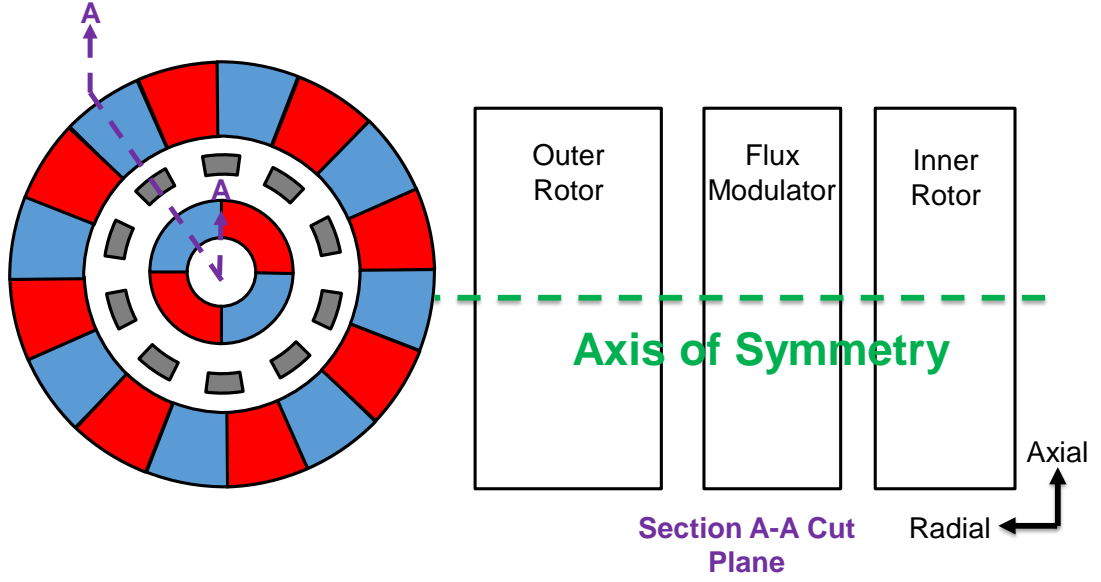


Figure 2.1: Central x-y plane of symmetry shown on a radial cut plane.

The other symmetry, that is only used for the outer radius and pole-pair scaling factor trials of Subsections 3.2.3 and 3.2.4 respectively, is a periodic symmetry with respect to angular position. In other words, the full magnetic gear can be represented by repeated sectors. This means that only one sector needs to be modeled with periodic boundary conditions to fully represent the gear. Angular symmetry was used for the radial scaling trials because some of these models were very large and difficult to solve with available computational resources. An example of such a periodic symmetry is shown in Figure 2.2. The axis of symmetry shown divides the gear into two, equal, repeated periods. The pole-pairs of models that use this symmetry have been subtly adjusted to even numbers so that this symmetry can be applied.

A continuous boundary condition is used to model the periodicity [8]. The boundary condition requires the definition of a source and destination boundary and behaves

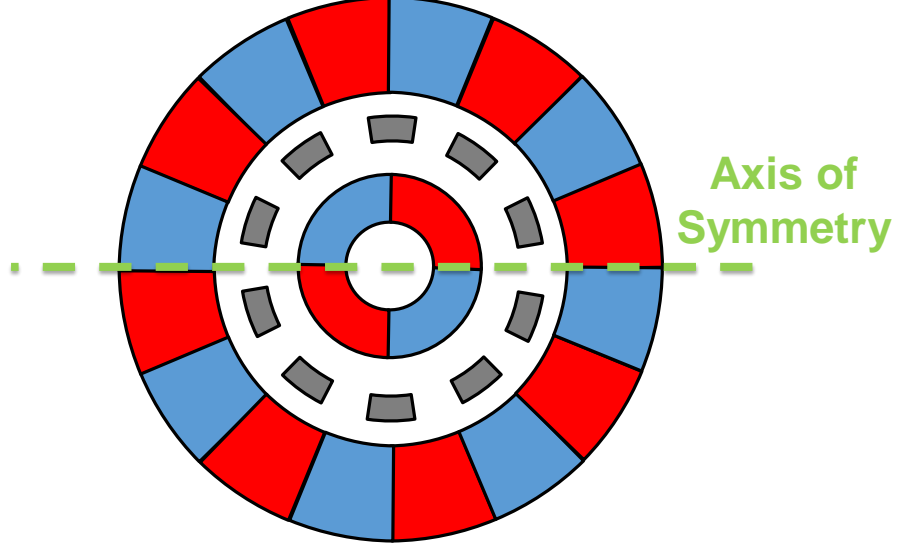


Figure 2.2: An axis of symmetry for a magnetic gear with angular periodicity.

according to,

$$\vec{A}_{src} = \vec{A}_{dst} \quad (2.8)$$

and,

$$V_{m,src} = V_{m,dst} \quad (2.9)$$

where  $\vec{A}_{src}$  is the magnetic vector potential at the source boundary,  $\vec{A}_{dst}$  is the magnetic vector potential at the destination boundary,  $V_{m,src}$  is the magnetic scalar potential at the source boundary, and  $V_{m,dst}$  is the magnetic scalar potential at the destination boundary. The magnetic vector potential directly relates to the  $\vec{B}$  field as seen in (2.3). The magnetic scalar potential directly relates to the  $\vec{H}$  field by,

$$\vec{H} = -\nabla V_m. \quad (2.10)$$

This means that for the magnetic vector potential and magnetic scalar potential to be equal at both the source and destination, the  $\vec{H}$  and  $\vec{B}$  fields must be equal.

The equality of fields along the source and destination is what defines continuity. Figure 2.3 shows the boundary orientation for the periodic boundary condition with the source boundary on the left and the destination boundary on the right. These boundary orientations define in what directions the continuity condition is applied.

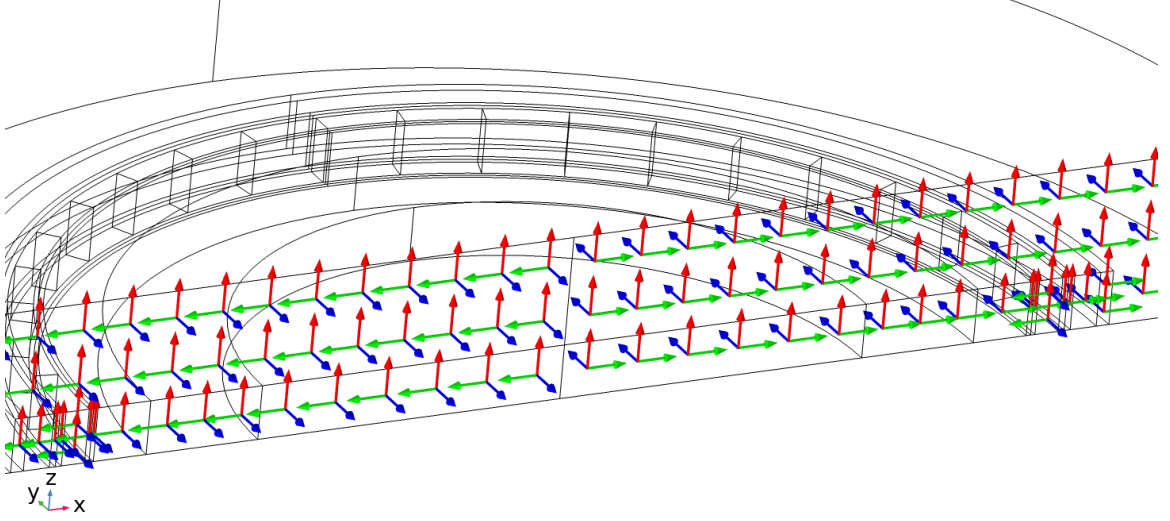


Figure 2.3: Boundary orientation for the source boundary on the left and the destination boundary on the right.

### 2.2.2 Axial Air Domain

A feature of the 3D COMSOL models is the ability to include an axial air domain. An air domain is necessary to account for the end-effects that reduce torque in all magnetic gears. A study was performed on the sensitivity of torque results to the length of the axial air domain, defined as the distance from the axial end of the magnetic gear to the end of the air domain. The results of this study are shown in Figure 2.4. The “PT-1 Variant” is a reduced length version of NASA PT-1 magnetic

gear that is 0.59" (15.0 mm) in axial length. The results of this study should still be applicable to all PT-1 variations because the shortened length makes the torque results of this model more sensitive to end-effects.

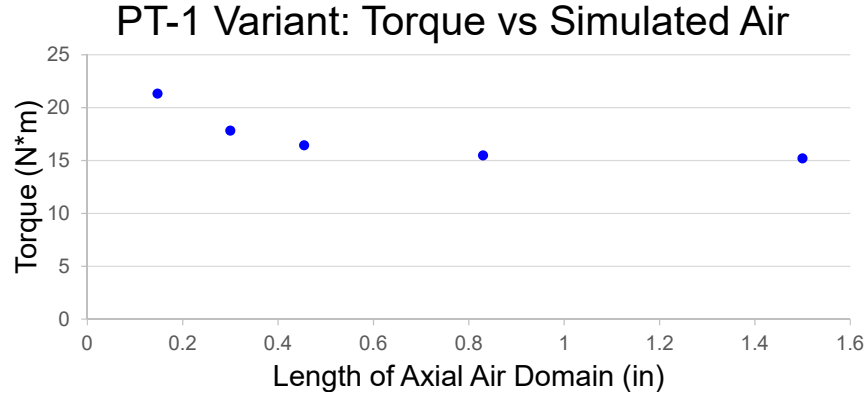


Figure 2.4: Convergence study on the necessary length of the axial air domain for accurate modeling of end-effects. The maximum length is 1.5" (38.1 mm).

Figure 2.4 shows that the torque begins relatively large when the simulated air is short. This is because when there is insufficient air domain length, flux that would have leaked or fringed is instead encouraged to couple through the flux modulator and contribute to torque. As the length of the air domain becomes large, a sufficient amount of air is eventually available to capture much of the leaking and fringing, so the torque results level out. Between an air domain length of 0.83" (21.1 mm) and 1.5" (38.1 mm), the torque only decreases by 0.288 N\*m. Based on this result, all air domain lengths in this thesis fall between 1.0" (25.4 mm) and 1.5" (38.1 mm). Torque results were not as sensitive to variation of the radial air domain because the

use of Halbach arrays limits the magnetic activity outside the radial bounds of the gear.

### 2.2.3 Magnetic Considerations

An important feature utilized by the magnetic gear models is the nonlinear B-H curve that defines magnetic behavior of the flux modulator material. The material used for the flux modulator for all models presented in this thesis is 0.01" (0.254 mm) laminations of HF-10 electrical steel, a non-oriented steel with a C5 coating [2]. The C5 coating is an electrical insulator included for the purpose of reducing eddy current losses. The B-H curve for this material can be seen in Figure 2.5.

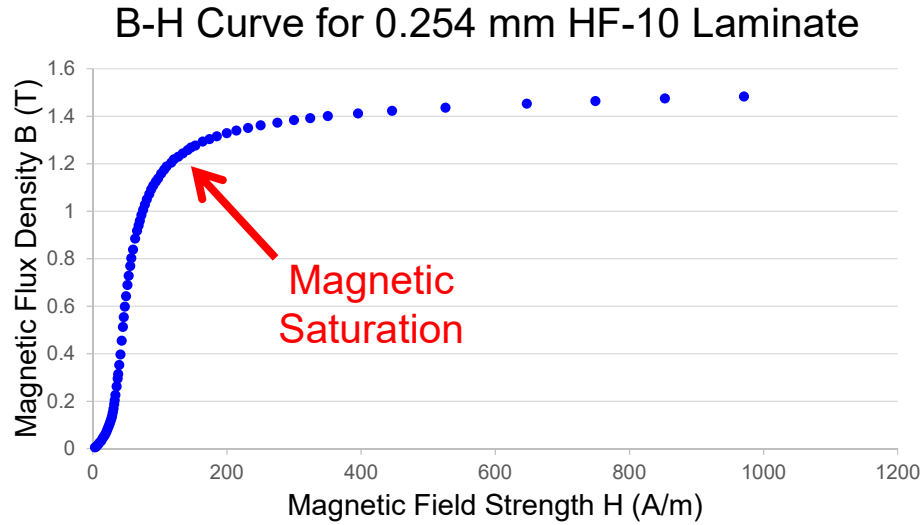


Figure 2.5: Nonlinear B-H curve for 0.01" (0.254 mm) HF-10 electrical steel laminate. The red arrow indicates around where magnetic saturation begins to occur.

It is necessary to use a nonlinear B-H curve for accurate magnetic gear modeling because of magnetic saturation. Magnetic saturation is the point of increasing magnetic field strength at which equivalent increases in field strength give significantly less magnetic flux density in return. The diminishing return of flux density can also be conceptualized as a decrease in permeability with increasing magnetic field strength. A linear material model cannot account for saturation because it assumes the B-H “curve” has a constant slope. This assumption can cause large overestimations of magnetic flux density depending on whether or not the flux modulator is operating near saturation.

The final feature of this section will be the magnet material used. All models presented in this thesis use the N52 neodymium magnet material. N52 has a remanent (residual) magnetic flux density of 1.465 T and a relative permeability of 1.05. This magnet material was chosen for use in these models because of its high remanent flux density.

## **2.3 Mesh Summary**

The following section will serve as an overview of the general meshing practices employed to all models in this thesis. This summary will focus mainly on 3D model meshing because there has always been sufficient computational resources available to use high mesh refinement for the 2D models. A standard 2D mesh refinement is shown in Figure Fig: 2D Mesh Quality. All 3D meshing is done using various refinement of tetrahedral elements to create unstructured meshes. Model size, and by relation element number, could vary quite a bit depending on the design variable being swept. This variance means that smaller models could have as few as 700,000 elements

whereas large models could have up to 2,000,000 elements. The elements numbers mentioned correspond to 3,500,000 degrees of freedom for the smallest models and 10,000,000 degrees of freedom for the largest models.

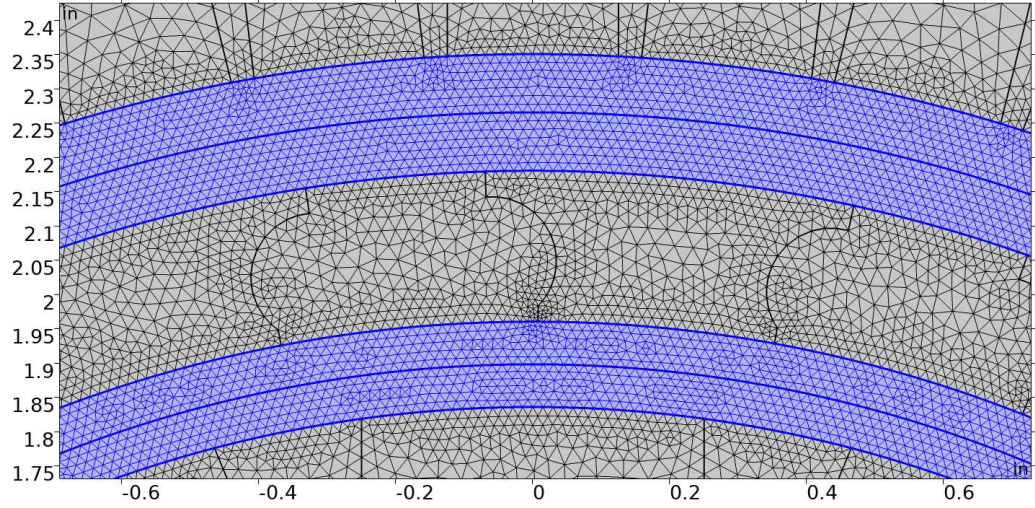


Figure 2.6: Standard mesh refinement for a 2D magnetic gear model. The air gap is highlighted in blue.

It has been found to be most productive to focus these elements primarily around the air gaps and flux modulator. This is because the area around the flux modulator shows the most nonlinearity due to the sharp permeability spikes from the modulator material. Figures 2.7 and 2.8 show the results of a convergence study that was conducted on a NASA PT-1 variation to quantify convergence of the air gap mesh resolution. Figure 2.7 shows convergence of output torque and Figure 2.8 shows convergence of gear ratio error as compared to the theoretical value of 4.25. The rule of thumb used for models in this thesis based on the convergence results is that there

should be a minimum of 1 element along the air gap thickness per 0.03" (0.76 mm) of air gap thickness.

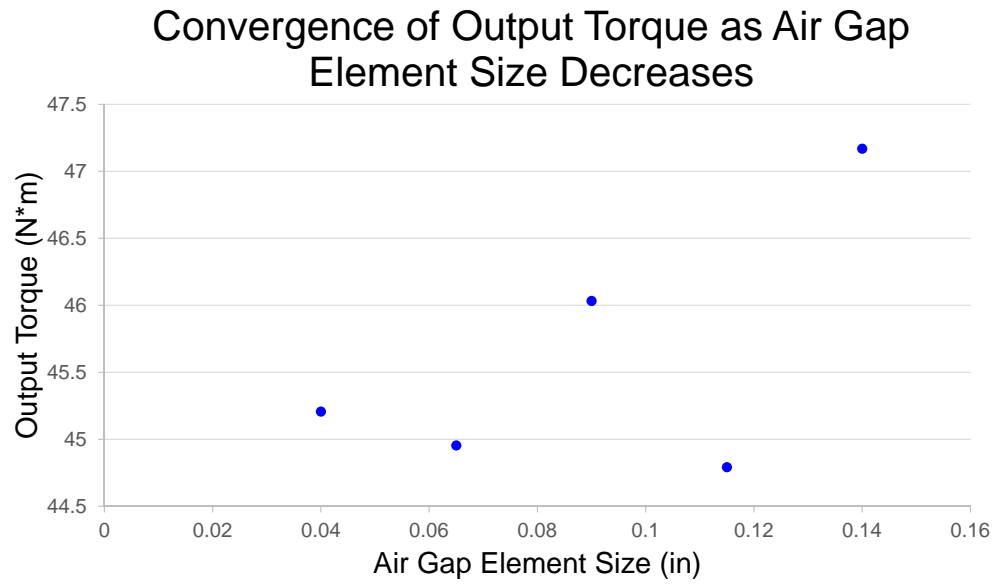


Figure 2.7: Convergence of output torque as mesh resolution of the air gaps becomes finer.



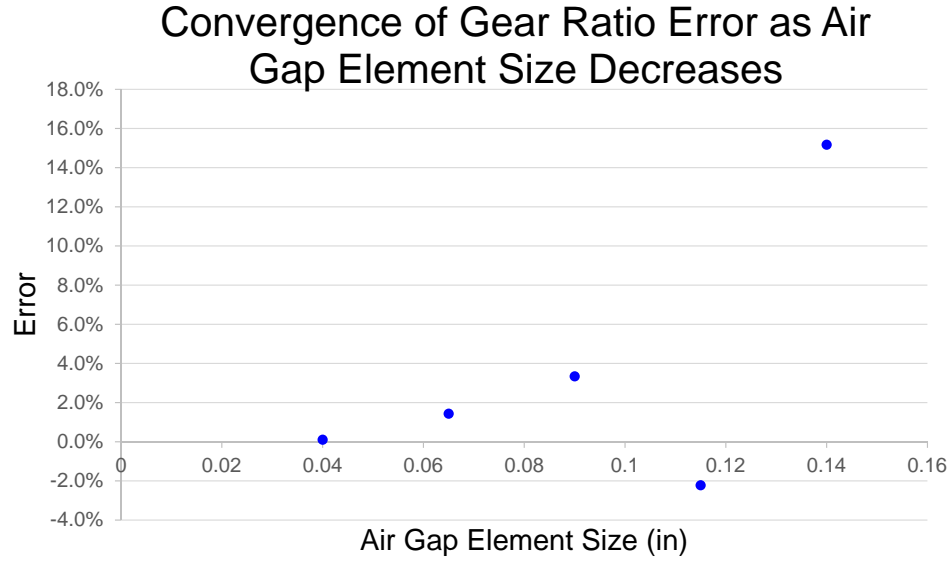


Figure 2.8: Convergence of the simulated gear ratio as compared to the theoretical gear ratio when air gap element size is decreased. The theoretical gear ratio is 4.25.

Figure 2.9 shows how a typical model begins with a fine mesh around the air gaps and then fills in gradually rougher mesh further from the air gaps. The axial air domain and radial air domains require little refinement because the flux density in these regions is relatively small compared to the flux modulator region, so they contribute less to torque. Also, these large regions of high permeability mean that there are no sharp changes in flux density that would be poorly estimated by a rough mesh.

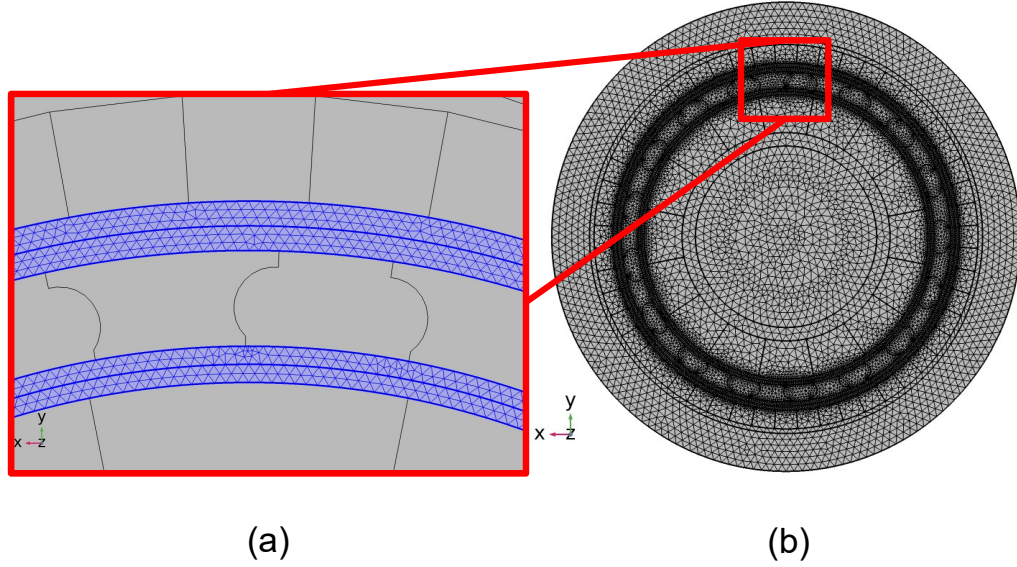


Figure 2.9: (a) Mesh close-up showing stage 1 of the meshing process that defines the air gaps; (b) full mesh that has been filled in by stage 2.

One last mesh consideration is the use of the copy mesh feature when using the periodic boundary condition. As previously mentioned, the periodic boundary condition in COMSOL applies a continuity requirement to a source and destination face. For the continuity requirement to work properly, nodes on the source and destination face must be in the exact same relative location such that flux density and field strength can be directly applied at the destination face.

## 2.4 Modeling Verification and Validation

Three main methods have been used to build confidence in the modeling results presented in this thesis. The first two methods verify that the model functions in alignment with conceptual understanding of magnetic gearing behavior. The final

method validates that the procedures used in this thesis to model magnetic gears produce results that are representative of real-world magnetic gears.

### 2.4.1 Gear Ratio Check

The first method is to compare the gear ratio of the model to the theoretical gear ratio. Gear ratio is one of the few performance characteristics that can be calculated very accurately with a simple theoretical equation. The theoretical gear ratio from (1.3) can be very quickly compared to the model's gear ratio which is calculated from,

$$G = \frac{T_{out}}{T_{in}} \quad (2.11)$$

where  $T_{out}$  is the output torque and  $T_{in}$  is the input torque. A correct gear ratio does not guarantee that the model is behaving properly; however, this serves as a quick check to verify that the magnetic elements are interacting in correct proportion.

### 2.4.2 Pseudo 2D Model

The second method is a process for 3D model verification which compares the 2D modeling results of a gear to a pseudo 2D model. The pseudo 2D model is a 3D model that has no axial air domain. Figure 2.10 shows a generic pseudo 2D model. Without an axial air domain, flux has no ability to travel in the z-direction due to no model variation of any kind in the z-direction. This means that all differences in results between the 2D model and pseudo 2D model can be attributed to the meshing quality. 2D models can utilize fine meshes and high order mesh elements, so there is a high level of confidence in the results of these models. If the pseudo 2D model can accurately reproduce the results of the 2D model, then it is assumed that the meshing quality of the 3D model is sufficient.

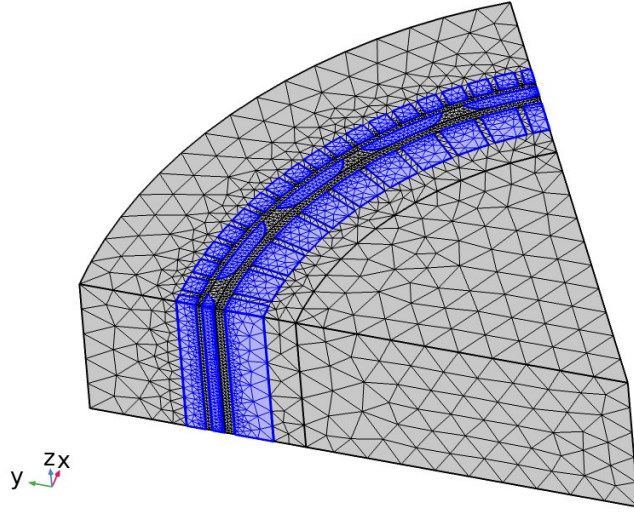


Figure 2.10: Generic pseudo 2D model with no axial air domain. The magnetically active components are highlighted in blue.

The pseudo 2D method has been used to verify many models, but a specific example is when it was used to verify the 3D mesh of the NASA PT-4. The torque results for each model type are given in Table 2.1. The first promising feature of these results is that the gear ratios for all models are near the theoretical gear ratio of 12.2. The gear ratio of the 3D model has a percent error of 0.246% with respect to the theoretical gear ratio which indicates that the magnetic flux densities are interacting in appropriate proportion. Another promising indicator is that the percent error between output torque of the 2D and pseudo 2D models is only 0.670%. This means that the 3D mesh is accurately representing a mesh of much higher resolution.

Table 2.1: Torque results for PT-4 model variations.

Model	Input Torque (N*m)	Output Torque (N*m)	Gear Ratio
3D	20.1	246	12.2
2D	25.7	315	12.2
Pseudo 2D	25.6	313	12.2

### 2.4.3 Experimental Validation

The final method of verification is the comparison of torque results between COMSOL models created using the techniques explained in this section to experimental magnetic gear prototypes. Table 2.2 shows the torque output of all the 3D COMSOL models made for NASA PTs and how closely they match the respective experimental results [26, 25, 27]. It builds confidence in the methods used for COMSOL modeling and meshing that for both PT-1 and PT-3, the percent error between simulation and experimental torque is only  $\sim 2\%$ .

Table 2.2: Current COMSOL and experimental torque results for all NASA PTs.

Model	COMSOL Torque (N*m)	Experiemental Torque (N*m)	Percent Error
PT-1	33.3	34.0	2.06%
PT-2	N/A	128	N/A
PT-3	113	115	1.74%
PT-4	246	N/A	N/A
PT-5	27.9	N/A	N/A

## Chapter 3: Reduced Length Modeling of Magnetic Gears

This chapter includes:

- An explanation of the reduced length modeling method
- The individual relationship between several design variables and end-effect factor
- Time savings and torque error when applying the reduced length modeling method to two PT-1 based designs
- Recommendations for how to generally apply the reduced length modeling method

### 3.1 Reduced Length Modeling Theory

This section looks to apply the electric machines concept of reduced length modeling to magnetic gears for the purpose of reducing simulation size and computation time. This concept was originally developed for motor applications and works by combining torque results from a reduced length 3D simulation and a supplemental 2D simulation [13]. The reduced length 3D model is used to estimate the torque produced by the portion of the gear that is subject to end-effects. The 2D model is

used to estimate the torque produced by the axially central portion of the gear that is not subject to end-effects. These portions of the gear are illustrated in Figure 3.1.

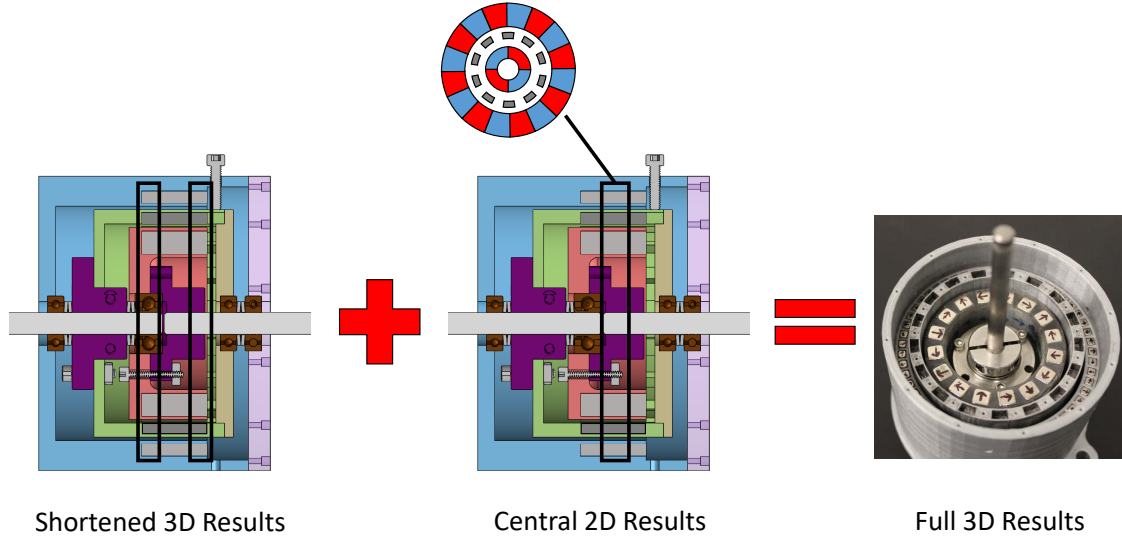


Figure 3.1: Sections of the magnetic gear that are estimated by each step of the reduced length modeling method. The two symmetric sections that experience end-effects in the first step are brought together to create a symmetric reduced length 3D model.

The purpose of modeling magnetic gears in 3D is to quantify the axial variation in flux density that occurs due to end-effects. However, the axial variation does not occur over the entire axial length of the gear as shown in Figure 3.2. The portion of the gear that experiences axial variation in flux density is referred to as the nonlinear region and the portion which does not experience axial variation is referred to as the linear region. Torque generated by the nonlinear region of the gear can be accurately estimated by a 3D model of shorter axial length which has a considerably smaller linear region than the original gear model. The torque lost from shortening this linear region is compensated by a supplemental 2D model which runs locally in a

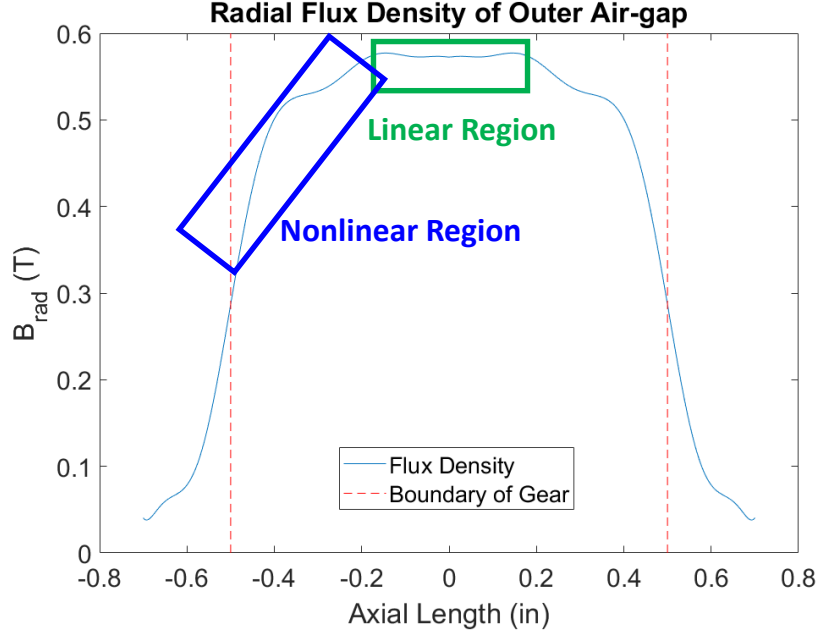


Figure 3.2: Flux density profile that displays the constant linear region and the decreasing nonlinear region. Radial flux density of the outer air gap is shown, but this trend exists to some extent at all locations for both radial and tangential flux density.

matter of seconds. This 2D model is able to accurately estimate torque generated by the linear region because flux density in that region is relatively constant in that region.

The benefits to modeling with this method are a reduction in computation time and the ability to run certain models which would have previously been too large to solve. The scaling of COMSOL solution time with respect to model size as defined by degrees of freedom (dof) is shown in Figure 3.3. It is noted that the scaling of computation time is greater than linear. This trend occurs because a damped Newton solver is used for solution of the COMSOL models. The Newton method for the solution of a system of nonlinear PDEs involves the use of an  $n \times n$  Jacobian



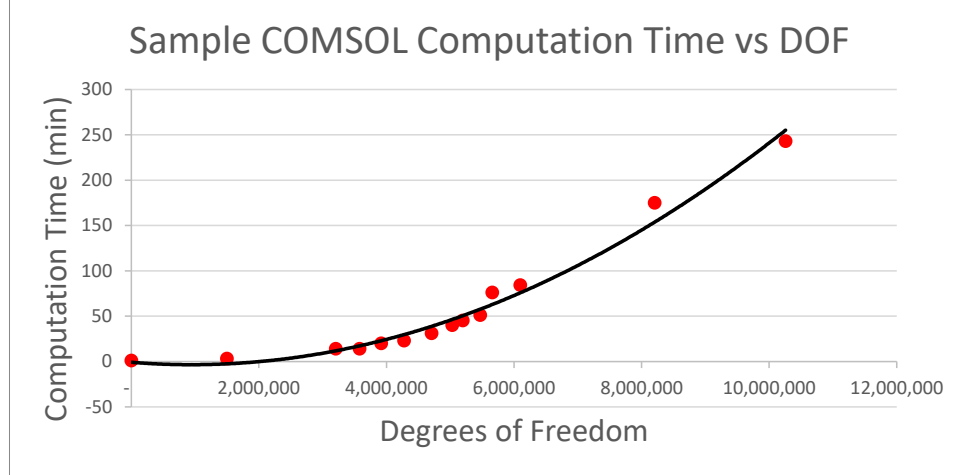


Figure 3.3: Example of the computation time scaling trend as the size or mesh refinement of a magnetic gear model is increased. This plot was created using the default COMSOL solver and fixed computational resources.

matrix where  $n$  is the number of nodes in the system. When a node is added to the system, the Jacobian matrix grows both in the number of equations that must be solved and also in the number of variables for each equation. This dual growth is why computation time increases disproportionately when the element number of a model increases.

The greater than linear scaling means that computation time can greatly increase if the degrees of freedom become too large. The degrees of freedom are defined by the number of elements, the type of elements, and the discretization of the magnetic vector potential (linear, quadratic, etc.). Nonlinear computational scaling means that significant reductions can be made to computation time by making moderate reductions to model size as suggested in the reduced length modeling method. Any reduction in the size of the model leads to a reduction in the number of elements

which reduces solution time. It is worthwhile to note that additional time savings can be made when working through an independent supercomputing center like Ohio Supercomputer Center (OSC) that uses a queue system. When the solution time is lower, less computational resources can be requested which gives added priority in the queue. This means that less time is spent waiting for a project to leave the queue for solution.

The other primary benefit to modeling with the reduced length method is that this method reduces the memory requirements for solution of the system. Several steps of the FEM process can be fairly intensive from a memory standpoint, and solution of the system fails if available memory is exceeded during any of these steps [12]. The first of these steps is the meshing process which can take significant memory to calculate and store node locations. The second step is the assembly of the system matrix which creates a very large matrix with factors defined at each node depending on the constitutive equations. The final step is the solution of the system matrix which always requires more memory than it takes to store the matrix. The memory requirements of each step listed here can be reduced by decreasing the geometric size of the model, thus lowering the number of elements.

The drawbacks to using the reduced length modeling technique are that the output torque is always overestimated to some extent and that there must be some knowledge of a particular magnetic gear design's susceptibility to end-effects. Output torque is always overestimated when using this modeling technique because a "perfect" 2D model is used to estimate output torque contribution of the axially central portion of the gear. In a full 3D model there would be an axial reluctance component which would slightly reduce torque contribution of this region. The significance of end effects

must also be understood. This understanding will inform how much axial length must be included in the reduced length 3D model to accurately describe the end-effect losses. The next section lays groundwork to estimate the prevalence of these losses for a concentric gear design which utilizes Halbach arrays on both magnet rotors.

### 3.2 Variable Sensitivity

To create a multi-variable correlation between many magnetic gear design variables would be an intensive undertaking unsuited for this thesis given the other content included. For this reason, this section looks at the effect of single variable correlation to the end-effect ratio or ratio of 3D torque to 2D torque. End-effect ratio is being used as a metric to quantify the significance of the end-effect losses. If the end-effect ratio is low, then it is assumed that a larger axial length of the magnetic gear must be modeled in 3D to quantify the severe end-effect losses.

For this modeling exercise, the NASA PT-1 cross-sectional geometry was utilized with a singular swept design variable for both 2D and 3D COMSOL models [2]. The swept design variable will depend on the section. Figure 3.4 can be referenced for the cross-sectional geometry of PT-1. The design and performance characteristics of PT-1 can be found in Table 3.1. Unless otherwise specified, the design variables listed in Table 3.1 will be used for all simulations in Chapter 3.

The weight and specific torque values listed in Table 3.1 differ from what is found in the literature because of the way PT-1 weight is considered in this thesis. Weight is determined by calculating weight of the extruded cross-section shown in Figure 3.4. This means that weight is greater than the active magnetic mass (because rotor structural material is included), but less than the total mass reported in the literature

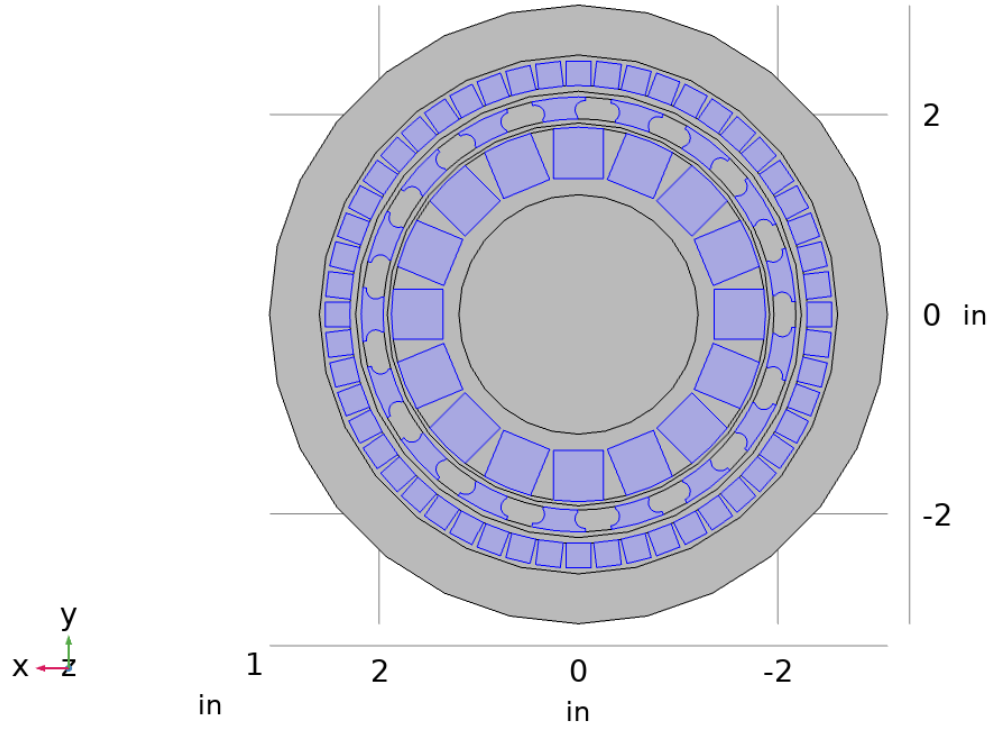


Figure 3.4: Cross-sectional geometry for NASA's PT-1 magnetic gear design. All magnetically active components are highlighted in blue.

(because structural material like the shaft and bearings are not included). The mass and specific torque of PT-1 becomes relevant for the specific torque improvements in Chapter 4.

Table 3.1: Design and performance characteristics for the NASA PT-1.

Characteristic	Metric	English
Gear Ratio	4.25	
Inner Pole-Pairs	4	
Outer Pole-Pairs	13	
Modulator Pieces	17	
Magnets per Inner Pole-Pair	4	
Magnets per Outer Pole-Pair	4	
Outer Radius	64.5 mm	2.54 in
Outer Magnet Thickness	6.35 mm	0.25 in
Outer Air Gap Thickness	2.88 mm	0.113 in
Modulator Thickness	5.59 mm	0.220 in
Inner Air Gap Thickness	2.12 mm	0.0835 in
Inner Magnet Thickness	12.7 mm	0.5 in
Axial Length	25.4 mm	1.0 in
Weight	1.135 kg	2.502 lbm
3D COMSOL Specific Torque	29.3 N*m/kg	9.82 ft*lb/lbm
3D COMSOL Torque	33.3 N*m	24.6 ft*lb
2D COMSOL Torque	53.0 N*m	39.1 ft*lb
End-Effect Factor	62.8%	
Experimental Torque	34.0 N*m	25.1 ft*lb

### 3.2.1 Axial Length

Axial length is expected to have a strong correlation with end-effect ratio because the axial length of the magnetic gear determines what percentage of the magnetic gear length is influenced by the high reluctance axial air domain at the axial ends of the gear. The presence of an axial air domain is what allows for end-effects to exist. Figure 3.5 shows axial length scaling trends that can provide some insight into how end-effect ratio scales with respect to axial length.

It can be seen that output torque from the 2D model has a linear scaling trend with respect to axial length. This is to be expected because the 2D models assume

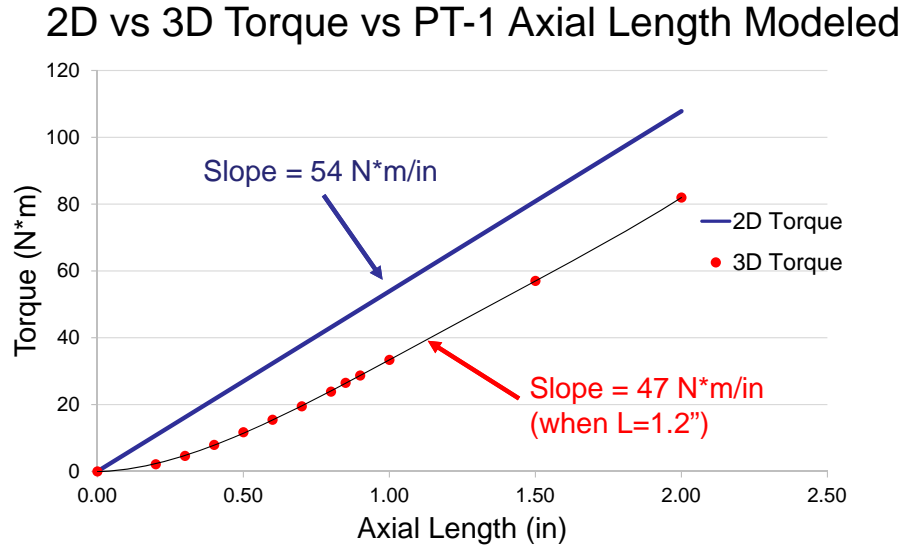


Figure 3.5: Scaling of output torque for 2D and 3D models per unit of axial length modeled up to 2" (50.8 mm).

that there is no axial variation in magnetic flux density. When there is no axial variation in flux density, torque can be calculated by accounting for the axial length with a simple linear scaling. In regards to 3D torque, the scaling with respect to axial length is asymptotic in nature. The 3D torque rate of change with respect to axial length starts out quite small when the axial length is small, but as the axial length becomes large, the rate of change approaches the 2D torque rate of change with respect to axial length. By the time axial length has reached 1.2" (30.5 mm), the 3D torque rate of change is already 47 N\*m/in. This rate of change was calculated from a 4th order polynomial function that was developed from the scatter plot shown in Figure 3.5. This rate of change is only 7 N\*m/in less than the 2D torque scaling of 54 N\*m/in.

The 3D rate of change is low when axially short because when the magnetic gear is axially short, the high reluctance of the air domains at the axial ends of the gear is significant with respect to the total reluctance of the magnetic gear system. When the magnetic gear is axially long, these regions of high reluctance have a relatively low impact on the overall reluctance of the magnetic gear system and rate of change nears the 2D value.

The “magnetic gear system” can be thought of as a network of discrete, equidistant reluctances in a 3D space. The axial length of the magnetic gear determines what percentage of these discrete reluctances comprise reluctances from the axial air domain. Figure 3.6 illustrates this effect by showing how the end-effect factor increases as the axial length increases. The end-effect factor  $E_T$  is defined as,

$$E_T = \frac{T_{3D}}{T_{2D}} \quad (3.1)$$

where  $T_{3D}$  is torque from a 3D simulation and  $T_{2D}$  is torque from a 2D simulation. The ratio of these values serves as a measure of end-effect severity.

As described, the end-effect factor begins very small when the axial length of the gear is short. As the gear increases in axial length, the end-effect factor drastically increases as the axial air domain becomes a less significant component of the system’s reluctance. As the gear gets longer, equivalent increases in axial length provide a lower increase in the end-effect factor because the same increase in length has a lower impact on percentage contribution to reluctance in the system. For example, the end-effect factor increases from 20% at an axial length of 0.2” (5.08 mm) to 43% at an axial length of 0.5” (12.7 mm). This is an axial length increase of 0.3” (7.62 mm) which correlates to an end-effect factor increase of 23%. An equivalent axial length increase (from 1.7” (43.2 mm) to 2.0” (50.8 mm)) only increases the end-effect factor by 3%.

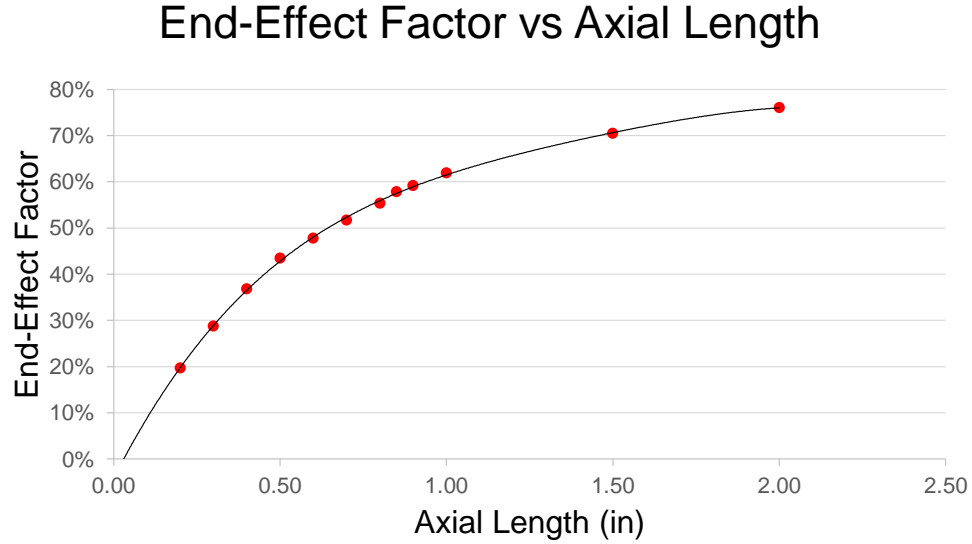


Figure 3.6: End-effect factor scaling of a coaxial magnetic gear as the axial length is increased.

If the axial length shown in Figure 3.6 is taken to infinity, the limit of the end-effect factor approaches 100% because the axial air domain will become an infinitesimal contributor to system reluctance.

### 3.2.2 Magnetic Air Gap Thickness

The variable of analysis in this section is the magnetic air gap thickness. The magnetic air gaps of a magnetic gear can be separated into an inner and an outer air gap. The inner air gap is the distance from the outer face of the inner rotor to the inner face of the flux modulator, while the outer air gap is the distance from the outer face of the flux modulator to the inner face of the outer rotor. When the air gap thickness is modified for these trials, it is done by modifying the inner rotor's outer face radius and the outer rotor's inner face radius. A variable has been introduced to



scale the air gaps equally. This variable is the magnetic air gap scaling factor  $X_{AG}$  and scales according to,

$$t_{IAG} = t_{IAGbase} * X_{AG} \quad (3.2)$$

and

$$t_{OAG} = t_{OAGbase} * X_{AG} \quad (3.3)$$

where  $t_{IAG}$  is the inner air gap thickness,  $t_{IAGbase}$  is the inner air gap thickness of the base mode,  $t_{OAG}$  is the outer air gap thickness, and  $t_{OAGbase}$  is the outer air gap thickness of the base model. The base PT-1 magnetic gear has an inner air gap thickness of 2.12 mm (0.835”) and an outer air gap thickness of 2.88 mm (0.113”). All other component thicknesses remain constant.

It is noted that in magnetic gear design there is a clear difference between the terms “magnetic air gap” and “physical air gap” or just “air gap”. The “magnetic air gap” specifically refers to the radial distance between magnetically active components whereas “physical air gap” or “air gap” refers to the radial distance of air between gear components. For all gear models presented in this thesis, there is only air located in the radial space between magnetically active components. For this reason, all references to the “air gap” should be understood to be both the physical and magnetic air gap. This is not true for all magnetic gear design because sometimes non-magnetically active materials are added to the air gap for structural support.

These air gaps are expected to have an impact on the end-effect factor because of how they influence the radial reluctance of the magnetic gear. When the air gaps are large, the radial reluctance is high; when the air gaps are small, the radial reluctance is low. Figure 3.7 shows how this variation in radial reluctance leads to different

radial flux density profiles for the outer air gap of a 3D magnetic gear simulation based on PT-1.

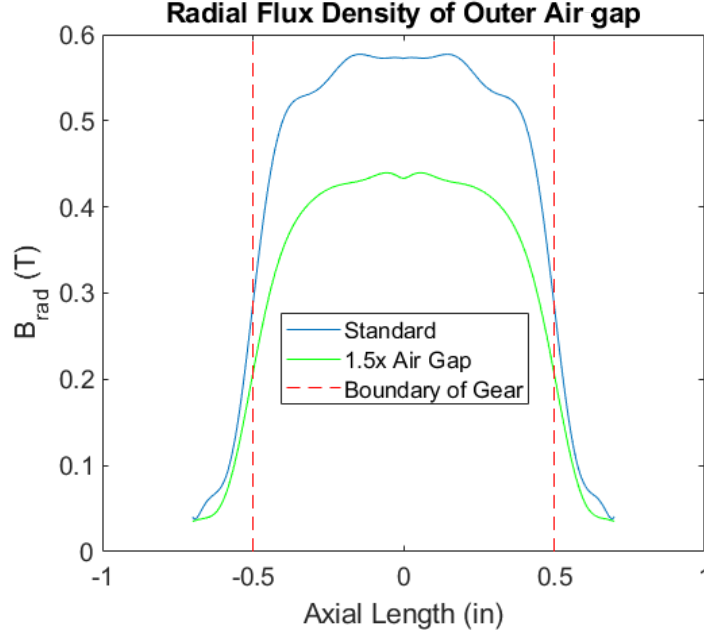


Figure 3.7: Comparison of the standard PT-1 flux density profile to a version of PT-1 that has 1.5x thicker air gaps.

This plot shows both that peak flux density decreases in the outer air gap when the magnetic air gap is increased, and also that the linear region becomes slightly smaller when the magnetic air gap is increased. This trend is shown for the outer air gap but also exists for the inner air gap. These results would indicate both a decrease in 3D torque because of the decreased peak flux density, and also a greater relative disparity between 3D and 2D torque for the case with a larger magnetic air gap because the linear region is smaller. As mentioned previously, a 2D model would

be represented as a purely linear region with no axial flux density variation, so the further from a pure linear region the 3D model is, the lower the end-effect factor is. This concept is further illustrated in Figures 3.8 and 3.9.

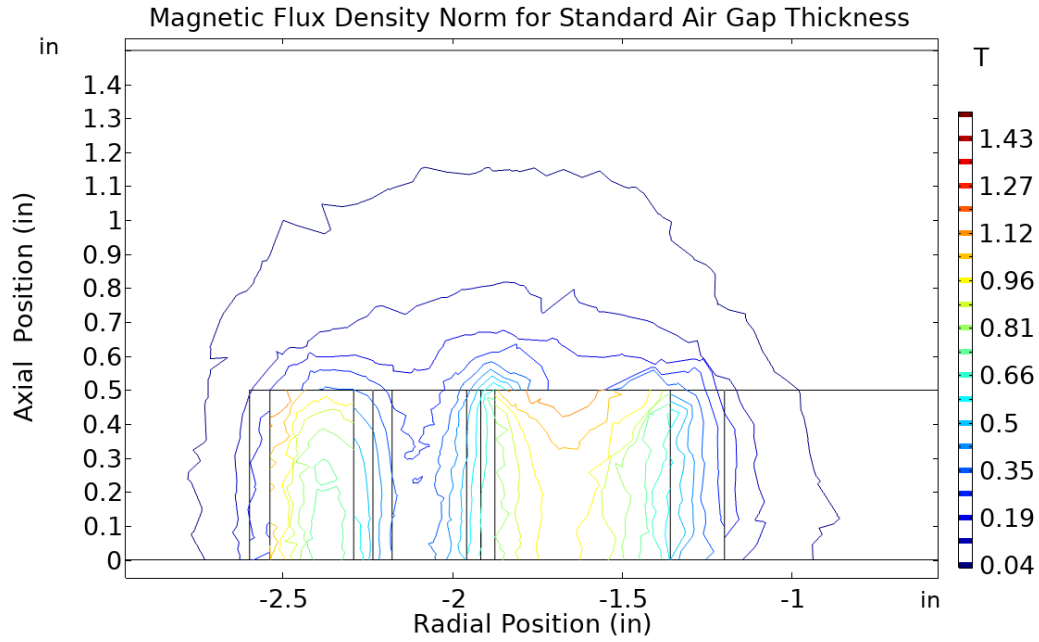


Figure 3.8: Contour of the magnetic flux density norm shown on an axial cross section of the original PT-1.

Figure 3.8 shows a greater peak magnetic flux density norm (1.43 T) than Figure 3.9 (1.14 T). This is consistent with the radial flux density results from Figure 3.7. Figure 3.8 also shows less axial flux density leakage than Figure 3.9. The 0.04 T contour line leaks all the way up to the end of the axial air domain at 1.5" (38.1 mm) only in Figure 3.9. This is because when radial reluctance is increased, the axial circuit becomes a more appealing path for flux to travel.

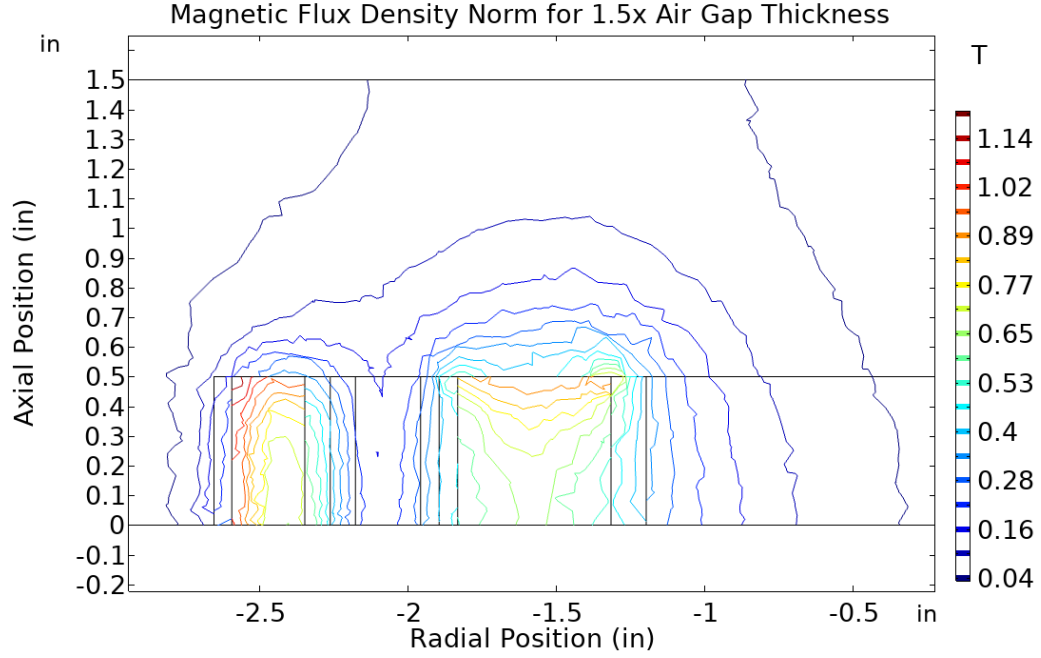


Figure 3.9: Contour of the magnetic flux density norm shown on an axial cross section of a modified PT-1 with 1.5x thicker magnetic air gaps.

Figure 3.10 shows how increasing the magnetic air gap thicknesses leads to decreased torque output for both 2D and 3D models. These results are consistent with the magnetic flux density contours which show lower flux density for the model with a larger magnetic air gap.

Figure 3.11 shows how the end-effect factor decreases with a linear trend as the magnetic air gap is increased. The trend is confirmed by the linear fit shown with an R squared value of 0.9729. These results are consistent with the understood theory because an increased radial reluctance increases flux preference for the axial path as shown in Figures 3.8 and 3.9. The smallest air gaps in these trials correlate to a 0.423

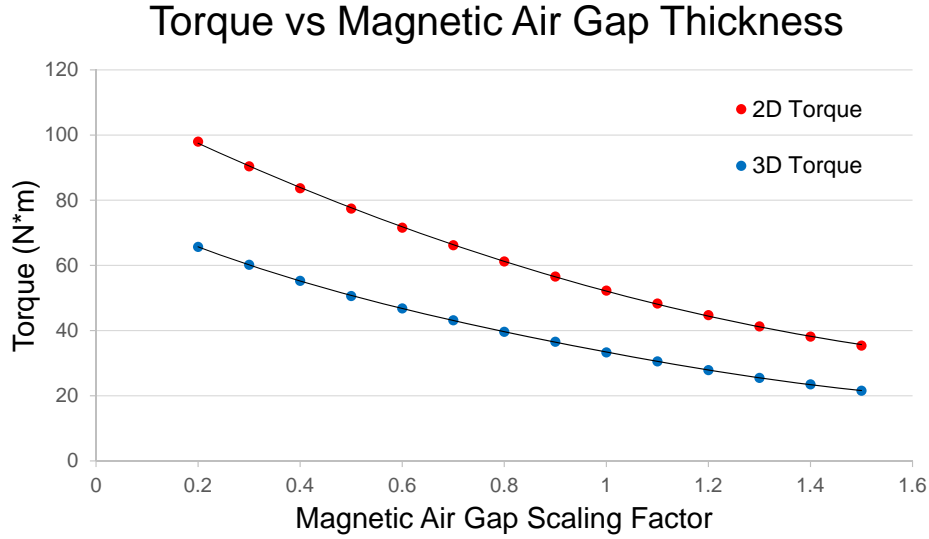


Figure 3.10: Scaling of output torque for 2D and 3D models as the inner and outer magnetic air gaps are equally scaled.

mm (0.167") inner air gap and a 0.576 mm (0.0227") outer air gap while the largest are 3.17 mm (0.125") and 4.32 mm (0.170") respectively. This is a relatively large sweep that only correlates to a 6.1% variance in the end-effect factor. The small variance indicates that the magnetic air gap thickness is not a particularly influential variable when analyzing end-effect significance compared to a variable like axial length.

There were some concerns regarding the use of square shaped magnets for these simulations and their potential effect on the results. Square magnets were used in the design of PT-1, but they are not ideal for identifying magnetic gear performance trends because they are hardly ever used beyond preliminary prototyping. These

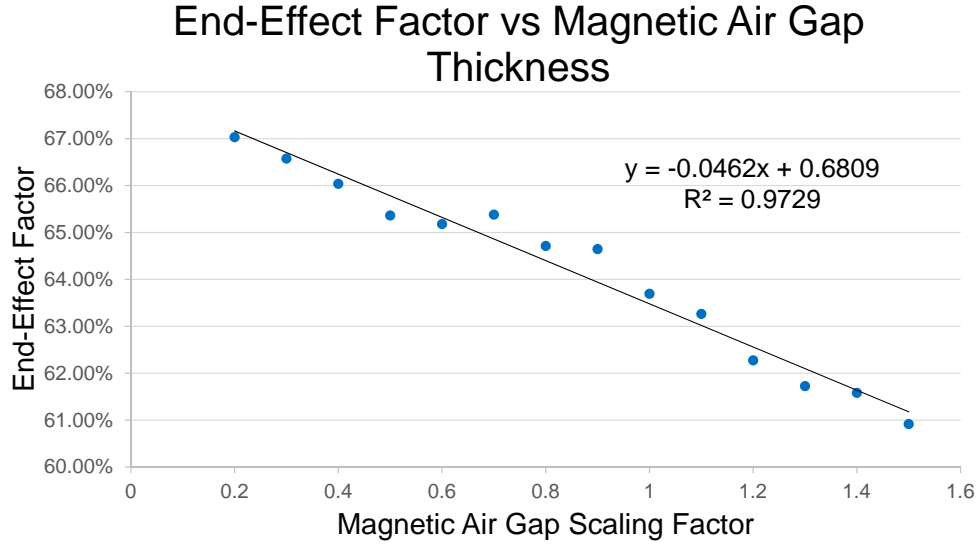


Figure 3.11: Scaling of the end-effect factor as the inner and outer magnetic air gaps are equally scaled.

square magnets use available gear space less efficiently than traditional curved magnets and produce a less sinusoidal flux density waveform. It is for these reasons that the simulations were rerun with curved magnets instead of square magnets.

Figure 3.12 shows how the magnet geometry was modified to a more conventional arc magnet design. This modification was made by equally extending the square magnets into their adjacent dividers. A dividing region like this would be necessary for an experimental model because of structural concerns, (even when using arc magnets) but these models exclude the dividing region because it should not affect the scaling trends. The torque results from these redone simulations can be found in Figure 3.13.

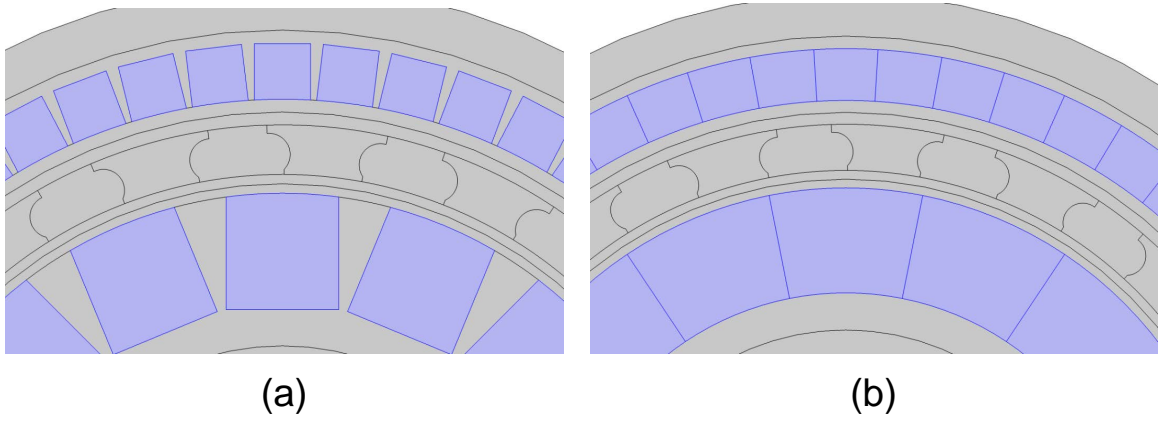


Figure 3.12: (a) Original square magnets used for PT-1; (b) modified curved magnets used for scaling analysis.

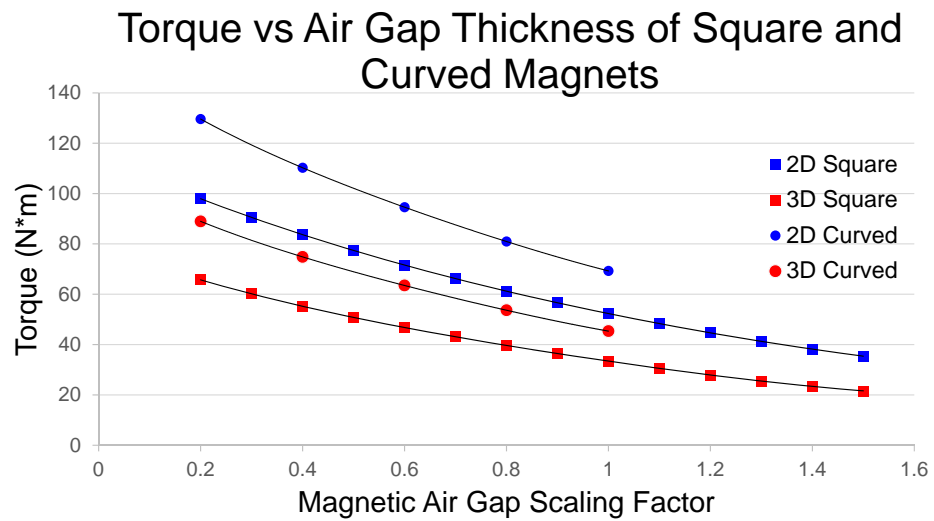


Figure 3.13: Comparison of torque results for 2D and 3D models when using square vs curved magnets.

As expected, the magnetic gear models that utilize curved magnets show higher torque results due to greater magnet volume and a more sinusoidal flux density waveform. It is observed that although the torques are greater, the scaling trends do not appear to be particularly different. This same trend can be seen with respect to the end-effect factor in Figure 3.14.

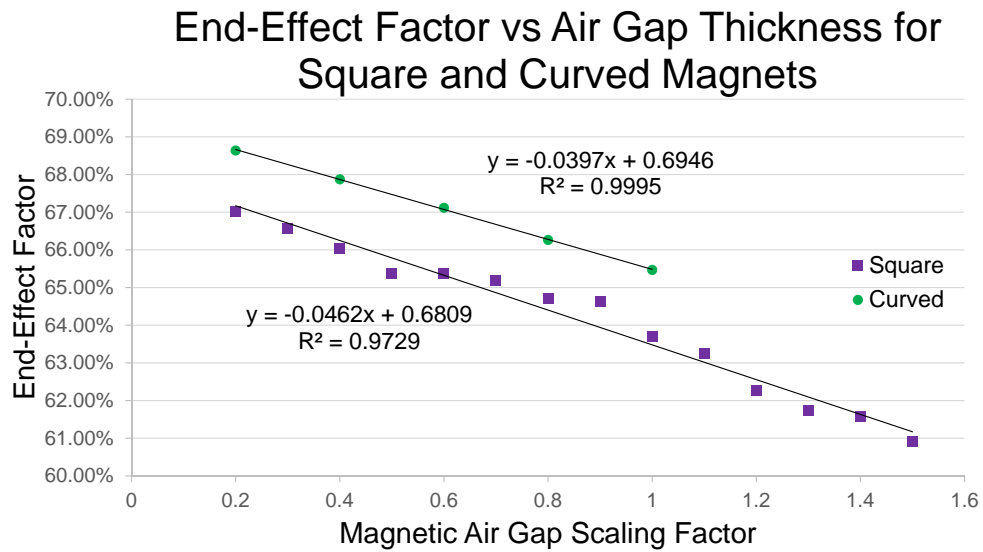


Figure 3.14: Comparison of end-effect factor results for 2D and 3D models when using square vs curved magnets.

Although the end-effect factor values from the curved magnet simulations are higher, these results seem to mostly be offset by a constant bias which leads them to show the same trend as the square magnet simulations. Both data sets show a strong correlation with the linear regression ( $R^2$  is 0.9729 for the square magnets and 0.9995 for the curved), and they show similar slopes (-0.0462 for the



square magnets and -0.0397 for the curved). Due to the results of Figures 3.13 and 3.14, it has been concluded that the use of curved magnets vs square magnets does not affect the scaling trends explored in this thesis. Curved magnets continue to be used for the remainder of the reduced length modeling section because they are more representative of practical magnetic gear prototypes.

### 3.2.3 Outer Radius

Before discussing the relationship between end-effect factor and radial scaling, it is useful to understand the mechanisms of how torque is generated in a magnetic gear and how these mechanisms can relate to radius. Figure 3.15 illustrates distance from the central axis and slip force, two mechanisms that can be used to conceptualize torque generation.

The slip force is the tangential force applied at the output component that would be required to exceed the maximum tangential force generated by the magnetic interactions of the gear. When exceeded, a phenomenon known as slip occurs in which the output component is unable to follow the relative radial positions of the other components at which maximum force and torque are generated [9]. The slip force, in addition to the moment arm at which it is applied, is what defines the output torque. The output torque can also be defined as slip torque. In much the same way as slip force, the slip torque is the torque applied to the output component that would be required to exceed the maximum tangential force generated by the magnetic interactions of the gear acting roughly at the output component radius. This explanation of torque is described mathematically by (1.11).

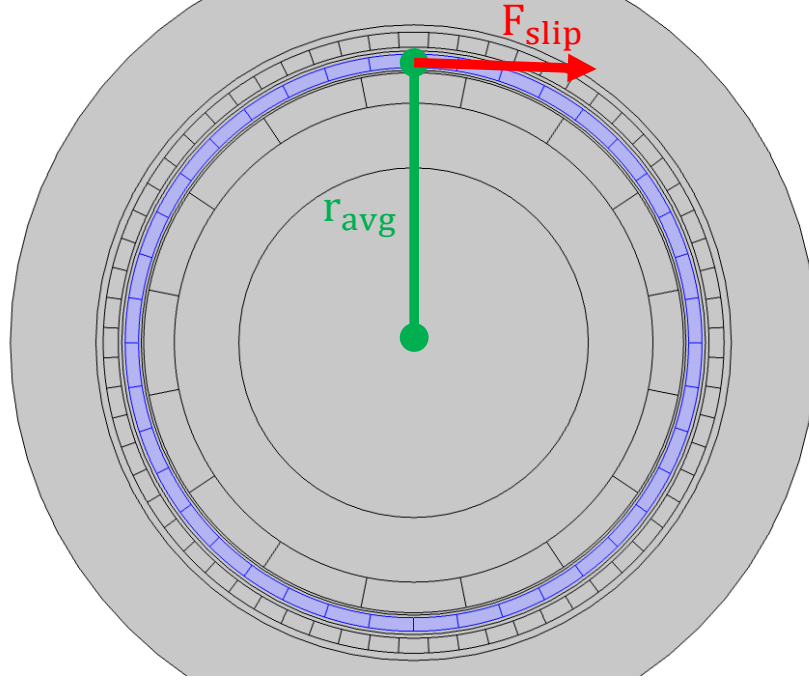


Figure 3.15: Average radius of the flux modulator and slip force of the flux modulator shown to conceptualize the elements that contribute to output torque.

The stated torque theory shows the unique opportunity provided by radial scaling to increase both slip force and length of the moment arm at the same time. It is unique because it is the only geometric scaling that squares output torque. The slip force can be increased by adding additional pole-pairs as the circumference increases, and the moment arm increases linearly with the radius. The increase of slip force due to increased pole-pairs is explained more in Subsection 3.2.4 which deals with pole-pair scaling. This section does not scale the pole-pairs along with the radius, and as a result, the slip force of the gear does not increase.

Figure 3.16 shows exactly how the magnetic gear outer radius is scaled for the following trials. The outer radius of the outer rotor is varied while the thicknesses

of all components and air gaps are kept constant. The circumferential length of the magnets are increased to account for the increased radius with constant pole-pair numbers. The modulator piece shape has also been changed to a simpler geometry to better accommodate radial scaling. Figure 3.13 shows the original modulator pieces which utilize unusual cuts out of the side of the modulator piece. For proceeding simulations in this section, the modulator pieces have straight sides with a single span angle such that it represents the modulator pieces of a more general magnetic gear. Simulations in this subsection use a gear ratio of 5 with 4 inner rotor pole-pairs, 16 outer rotor pole-pairs, and 20 flux modulator pieces. Pole-pair number was changed to create periodic symmetry with respect to angular position for the goal of reducing model size.

It can be seen in Figure 3.17 that both the 2D and 3D torques scale as linear. They show high R squared values of 0.9934 and 0.9835 respectively. Linear scaling is consistent with the theory that only the moment arm length would be scaled along with the outer radius. The slight deviation from linear scaling could be due to complexities of scaling the outer radius with constant thicknesses, or possibly a less sinusoidal flux density waveform as radius is scaled up with a constant number of magnets.

It was found that the end-effect factor decreases as radius increases. This result is shown in Figure 3.18. The end-effect factor variation is due to the effect that radial scaling has on the reluctance between pole-pairs. When the radius is scaled up, all other variables held equal, it increases the linear distance between adjacent pole-pairs on the same rotor. The linear distance is comprised of low permeability substances like air and magnet material, so the reluctance between these pole-pairs

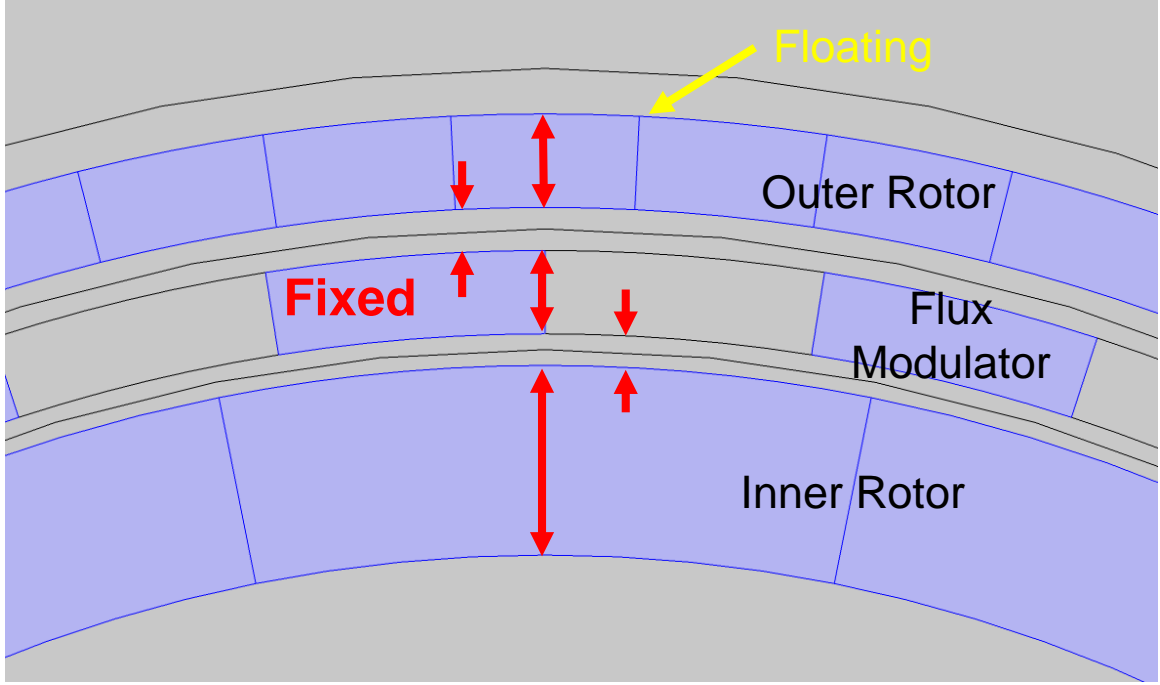


Figure 3.16: Illustration of how the magnetic gear radius is scaled. The outer radius of the outer rotor is varied while the component and air gap thicknesses are kept fixed.

increases significantly. Increasing reluctance between adjacent pole-pairs reduces in-plane leakage which increases the relative significance of axial leakage as an inefficiency of the magnetic network. This ultimately leads to a greater disparity in output torque between the 2D and 3D models and reduces the end-effect factor as radius increases.

In-plane leakage is a concept that plays a significant role in noted trends with respect to the end-effect factor. In-plane leakage is a magnetic inefficiency present in both 2D and 3D models where flux does not couple in the flux modulator to produce torque, but instead leaks back to its original rotor through the xy-plane. This can happen both by leaking to adjacent pole-pairs on the same rotor and also by leaking back through the magnet of origin. The loss of useful flux via these mechanisms often

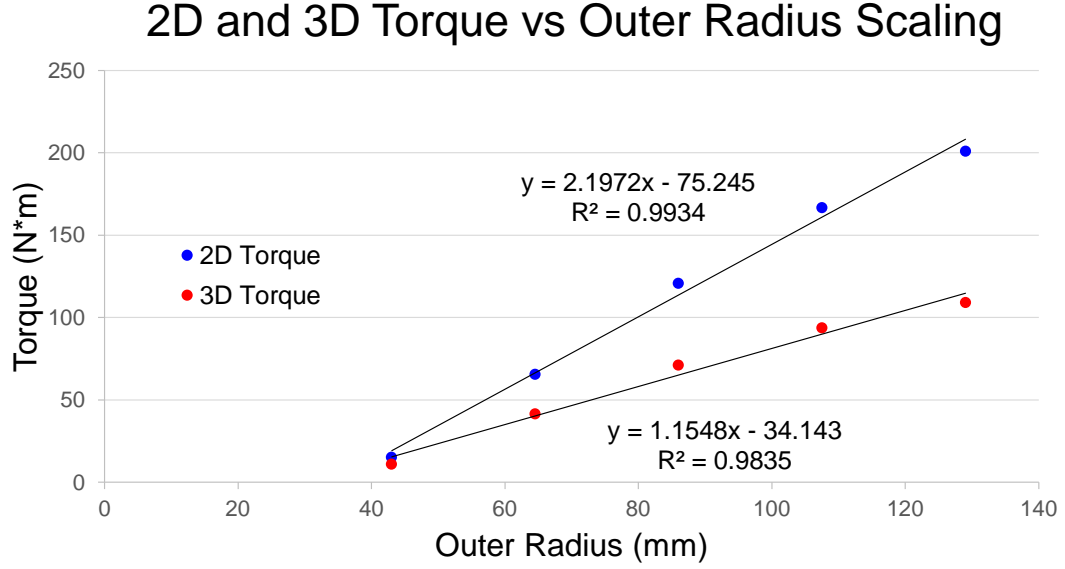


Figure 3.17: 2D and 3D torque results as the outer radius of the gear was scaled with no change to pole-pair number.

correlates with reduced torque output and an increased end-effect factor because it makes axial leakage less significant.

One concern with running the radial scaling trials was that the varying radius may skew the flux density waveform produced by the Halbach arrays. This could theoretically create variation between the radial scaling trials that could not be attributed directly to the changing radius. To normalize the Halbach waveform shape and isolate the variable of outer radius, a modification was made to the models in which the Halbach arrays were undiscretized and made into a continuous magnet ring.

The discretization modification is shown in Figure 3.19. The rings that replace the individual magnets are assigned a remanent flux density that varies by angular position in accordance with,

$$B_{rad} = B_r * \cos(\theta * p_{IR}) \quad (3.4)$$

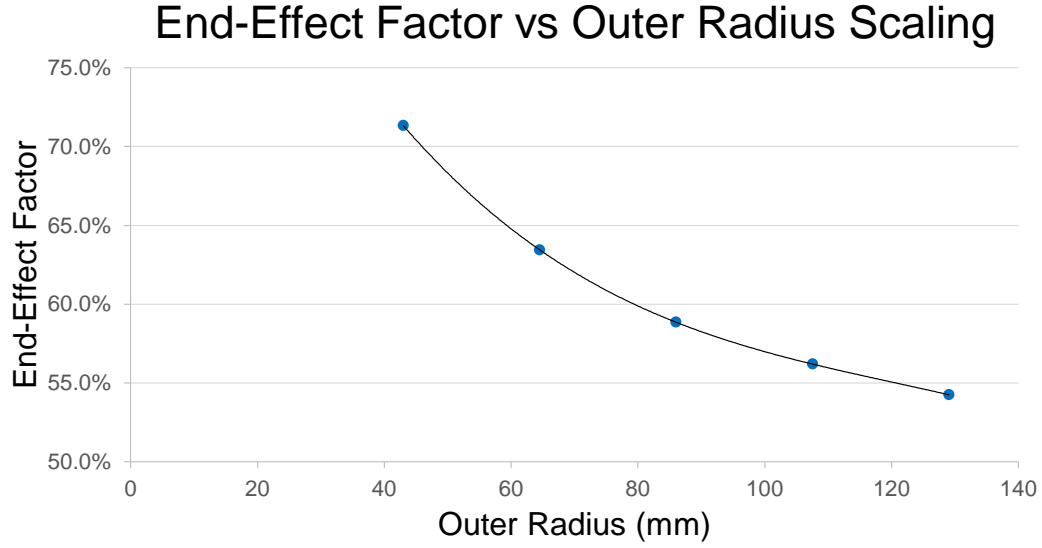


Figure 3.18: End-effect factor results as the outer radius of the gear was scaled with no change to pole-pair number.

and

$$B_{tan} = -B_r * \sin(\theta * p_{IR}) \quad (3.5)$$

for the inner rotor where  $B_{tan}$  is the radial magnetic flux density,  $B_r$  is the remanent flux density,  $\theta$  is the angular position,  $p_{IR}$  is the number of inner rotor pole-pairs, and  $B_{tan}$  is the tangential magnetic flux density. The outer rotor equations are,

$$B_{rad} = B_r * \cos(\theta * p_{OR}) \quad (3.6)$$

and

$$B_{tan} = B_r * \sin(\theta * p_{OR}) \quad (3.7)$$

where  $p_{OR}$  is the number of outer rotor pole-pairs. These equations generate continuous Halbach arrays over the circumference of the magnet rings as opposed to discrete magnets of single magnetization vectors. Images (c) and (d) of Figure 3.19

show how the modification leads to a more sinusoidal flux density waveform. By having ideal flux density waveforms for rotors of every radius, the variable of Halbach discretization is normalized for all trials.

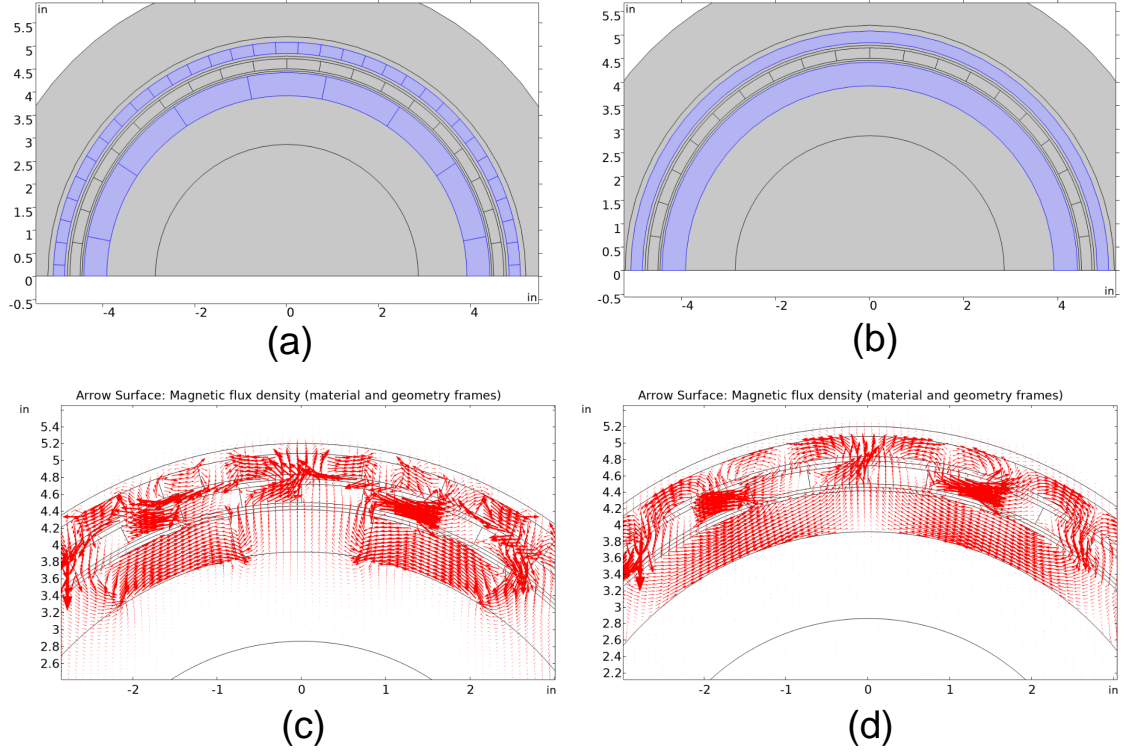


Figure 3.19: (a) Discretized magnet geometry for one of the radius model; (b) non-discretized magnet geometry for the same radius model; (c) flux lines associated with “a”; (d) flux lines associated with “b”.

Figure 3.20 shows the torque results for both the discretized and non-discretized Halbach arrays. As expected, the use of ideal Halbach arrays increases the torque generated by both the 2D and 3D models. It is necessary to note that both types of models still show a similar linear scaling trend despite now scaling torque faster.

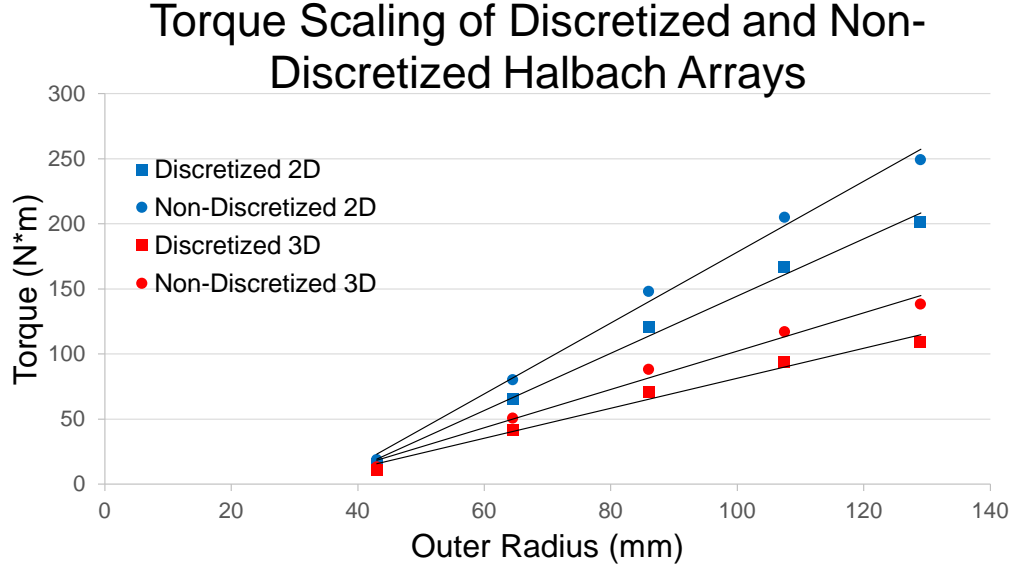


Figure 3.20: 2D and 3D torque results for magnetic gears with discretized and non-discretized Halbach arrays.

It can be seen in Figure 3.21 that the non-discretization change had an insignificant effect on the scaling of the end-effect factor with respect to outer radius. Despite having an insignificant effect on end-effect scaling, the non-discretization modification is again applied to the pole-pair scaling trials in Section 3.2.4 to ensure that the flux density waveform is normalized.



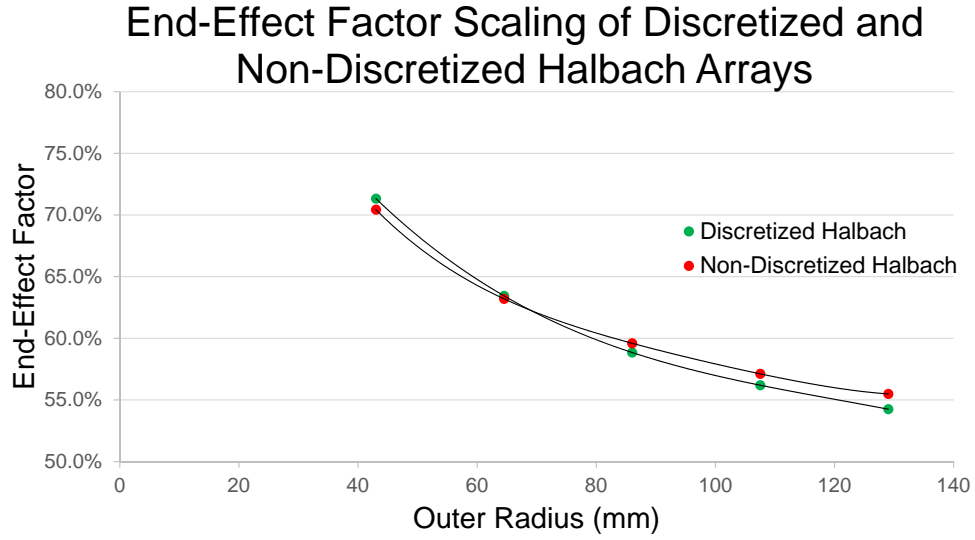


Figure 3.21: End-effect factor results for magnetic gears with discretized and non-discretized Halbach arrays.

Based on the final non-discretized end-effect results, it has been concluded that radius is a significant contributor to the end-effect factor. Outer radius was swept from 43 mm (1.69") to 129 mm (5.08") and an end-effect factor variation of 14.9% was found. The end-effect factor was found to be especially sensitive to radius scaling at low radii while gradually becoming less sensitive as the radius increased based on results from Figure 3.21.

### 3.2.4 Pole-Pair Scaling Factor

Pole-pair scaling is expected to have a correlation to the end-effect factor because modifying the number of pole-pairs changes the reluctance between pole-pairs. When

the number of pole-pairs is increased for a given rotor, the reluctance between pole-pairs decreases. When the number of pole-pairs is decreased for a given rotor, the reluctance between pole-pairs increases. Figure 3.22 shows how the pole-pairs are scaled for these trials.

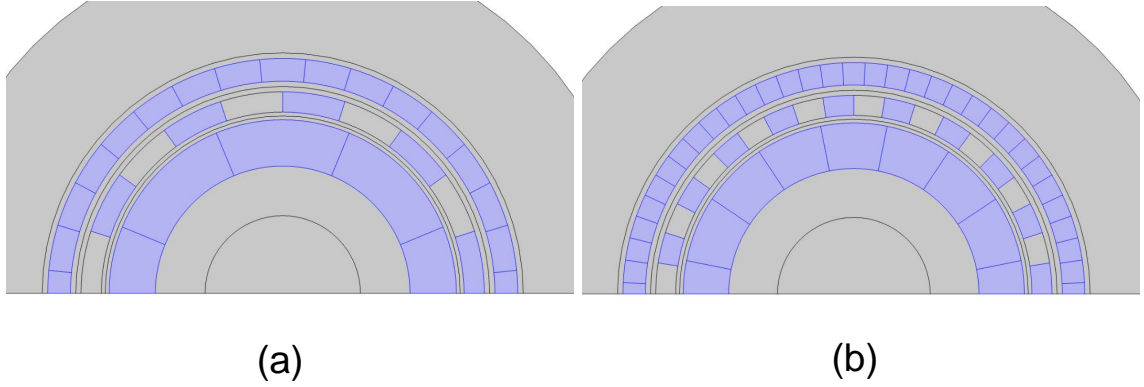


Figure 3.22: All magnetically active components are highlighted in blue; (a) Base model for the following pole-pair trials with 2 inner rotor pole-pairs and 8 outer rotor pole-pairs (4 magnets per pole-pair); (b) pole-pair model with a pole-pair scaling factor of 2. The model has 4 inner rotor pole-pairs and 16 outer rotor pole-pairs.

A variable has been introduced to scale the rotor pole-pairs equally. This variable is the pole-pair scaling factor  $X_{PP}$  and is described by,

$$p_{IR} = p_{IRbase} * X_{PP} \quad (3.8)$$

and

$$p_{OR} = p_{ORbase} * X_{PP} \quad (3.9)$$

where  $p_{IRbase}$  is the base number of inner rotor pole-pairs and  $p_{ORbase}$  is the base number of outer rotor pole-pairs. For these trials,  $p_{IRbase}$  equals 2, and  $p_{ORbase}$  equals

8. Note that the increased number of pole-pairs also increases the number of flux modulator pieces.

The torque results for the pole-pair scaling trials can be seen in Figure 3.23. These results for both 2D and 3D torque exhibit an optimal pole-pair scaling factor for maximizing torque. The optimization can be understood by examining,

$$T_c = \frac{\partial W'}{\partial \theta_c} \quad (3.10)$$

where  $T_c$  is the component torque,  $W'$  is the magnetic co-energy, and  $\theta_c$  is the angular position of a specified gear component [15]. For the following analysis, the component of interest is the flux modulator because that is where the output torque is taken.

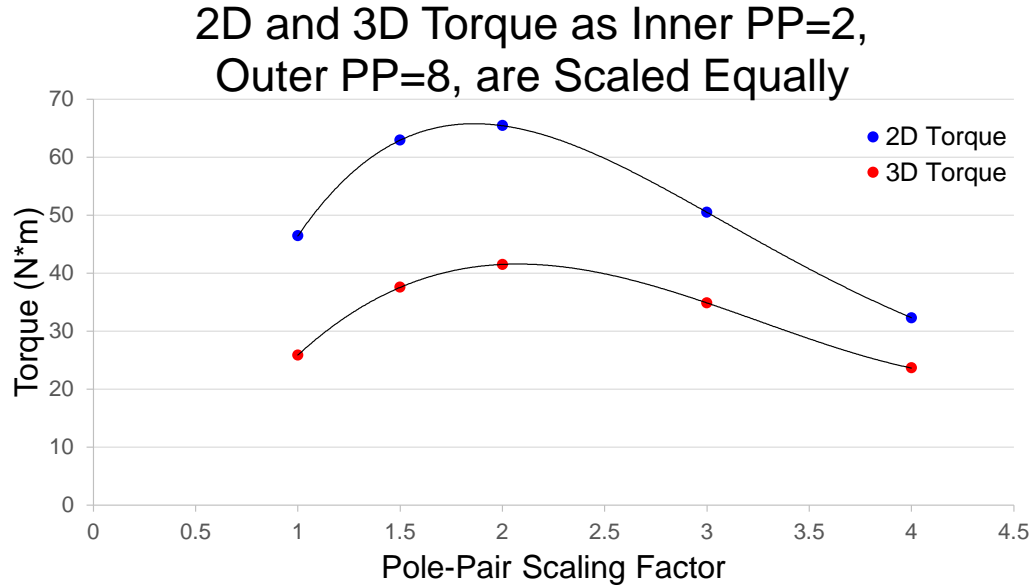


Figure 3.23: 2D and 3D torque results as the pole-pair scaling factor of the gear was varied with no change to any radii or thicknesses.

Eq (3.10) shows that the output torque is a function of the rate of change in magnetic co-energy as the output component is rotated. This means that if peak

magnetic co-energy can be maintained, then increasing the spatial frequency of pole-pairs can increase the rate of change of magnetic co-energy as the component is rotated. Magnetic co-energy is described by,

$$W' = \frac{1}{2\mu} \int_V B^2 dV \quad (3.11)$$

where  $\mu$  is material permeability, and  $B$  is the magnetic flux density. The calculation is more complicated in the COMSOL models used by this thesis because a nonlinear B-H curve is used for the flux modulator material which makes  $\mu$  non-constant. However, generally speaking, if magnetic flux density at the flux modulator can be retained while increasing pole-pair number, then peak magnetic co-energy can be retained. Similar peak magnetic co-energy with a higher spatial frequency means that torque can be increased by increasing the number of pole-pairs. The described torque increase is correlated to the torque shown from a scaling factor of 1 to 2 in Figure 3.23. Torque begins to decrease beyond a scaling factor of 2 because that is the point at which in-plane leakage becomes significant enough to drop peak magnetic co-energy at a faster rate than the increasing spatial frequency.

These torque results correlate to the plot of the end-effect factor shown in Figure 3.24. The plot shows that the end-effect factor increases at a linear rate even beyond the point where torque begins to drop. The R squared fit for the linear regression is 0.9832. The increases of the end-effect factor is due to the increase of in-plane leakage as reluctance between the pole-pairs is reduced. As shown before with the radial scaling trials, this reduces the significance of axial leakage.

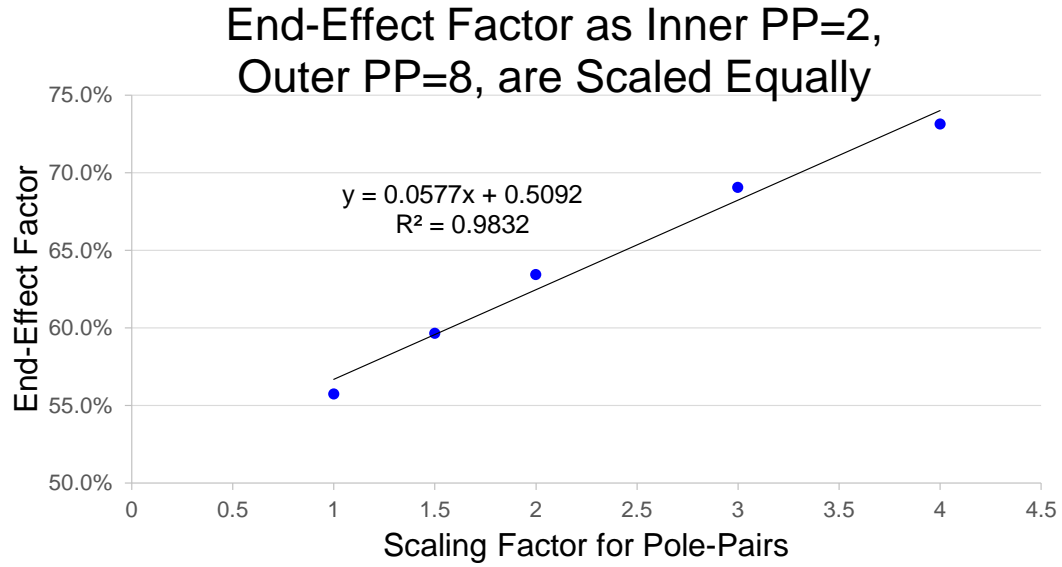


Figure 3.24: End-effect factor results as the pole-pair scaling factor of the gear was varied with no change to any radii or thicknesses.

Like the radial scaling study, these trials were also run with non-discretized Halbach arrays. The torque results of these trials can be seen in Figure 3.25. Again, the more ideal flux density waveforms produced by the non-discretized Halbach arrays contribute to more torque, but do not change the trends of torque with respect to pole-pair scaling.

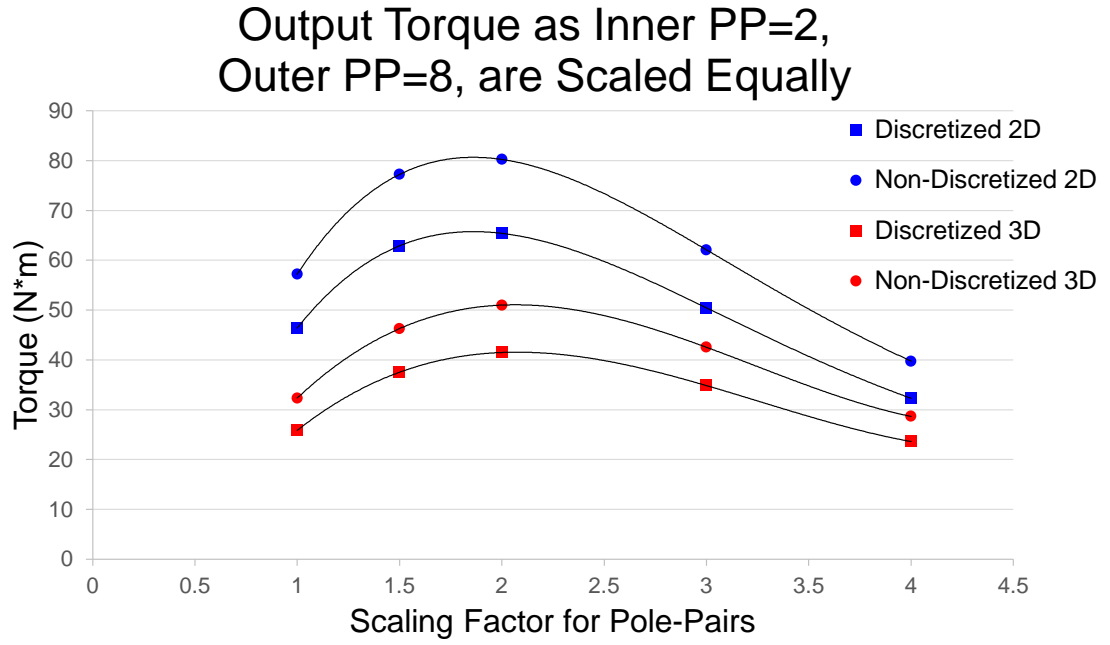


Figure 3.25: 2D and 3D torque results for magnetic gears with discretized and non-discretized Halbach arrays as pole-pair scaling factor was varied.

The end-effect factor shows little difference between discretized and non-discretized Halbach arrays as seen in Figure 3.26. Both data sets have a linear scaling where the discretized trials have an R squared value of 0.9832, and the non-discretized trials have an R squared value of 0.9811. The discretized and non-discretized trials also have a similar scaling rate as their linear regression lines have slopes of 0.0577 and 0.0517 respectively.

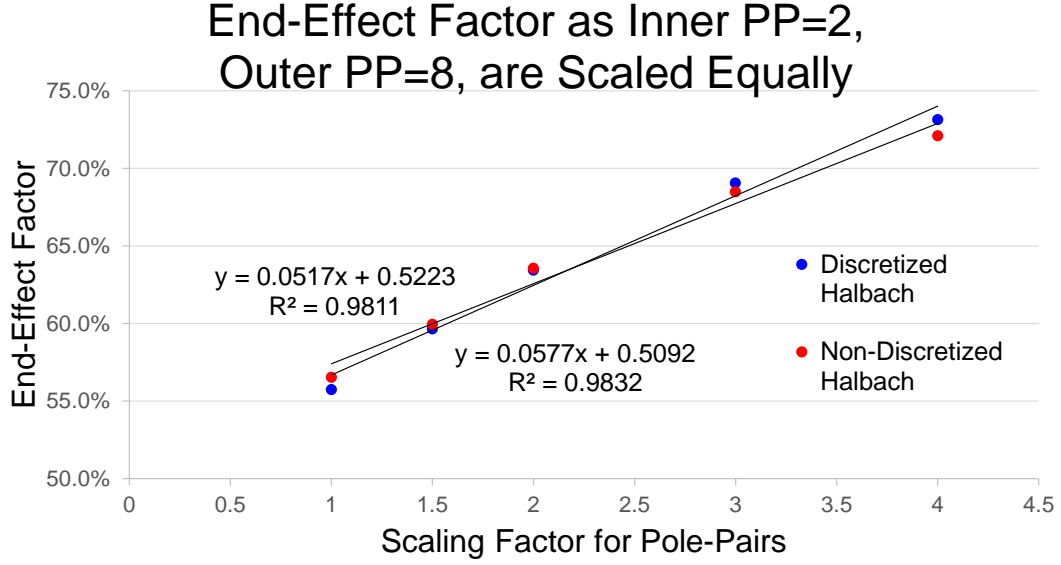


Figure 3.26: End-effect factor results for magnetic gears with discretized and non-discretized Halbach arrays as pole-pair scaling factor was varied.

Due to the results found in 3.26, it has been concluded that the pole-pair scaling factor is a significant contributor to the end-effect factor. The scaling factor was swept from 1 to 4 which correlates to 2 inner rotor pole-pairs and 8 outer rotor pole-pairs at 1, and 8 inner-rotor pole-pairs and 32 outer rotor pole-pairs at 4. This span caused an end-effect factor variation of 15.6%.

### 3.3 Reduced Length Modeling Application

This section applies the reduced length modeling theory to the original PT-1 model and then an axially longer variation of PT-1. The purpose of the exercise is to quantify the time savings and error associated with the reduced length modeling technique. The time saving analysis is done for two different gear designs to illustrate how results from the method vary depending on the end-effect factor.

### 3.3.1 PT-1 Time Savings and Error

The reduced length modeling technique has been applied to the original PT-1 geometry. This was done by modeling the geometry in 3D at various axial lengths and then supplementing the deviation from the base model with 2D model results. The combination of 2D and 3D models is described by,

$$l_{base} = l_{2D} + l_{3D} \quad (3.12)$$

and

$$T_{tot}(l_{2D}, l_{3D}) = T_{2D}(l_{2D}) + T_{3D}(l_{3D}) \quad (3.13)$$

where  $l_{base}$  is the axial length of the original 3D model (1.0" (25.4 mm) in this case),  $l_{2D}$  is the axial length modeled in 2D,  $l_{3D}$  is the axial length modeled in 3D,  $T_{tot}$  is the total torque,  $T_{2D}$  is the torque contribution from the 2D model, and  $T_{3D}$  is the torque contribution from the 3D model.

Figure 3.27 shows how the torque results combine from the 2D and 3D models to create a total torque estimate of the true torque. Notice that 3D axial length is plotted on the x-axis, so the 2D torque contribution decreases as more axial length is plotted in 3D. The total torque converges on the true torque as the axial length modeled in 3D approaches the base axial length.

The trade-off between 2D and 3D torque creates a trade-off between model accuracy and computation time. This phenomenon is shown in Figure 3.28 where modeling error increases as the computation time decreases. The percent error shown is described by,

$$E_{per} = \frac{T_{tot} - T_{true}}{T_{true}} * 100 \quad (3.14)$$



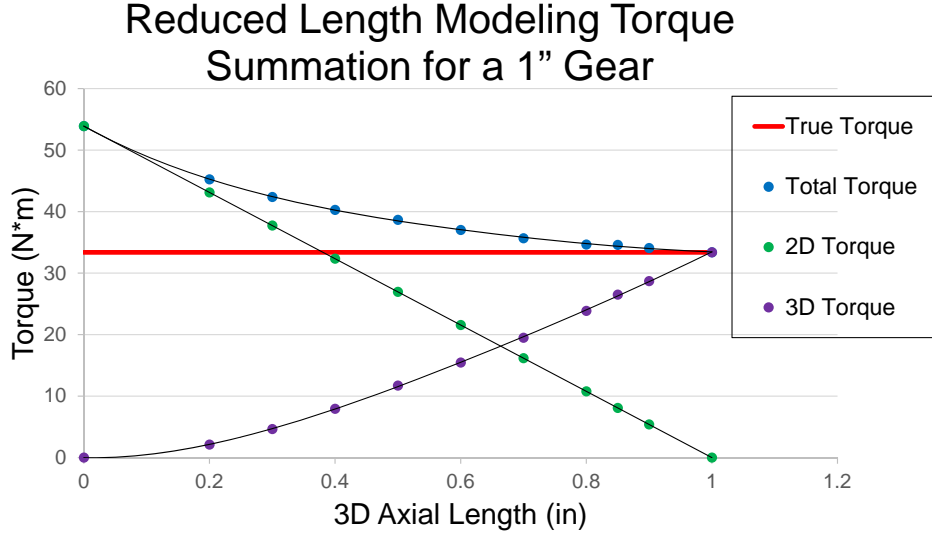


Figure 3.27: Illustration of the torque summation used for the reduced length scaling method. The plot is for a gear with a base axial length of 1.0" (25.4 mm).

where  $E_{per}$  is the percent error between total torque and true torque and  $T_{true}$  is torque when the full magnetic gear length is modeled in 3D. Taking 5% error as an acceptable threshold, the plot shows that only 0.8" (20.3 mm) of the full 1.0" (25.4 mm) needs to be modeled in 3D. This corresponds to a 42 minute reduction in computation time, a 49% reduction from the original time.

### 3.3.2 Modified PT-1 Time Savings and Error

The same analysis is repeated except the base axial length of the PT-1 design has been increased to 2.0" (50.8 mm). The end-effect factor of this gear is 76% as compared to the 62% end-effect factor of the original PT-1. Figure 3.29 shows the torque summation results when applied to a gear with relatively less end-effects. The

### Percent Error and Computation Time of 1" Base Axial Length Model

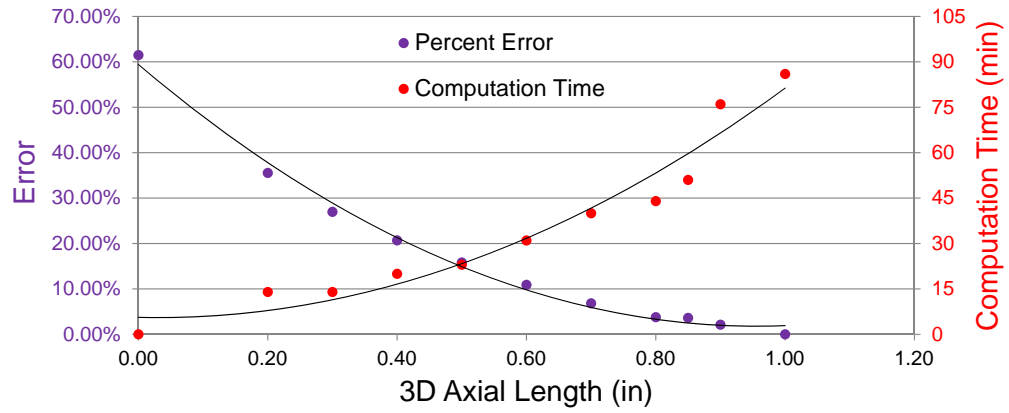


Figure 3.28: Scaling of percent error and computation time as reduced 3D model length is varied for a magnetic gear that had an original axial length of 1.0" (25.4 mm).

main feature is that total torque approaches true torque well before the full length of the gear is modeled in 3D.

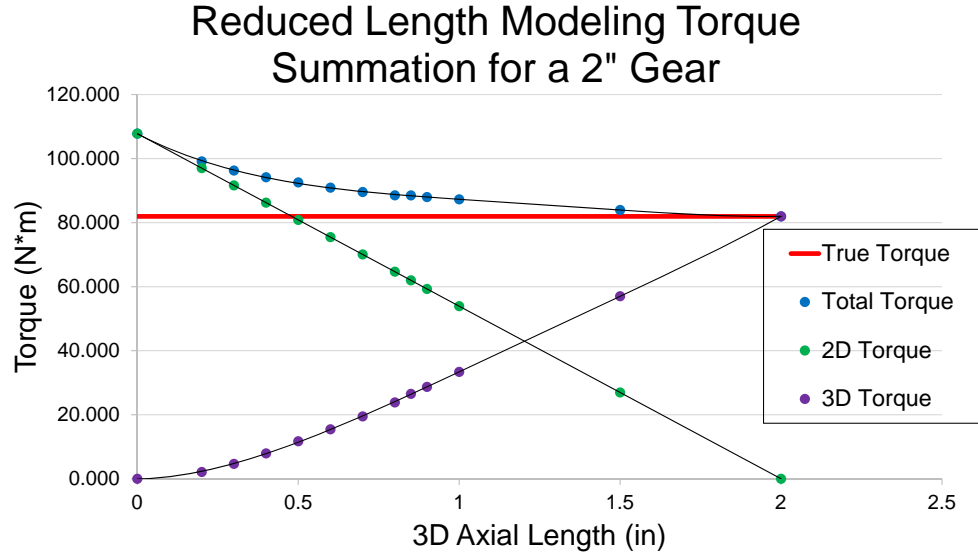


Figure 3.29: Illustration of the torque summation used for the reduced length scaling method. The plot is for a gear with a base axial length of 2.0" (50.8 mm).

The faster approach to true torque is also reflected in Figure 3.30 which shows the percent error and computation time statistics for the 2.0" (50.8 mm) base axial length model. Percent error in the plot is also calculated by (3.14). If the same acceptable percent error of 5% is chosen for this analysis, then only 1.2" (30.5 mm) of the full 2.0" (50.8 mm) must be modeled in 3D to meet the accuracy requirement. This corresponds to a 136 minute reduction in computation time, a 56% reduction from the original time. It is shown that the reduced length modeling method provides greater improvement to magnetic gear models with high end-effect factors.

## Percent Error and Computation Time of 2" Base Axial Length Model

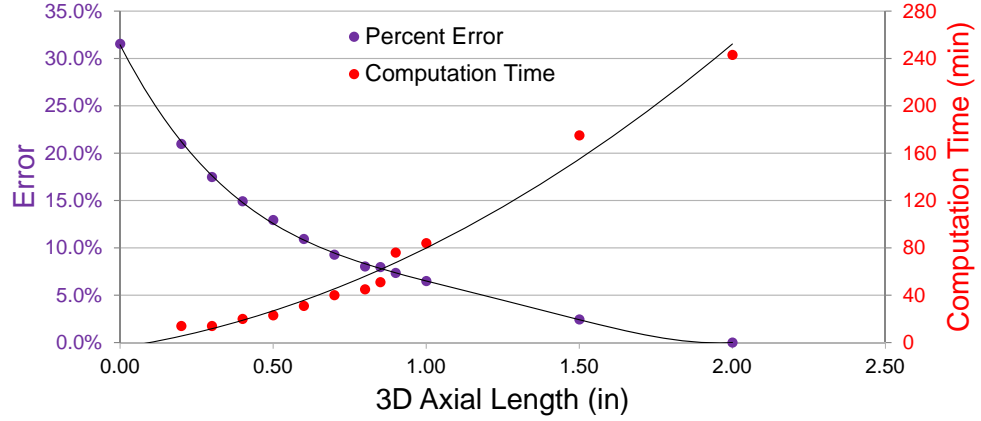


Figure 3.30: Scaling of percent error and computation time as reduced 3D model length is varied for a magnetic gear that had an original axial length of 2.0" (50.8 mm).

### 3.4 Discussion

#### 3.4.1 Summary of Results

It has been concluded that the reduced length modeling technique can be applied to a concentric magnetic gear topology that uses Halbach arrays with no back iron to significantly reduce model size while accruing minimal error. Computation time savings of 49% and 56% were shown for magnetic gear models that only had a 5% percent error from the original full 3D results. The end-effect factor was quantified with respect to several magnetic gear design variables to build a base of end-effect behavioral understanding such that the reduced length modeling technique can be applied in relative terms to other magnetic gears of a similar design. It was found

that axial length, outer radius, and pole-pair scaling factor all have a significant contribution to the end-effect factor. Large axial length corresponds to a high end-effect factor due to the large linear region of flux density. Small outer radius and large pole-pair scaling factor correspond to a high end-effect factor due to the increased in-plane leakage. Magnetic air gap thickness was not found to have a relatively large impact on the end-effect factor as compared to the other variables. Plots for these relationships can be found at the end of each variable's respective section.

### **3.4.2 General Application of Findings**

As previously mentioned, this thesis only provides the framework to apply the reduced length modeling method in relative terms to other models, not in absolute terms. Application of the method is most useful when performing modeling tasks that require repeated solution of subtly differing models, as would be the case in many parametric sweeps. When repeating many simulations, the time savings shown for this method can compound to become quite significant. An exploratory study could be performed to quantify torque convergence of the reduced length modeling method as various axial lengths are modeled in 3D. The convergence could then be used with an acceptable percent error tolerance to make computational savings that would apply to all trials of the parametric sweep. Caution should be taken to make sure that none of the parametric sweep parameters include relatively large variation of design variables that have been identified in this thesis as strongly correlated to the end-effect factor. A significant decrease in the end-effect factor could increase percent error beyond the defined tolerance.

The reduced length modeling method can also be useful when applied to magnetic gear models that would otherwise exceed available computer memory resources. The gear could be modeled in 3D at an axial length that can be managed by the computational resources. A convergence study could then be conducted using even shorter 3D models to determine how near the reduced length modeling results are to convergence on true torque. A convergence study may be unnecessary if a high end-effect factor can be extrapolated from a similar gear design by using end-effect factor scaling results presented in this thesis.

## Chapter 4: Cladding Magnet-Coaxial Magnetic Gear Design

This chapter includes:

- An explanation of cladding magnet improvement theory
- An optimization of cladding magnet design variables
- The specific torque increase when applying cladding magnets to the NASA PT-1 and PT-5 CMGs
- Recommendations for how to generally apply cladding magnets to CMG designs

### 4.1 Cladding Magnet Theory

It has been established that end-effect loss plays a significant role in the behavior and performance of magnetic gears, often causing sizable decreases in output torque. This section introduces a cladding magnet concept for the purpose of mitigating these end-effect losses and increasing specific torque. Generally speaking, magnetic cladding involves tailoring the magnetization vector of a permanent magnet such that it opposes unwanted leakage. Opposing leakage is relevant to magnetic gears because unwanted leakage over the axial end of the gear can reduce output torque by anywhere from 10% to 40% depending on the design. Opposition to the axial leakage would require permanent magnets on the axial ends of the gear that have a remanent flux

density vector in the axial direction. Cladding magnet flux redirection is shown in Figure 4.1.

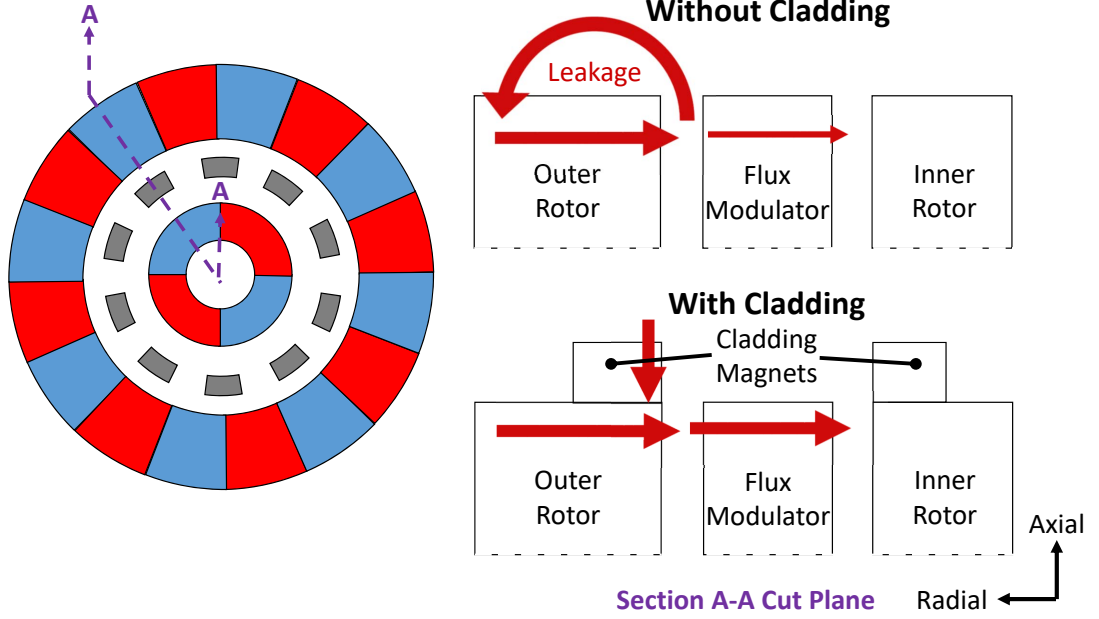


Figure 4.1: Representation of the cladding magnet capping effect. The red lines show the flux path from the outer rotor magnet.

Magnetic cladding has been proposed for application to a Halbach cylinder as early as 1987 [24]. It was suggested that weight could be saved by employing axially oriented cladding magnets to an octagonal dipole structure which very much resembles a Halbach cylinder. The dipole structure subject of this study was much smaller (outer radius = 17 mm) than the magnetic gears presented in this thesis; however, it was theorized that the weight saving results should scale well as size increases.

The Halbach cylinder cladding concept was then refined via parametric sweep in 2008 [6]. The sweep of cladding magnet geometry showed that all but Halbach



cylinders with a large axial length (200 mm) and a small outer radius (60 mm) can improve mean flux density within the bore with the addition of cladding magnets. Halbach cylinders of these characteristics are ill suited for cladding magnet integration because of end-effect factor scaling results shown in Subsections 3.2.1 and 3.2.3. Large axial length and small outer radius are both associated with a high end-effect factor. This means that end-effect losses are a relatively minor inefficiency in the magnetic system so devoting cladding magnet mass to mitigate them does not improve mean flux density enough to justify the added mass. Halbach cylinders that did not have these unfavorable characteristics showed a mean bore flux density improvement of up to 0.2-0.3 T for the same magnet volume.

These Halbach cylinder results could indicate potential specific torque improvements for magnetic gears because increased magnetic flux density is related to increased torque through (1.10) and (1.11), and because the magnet rotors are, in some respects, Halbach cylinders. However, the general application of cladding to Halbach cylinders does not explain how to best apply the concept to magnetic gears. The use of multiple pole-pairs per cylinder, the optimization of flux density at the flux modulator as opposed to the mean flux density of the bore, the inversion of the Halbach cylinder used for the inner rotor, and many other differences add complexity to the problem of magnetic gearing application. The following sections define cladding magnet geometry using several design variables, explore how to most effectively apply these design variables to magnetic gears, and finally, retrofit magnetic gear models with cladding magnets to show specific torque improvement. These coaxial magnetic gears retrofitted with cladding magnets are referred to as cladding magnet-coaxial magnetic gears (CM-CMGs).

## 4.2 Variable Sensitivity

This section serves to outline the cladding magnet design variables that have the most impact on output torque. The study is performed by analyzing cladding magnet modifications to the PT-1 magnetic gear outlined by Table 3.1. Figure 4.2 shows how these cladding magnets are incorporated onto the standard gear cross-section along with the definition of several design variables that are discussed in the following subsections. The cladding magnets are located on top of the standard radial magnets as close as possible to their respective air gaps. The cladding magnets are positioned there to minimize reluctance between them and the flux modulator. Only one side of cladding magnets is shown because the models utilize symmetry about the xy-plane, but in reality there are cladding magnets on both axial ends of the gear.

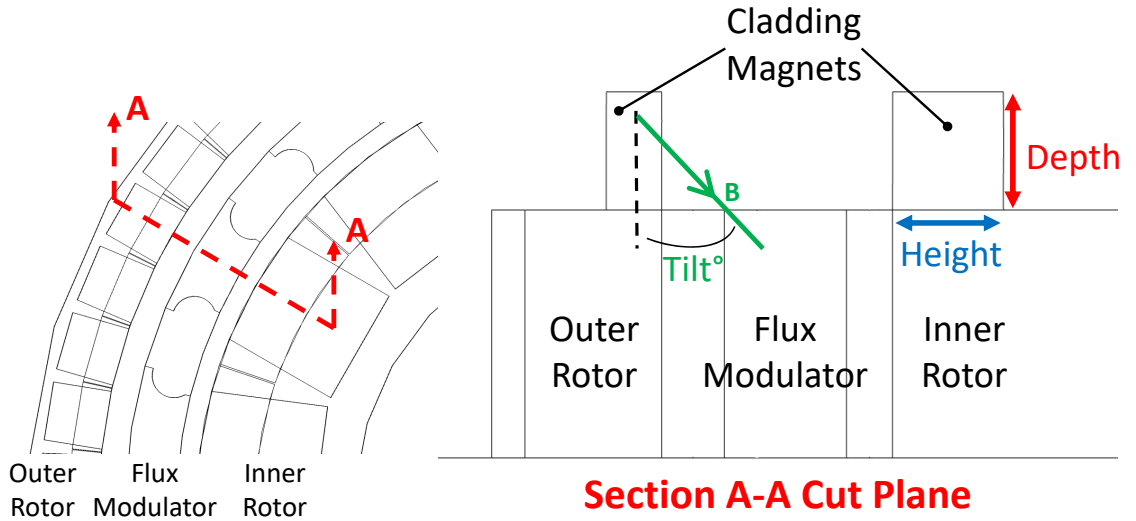


Figure 4.2: Radial cross-section of a CM-CMG. The three variables shown were the variables determined to be the most consequential to torque production.

The cladding magnets used in these trials are arranged as Halbach arrays to concentrate flux towards the axial center of the gear. The arrangement can be seen from a top view in Figure 4.3. It is noted that the orientation is modified when the tilt variable is introduced; however, this is the base vectoring when tilt=0°.

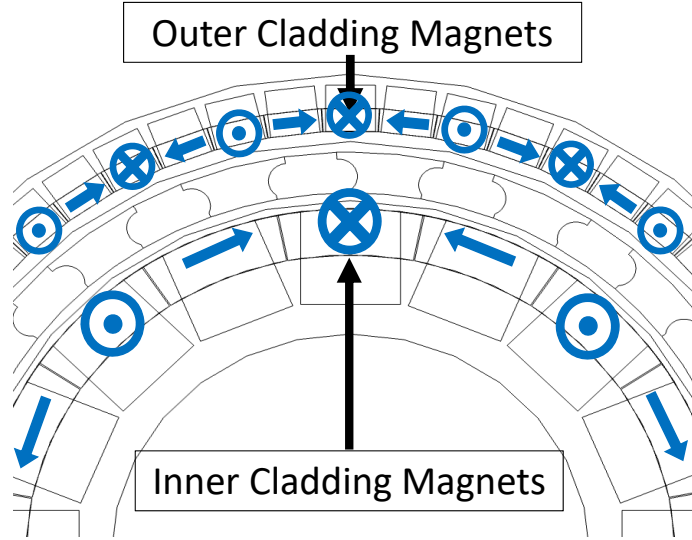


Figure 4.3: Top view of the Halbach array cladding magnet orientations.

Another feature of these models is that the axial length of the base PT-1 model is decreased as cladding magnet mass is added to keep total gear mass constant. The shortened (adjusted) axial length is shown by Figure 4.4. The properties of this modification are defined by,

$$W_{base} = W_{adj} + W_{CM} \quad (4.1)$$

where  $W_{base}$  is the base weight of PT-1,  $W_{adj}$  is the weight of the adjusted standard gear portion, and  $W_{CM}$  is the weight of the cladding weight, and,

$$l_{adj} = l_{base} - \frac{W_{CM}}{\lambda_{gear}} \quad (4.2)$$

where  $l_{adj}$  is the adjusted axial length of the standard gear portion,  $l_{base}$  is the base length of PT-1, and  $\lambda_{gear}$  is the mass per unit axial length of the PT-1 cross-section.

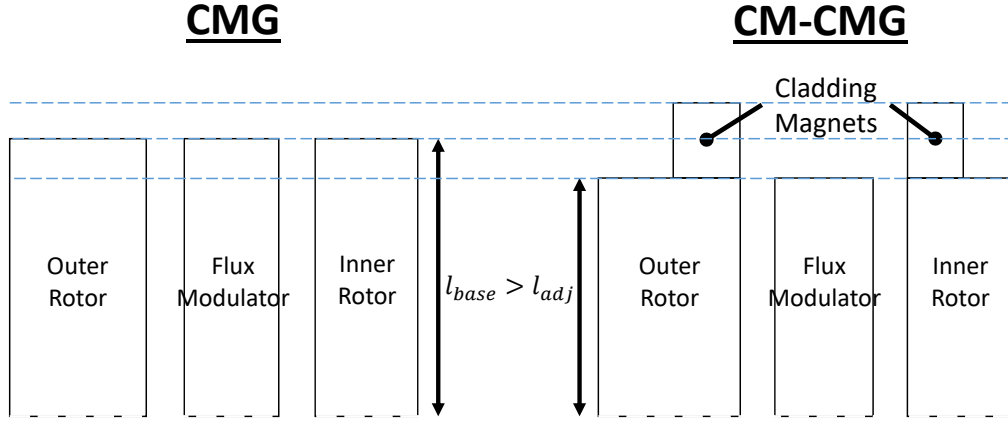


Figure 4.4: Illustration of the length adjustment made to the standard gear portion to make mass constant.

Mass must be kept constant for these trials because of the way specific torque scales with respect to magnetic gear mass. It has been shown in the literature that the specific torque of magnetic gears increases as the torque of the gear increases [26]. Torque is known to increase as mass increases (assuming magnetically active mass is increased). Specific torque increasing with respect to mass means that it would be inappropriate to compare the specific torque of more massive CM-CMGs to less massive CMGs because it would advantage the larger CM-CMGs. Without axial adjustment, the CM-CMG is always more massive than the corresponding CMG

because of the additional cladding magnet mass. It was decided axial length would be scaled down to keep mass the same because axial length can be scaled much easier than other design variables like outer radius.

#### 4.2.1 Height

The first design variable of discussion is cladding magnet height. Height is the radial length of the cladding magnet as shown in Figure 4.5. The inner and outer rotor radial magnets located underneath the cladding magnets have different thicknesses, so a variable has been introduced to scale the inner and outer cladding magnets to cover a set percentage of their respective radial magnets. This variable is known as height ratio  $H_{ratio}$  and is described by,

$$H_{ratio} = \frac{H_{in}}{t_{IR}} = \frac{H_{out}}{t_{OR}} \quad (4.3)$$

where  $H_{in}$  is the height of the inner cladding magnets,  $t_{IR}$  is the thickness of the inner rotor magnets,  $H_{out}$  is the height of the outer cladding magnets, and  $t_{OR}$  is the thickness of the outer rotor magnets.

A set of trials were run where height ratio and depth were varied for a cladding retrofit PT-1 magnetic gear of constant weight. The specific torque results of these trials are shown in Figure 4.6 because this thesis is concerned with optimizing specific torque, but it is noted that torque results would show the same trend because the weight of all trials in this study is constant. The trend of note with respect to height ratio is that for nearly all depths, the maximum specific torque appears at a height ratio of 50%. The trend is highlighted on the contour by a red line. The optimal value of 50% makes sense because imagining that the underlying radial magnet is divided radially into a north and south pole, a 50% height factor would be needed to

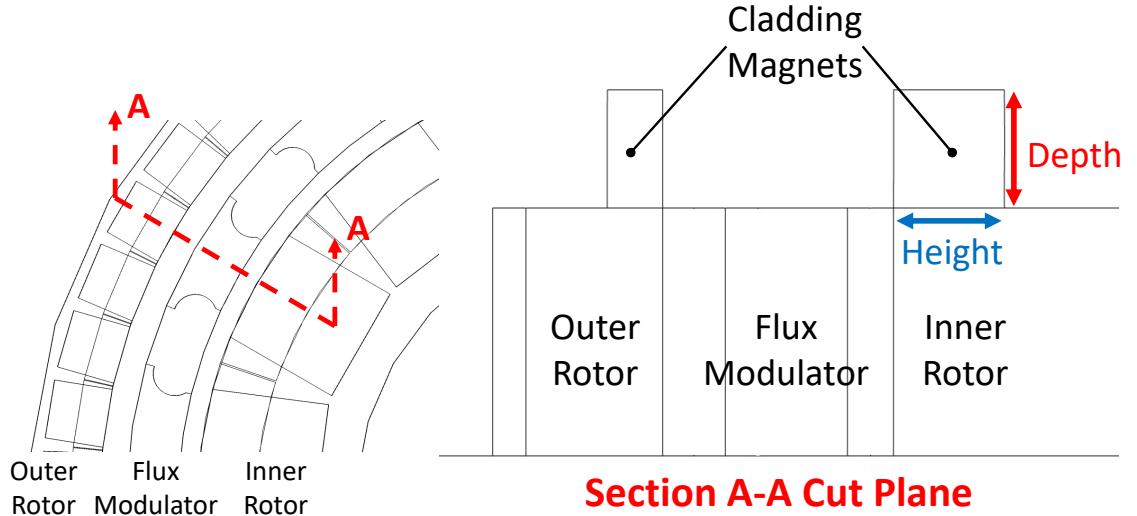


Figure 4.5: Radial cross-section with height and depth highlighted.

fully cover the north or south pole that is adjacent to the air gap. The trend does not hold indefinitely as depth increases, but it only breaks down once depth is reasonably beyond optimal (more than 25% greater than optimal depth).

#### 4.2.2 Depth

Mentioned in the previous subsection, depth is axial length of the cladding magnet as shown in Figure 4.5. Figure 4.6 shows that depth has an optimal value of  $\sim 0.2''$  (5.08 mm) for the PT-1 CM-CMG. The next depth study determines whether there is an advantage to decoupling depth of the inner and outer cladding magnets. Figure 4.7 shows the specific torque results of this study. Trials in this study were run using a height ratio of 50% and a tilt of  $\sim 45^\circ$ . The results show an increase of optimal specific torque from 32.9 N\*m/kg to 33.08 N\*m/kg by increasing the inner cladding magnet depth from 0.20" (5.08 mm) to 0.22" (5.59 mm). That is only a 0.547% increase of

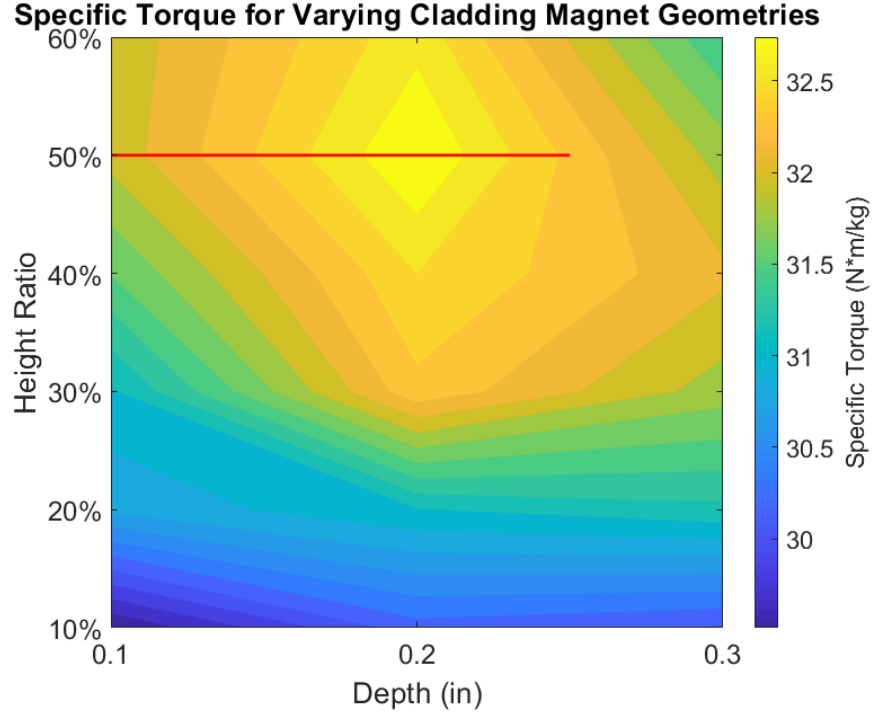


Figure 4.6: Specific torque as height ratio and depth are varied. The red line highlights the height ratio scaling trend. Maximum specific torque occurs at a height ratio of 50% and a depth of 0.2" (5.08 mm).

optimal specific torque, so it was concluded that decoupling inner and outer cladding magnet depth has an insignificant impact on specific torque.

To better understand the scaling of depth as CMG design variables change, a study was done to observe how the depth of optimal specific torque changes as the base axial length of PT-1 is varied. Axial length was chosen as the design variable of comparison because it also determines geometric length in the z-direction. Figure 4.8 shows the results of this study. It was found that depth of optimal specific torque slightly increases as base axial length of the CMG increases. It was also confirmed that specific torque increases as the base axial length is increased and the gear becomes

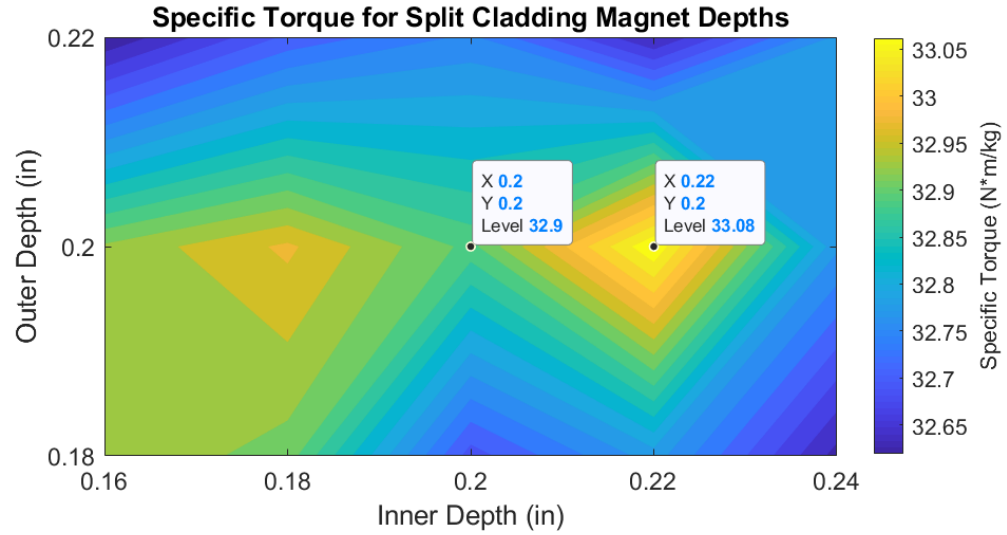


Figure 4.7: Specific torque as inner and outer cladding magnet depths are varied. Torque would show the same trend because mass is constant. Maximum specific torque occurs at an inner depth of 0.22" (5.59 mm) and an outer depth of 0.2" (5.08 mm).

more massive. This finding confirms the need to run all directly compared models at the same mass. More work will need to be done to determine how to universally apply depth, but for now, understanding of the correlation can help estimate a range of depths to include in a parametric sweep.



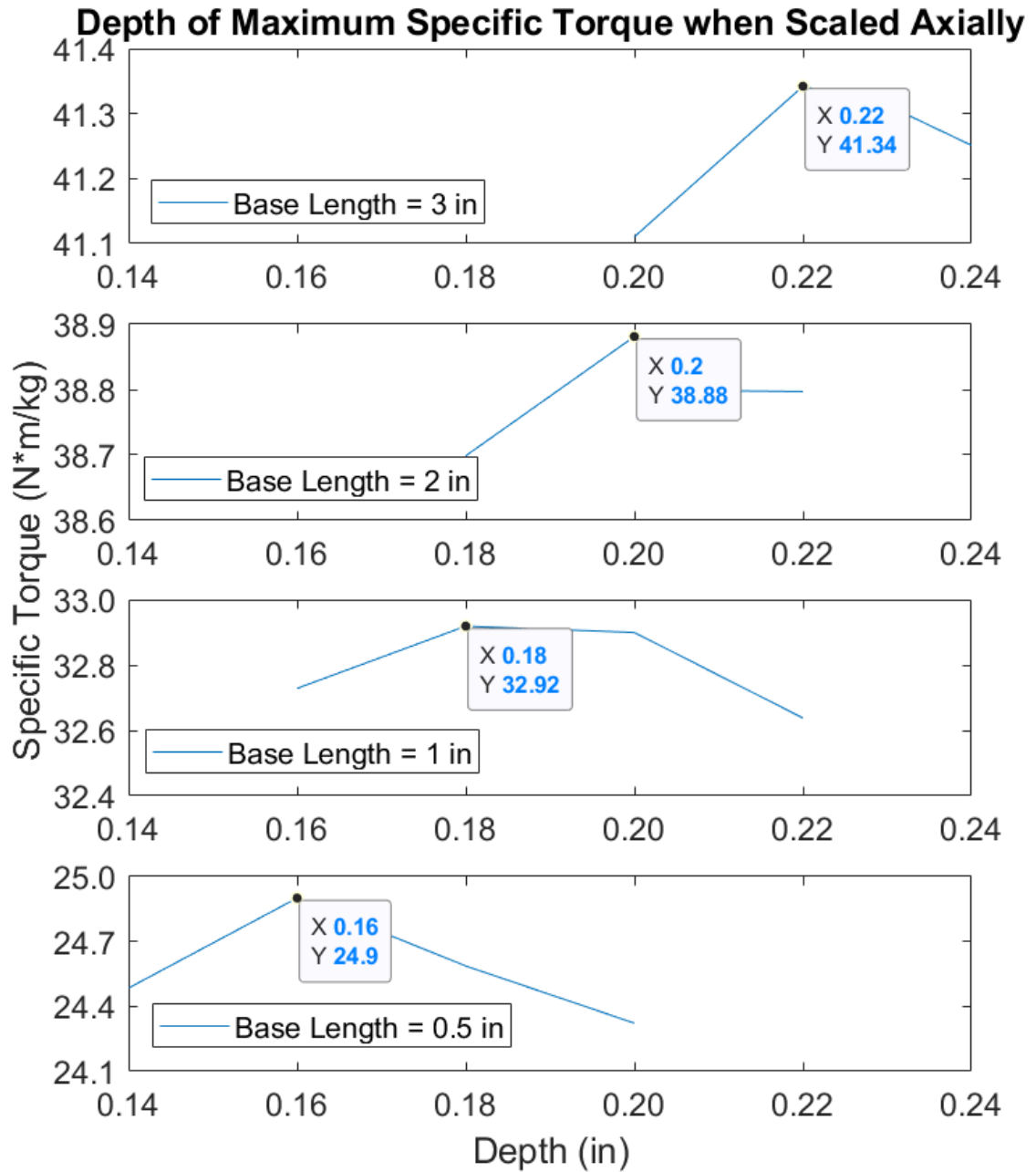


Figure 4.8: Specific torque results as depth is swept for magnetic gears of different base lengths. Base length is varies from 0.5" (12.7 mm) to 3.0" (76.2 mm) and optimal varies from 0.16" (4.06 mm) to 0.22" (5.59 mm).

### 4.2.3 Tilt

The final consequential design variable to be discussed is cladding magnet tilt. Tilt is rotation of the cladding magnet magnetization vector about the tangential axis. Rotation about the tangential axis is shown in Figure 4.9. Note that tilt between each rotor is mirrored about the flux modulator such that when tilt is greater than  $0^\circ$  and less than  $90^\circ$ , both sets of cladding magnets are oriented towards the flux modulator. Tilt only needs to be applied to the cladding magnets with a non-zero radial or axial remanent flux density component because the purely tangential cladding magnets which makeup the Halbach array experience no change in vectoring when rotated around the tangential axis. The tilt is applied to these cladding magnets of non-zero radial or axial remanent flux density on the inner rotor by,

$$\vec{B}_{r,tilt} = \vec{B}_r \times \begin{bmatrix} \cos(\text{Tilt}) & 0 & \sin(\text{Tilt}) \\ 0 & 1 & 0 \\ -\sin(\text{Tilt}) & 0 & \cos(\text{Tilt}) \end{bmatrix} \quad (4.4)$$

and on the outer rotor by,

$$\vec{B}_{r,tilt} = \vec{B}_r \times \begin{bmatrix} \cos(-\text{Tilt}) & 0 & \sin(-\text{Tilt}) \\ 0 & 1 & 0 \\ -\sin(-\text{Tilt}) & 0 & \cos(-\text{Tilt}) \end{bmatrix} \quad (4.5)$$

where  $\vec{B}_{r,tilt}$  is the remanent flux density vector after tilt is applied,  $\vec{B}_r$  is the original remanent flux density vector, and Tilt is the tilt. All vectors are defined in cylindrical coordinates.

The addition of tilt can also be conceptualized along a continuum of Halbach structures with an increasing variation of magnetization vectors. The continuum begins with Halbach cylinders that only project flux radially and ends with Halbach spheres that use a gradient of magnetization vectors to maximize flux density at the center of a sphere [19]. Figure 4.10 provides a visual for the continuum by showing

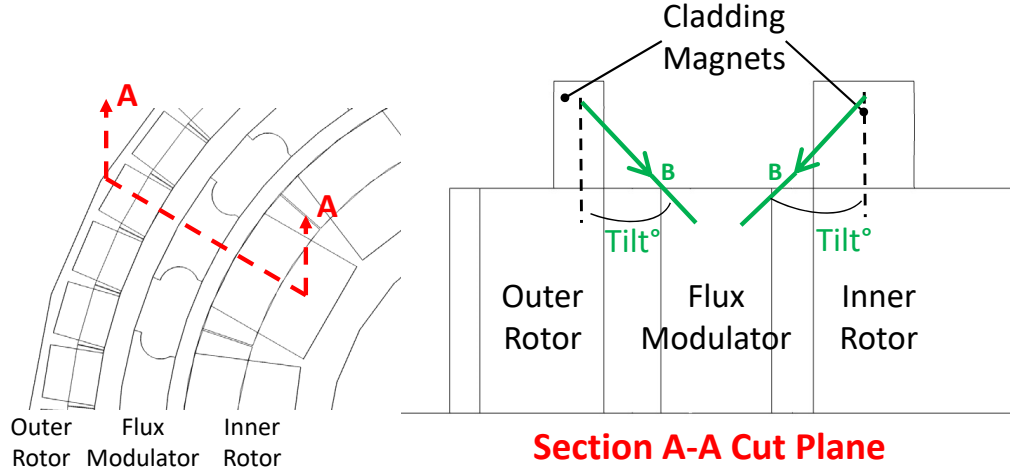


Figure 4.9: Radial cross-section with tilt highlighted.

radial cross-sections of the Halbach structures in question. Maximizing flux density at a central point is not ideal for magnetic gearing application, but it can be useful to consider the use of magnetization vector gradients to optimize flux density at a specific location.

A study was conducted to determine the sensitivity of output torque to tilt. The results of this study are shown in Figure 4.11. The plot shows that torque can be improved by 4.88% if tilt is set to  $45^\circ$  as opposed to completely axial at  $0^\circ$ . Another feature of tilt behavior shown by Figure 4.11 (b) is that torque is not particularly sensitive to tilt around  $45^\circ$ . From a tilt of  $40^\circ$  to  $50^\circ$ , torque only varies by  $0.03 \text{ N}\cdot\text{m}$ .

As with depth, a set of trials were run that decoupled tilt for cladding magnets on the inner and outer rotors. The results of these trials are shown in Table 4.1. It was found after sweeping  $\text{Tilt}_{in}$  that torque was similarly unaffected as with Figure 4.11

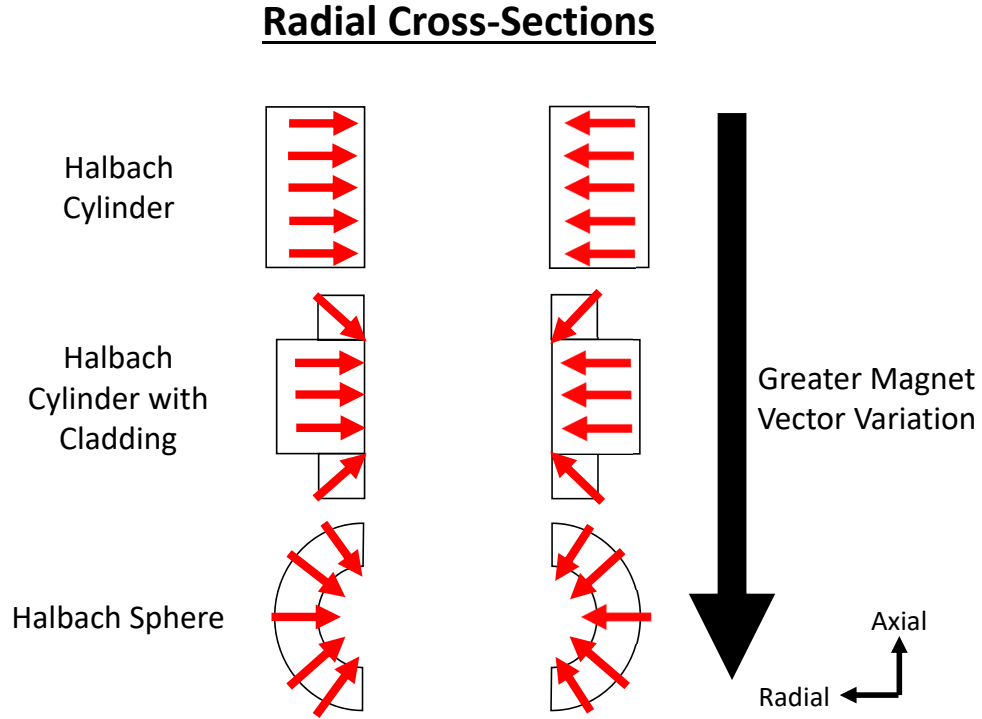


Figure 4.10: Progression of Halbach structures that incorporate increasing variation of magnetization vectors.

(b). At this point, the study was concluded because of the evidence that optimal tilt falls around  $45^\circ$ , and variation around this optimum makes little difference to torque.

Table 4.1: Torque results for the PT-1 CM-CMG when tilt of the inner and outer rotors are decoupled.

Trial	Tilt <sub>in</sub> (°)	Tilt <sub>out</sub> (°)	Output Torque (N*m)
1	42.5	47.5	37.3
2	45.0	47.5	37.3
3	47.5	47.5	37.3
4	50.0	47.5	37.3
5	52.5	47.5	37.3

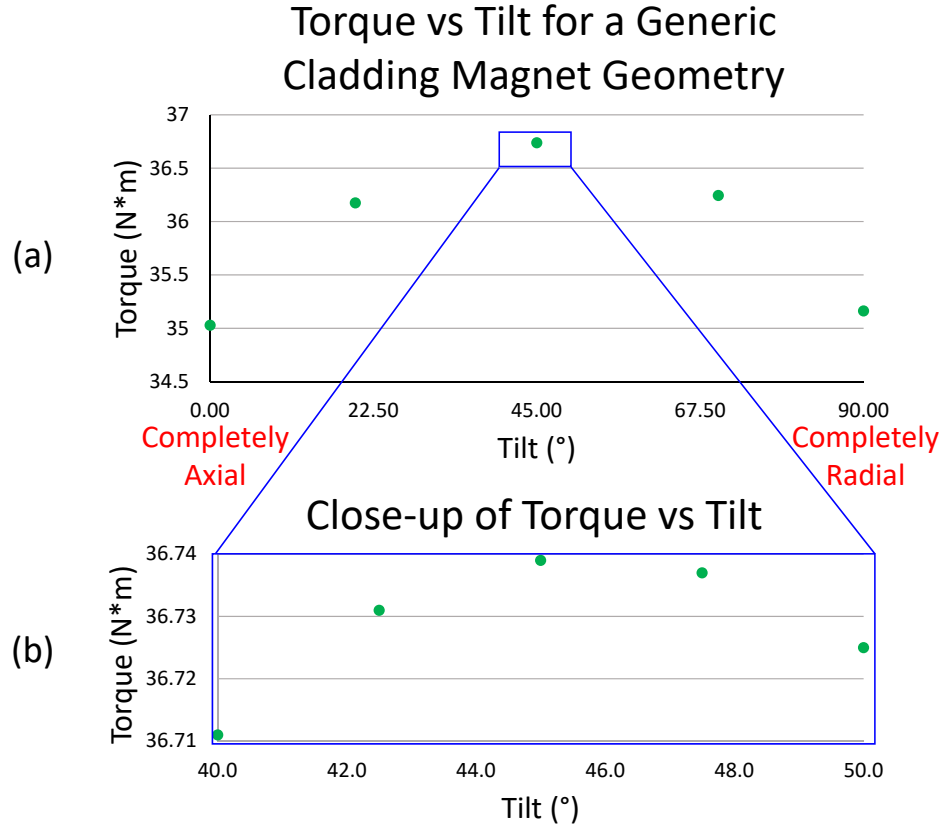


Figure 4.11: (a) Output torque of a CM-CMG as tilt is varied; (b) a close-up of “a” showing that there is very little difference in output torque around 45°.

#### 4.2.4 Miscellaneous Variables

Two final design variables were subject to preliminary investigation and deemed to have little effect on specific torque, but it is worth reporting that they were considered. The first of these variables has been labeled offset and is shown in Figure 4.12. Offset is the difference in axial length between the flux modulator and the magnet rotors. A very conservative model was run with an offset of 0.02” (0.508 mm). Axial lengths of the flux modulator and magnet rotors were adjusted to keep mass constant as

compared to a PT-1 CM-CMG model with no offset. The baseline model had a specific torque of 33.01 N\*m/kg while the offset model had a specific torque of 32.76 N\*m/kg. Decrease in specific torque for a relatively small offset led to the conclusion that consideration of offset would not provide a significant increase to specific torque.

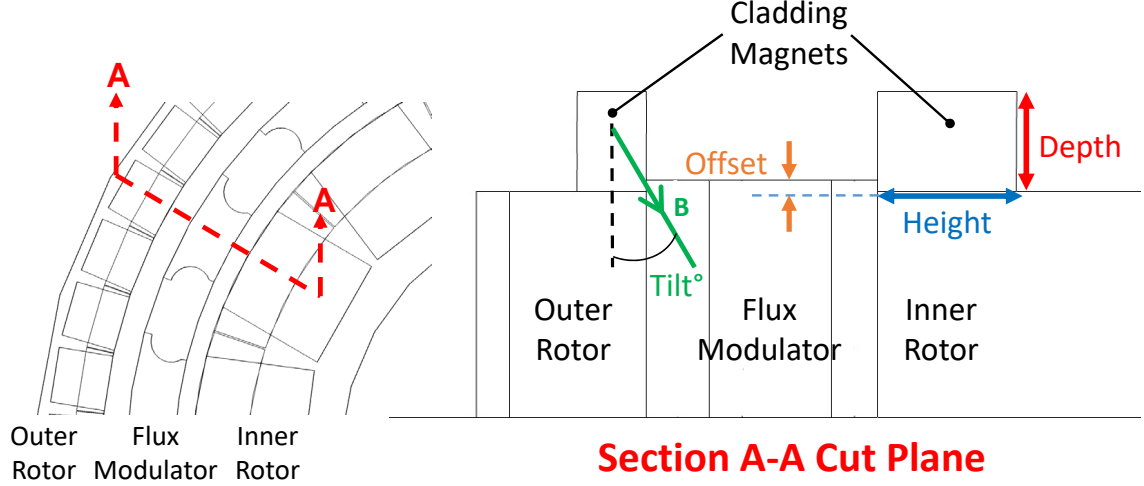


Figure 4.12: Radial cross-section to display offset.

The second design modification is the dividing of cladding magnets into an upper and lower cladding magnet with distinct magnetization vectors. The magnet vectors can be seen in Figure 4.13. Notice that  $Tilt_1 > Tilt_2$  to minimize reluctance between the flux modulator and each of the two cladding magnets. This vectoring is consistent with the theory presented with Figure 4.10. The torque results of the preliminary study can be found in Table 4.2. Trial 2 shows a mild improvement over the baseline, but again, there is not good evidence that dividing cladding magnets provides a significant increase to specific torque.

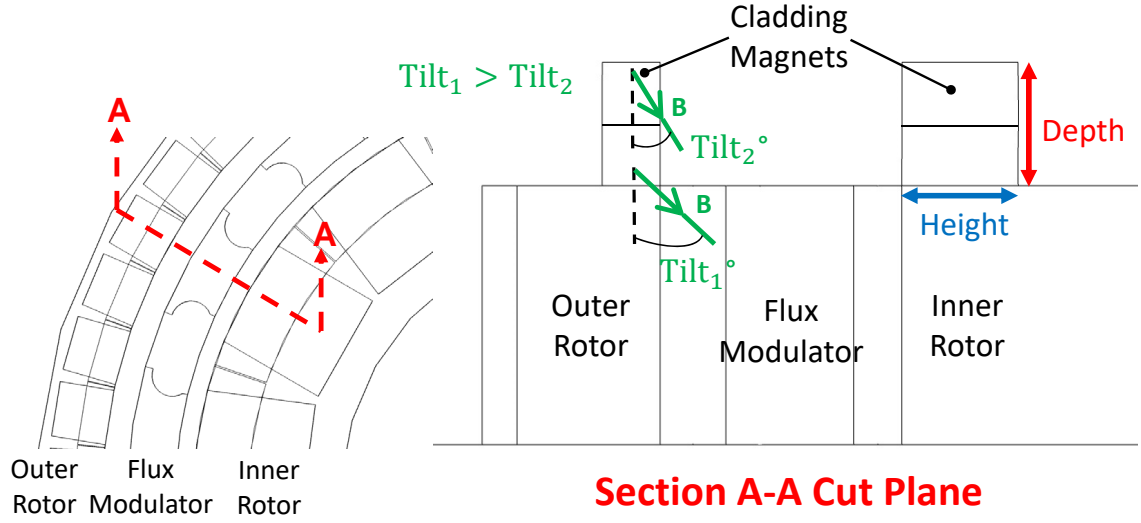


Figure 4.13: Radial cross-section to display  $Tilt_1$  and  $Tilt_2$ .

Table 4.2: Torque results for the PT-1 CM-CMG when cladding magnets are divided into an upper and lower magnet with distinct tilt angles.

Trial	$Tilt_1$ (°)	$Tilt_2$ (°)	Specific Torque (N*m/kg)
Baseline	45	45	33.0
1	60	30	33.0
2	50	40	33.1

### 4.3 Cladding Magnet Designs

The following section outlines distinct CM-CMG models that were optimized during the course of the variable sensitivity study along with a model that was created using principles derived from the variable sensitivity study. This serves to show the CM-CMG potential for specific torque improvement and a practical example of cladding magnet theory application. Each subsection includes a CM-CMG characteristic table that provides a list of characteristics specific to the CM-CMG. All other

magnetic gear properties come from the respective PT table. The PT-1 properties can be found in Table 3.1.

### 4.3.1 PT-1 Iteration 1

The first iteration of the PT-1 CM-CMG included several design features that were eventually replaced in the final design due to poor performance. The most obvious of these features is the use of non-Halbach array cladding magnets. These non-Halbach cladding magnets can be seen in Figure 4.14. Each of these cladding magnets is centered on a radially magnetized magnet underneath. The cladding magnets do not utilize a tilt angle.

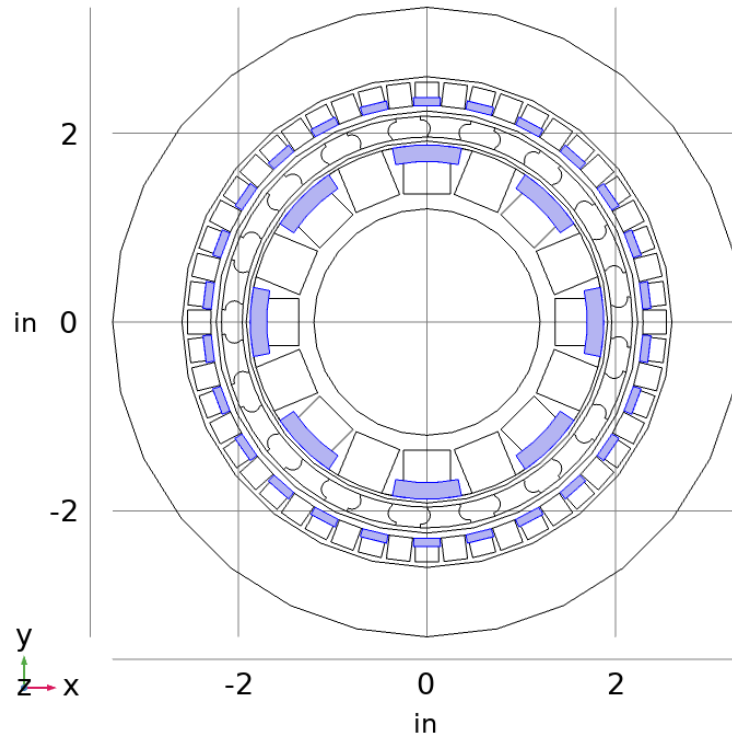


Figure 4.14: Top view of the PT-1 iteration 1 CM-CMG. The cladding magnets are highlighted in blue.



When Halbach arrays are used for the cladding magnets, the span angle of each cladding magnet is defined by the span angle of the standard gear magnet underneath. Without this definition, a variable had to be used to determine the span angle of each cladding magnet. The variable was labeled span angle ratio  $\phi_{ratio}$  and behaved according to,

$$\phi_{ratio} = \frac{\phi_{CM,in}}{\phi_{P,in}} = \frac{\phi_{CM,out}}{\phi_{P,out}} \quad (4.6)$$

where  $\phi_{CM,in}$  is the span angle of a single inner rotor cladding magnet,  $\phi_{P,in}$  is the span angle of a single inner rotor pole,  $\phi_{CM,out}$  is the span angle of a single outer rotor cladding magnet, and  $\phi_{P,out}$  is the span angle of a single outer rotor pole. Figure 4.14 shows a span angle ratio of 50% where each cladding magnet covers half of each standard gear pole. Keep in mind that each standard gear rotor uses 4 magnet per pole-pair Halbach arrays.

The addition of non-Halbach cladding magnets provided some specific torque improvement over the standard PT-1 design (1.37%), but the improvement was not significant. These results can be found in Table 4.3. The values chosen for span angle ratio, height ratio, and depth were found by performing a parametric sweep of these three variables.

Several conclusions were drawn from the Iteration 1 design, primarily that non-Halbach array cladding magnets only provide a minimal reduction to flux leakage. The use of non-Halbach arrays also hurt computational efficiency of the COMSOL models because it required the inclusion of span angle ratio to the parametric sweep. It is likely, based on the variable sensitivity study of tilt, that the absence of tilt significantly reduced the specific torque improvement of this CM-CMG design.

Table 4.3: Design and performance characteristics for the PT-1 Iteration 1 CM-CMG.

Characteristic	Metric	English
Span Angle Ratio	50%	
Height Ratio	35%	
Depth	6.99 mm	0.275 in
Adjusted Axial Length	23.0 mm	0.904 in
Weight	1.135 kg	2.502 lbm
3D COMSOL Torque	33.8 N*m	24.6 ft*lbf
3D COMSOL Specific Torque	29.7 N*m/kg	9.83 ft*lbf/lbm
Specific Torque Improvement over PT-1	1.37%	

### 4.3.2 PT-1 Iteration 2

The second and final CM-CMG for PT-1 is presented in this subsection. The Iteration 2 design was created by using the results of the variable sensitivity study performed in Section 4.2. The cladding magnet design variables considered for optimization include height ratio, depth, and tilt, and the model uses fully connected Halbach array cladding magnets as shown in Figure 4.15.

The addition of Halbach array cladding magnets and tilt generated a significant increase in specific torque as shown by Table 4.4. From Iteration 1 to Iteration 2, specific torque improved from 29.7 N\*m/kg to 32.9 N\*m/kg which corresponds to a 12.4% increase in specific torque over the original PT-1 magnetic gear. A fine parametric sweep found optimal depth and tilt to be 0.180" (4.57 mm) and 49° respectively. The sweep was informed by results outlined in Section 4.2 and made only a minor improvement to specific torque (<0.1 N\*m/kg). This CM-CMG design shows that the addition of cladding magnets to CMGs has the potential to generate significant specific torque improvement.

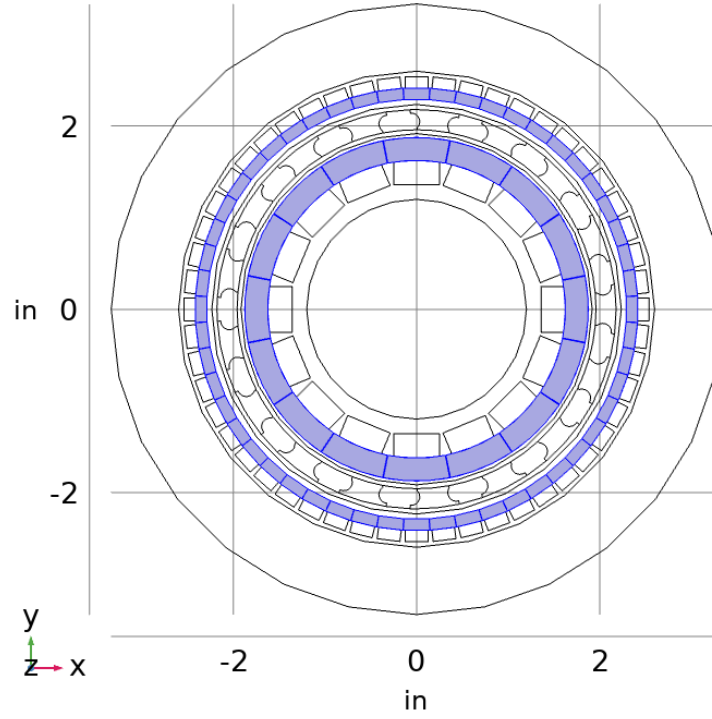


Figure 4.15: Top view of the PT-1 iteration 2 CM-CMG. The cladding magnets are highlighted in blue.

Table 4.4: Design and performance characteristics for the PT-1 Iteration 2 CM-CMG.

Characteristic	Metric	English
Height Ratio	50%	
Depth	4.57 mm	0.180 in
Tilt	49°	
Adjusted Axial Length	20.9 mm	0.823 in
Weight	1.135 kg	2.502 lbm
3D COMSOL Torque	37.4 N*m	27.6 ft*lb
3D COMSOL Specific Torque	32.9 N*m/kg	11.0 ft*lb/lbm
Specific Torque Improvement over PT-1	12.4%	

### 4.3.3 PT-5

The final CM-CMG focuses on the application of CM-CMG design principles to a new NASA PT-5 design. Characteristics of the PT-5 design can be found in Table 4.5. It is noted that the end-effect factor of 65.9% is still relatively low, being only slightly higher than PT-1's end-effect factor of 62.8%. A low end-effect factor means that a relatively large amount of flux is being lost to end-effects, so the implementation of cladding magnets has the potential to redirect a relatively large amount of flux. This low end-effect factor is likely due to PT-5's short axial length which has been shown to correlate to low end-effect factors in Subsection 3.2.1. It should be noted that the listed weight of PT-5 is the weight of only magnetically active materials.

Table 4.5: Design and performance characteristics for the NASA PT-5.

Characteristic	Metric	English
Gear Ratio	4.2	
Inner Pole-Pairs	10	
Outer Pole-Pairs	32	
Modulator Pieces	42	
Magnets per Inner Pole-Pair	12	
Magnets per Outer Pole-Pair	6	
Outer Radius	73.0 mm	2.87 in
Outer Magnet Thickness	4.0 mm	0.157 in
Outer Air Gap Thickness	1.0 mm	0.0394 in
Modulator Thickness	2.0 mm	0.0787 in
Inner Air Gap Thickness	1.5 mm	0.0591 in
Inner Magnet Thickness	5.0 mm	0.197 in
Axial Length	15 mm	0.591 in
Weight	0.379 kg	0.834 lbm
3D COMSOL Specific Torque	73.8 N*m/kg	24.7 ft*lb/lbm
3D COMSOL Torque	27.9 N*m	20.6 ft*lb
2D COMSOL Torque	42.4 N*m	31.3 ft*lb
End-Effect Factor	65.9%	

A top view of the PT-5 cladding outfit is shown by Figure 4.16. To make the model more representative of a practical magnetic gear, the cladding magnets were sized such that they had the same tangential gap between them as the standard gear magnets. The gap slightly decreases magnitude of the flux density waveform, but it is needed to reinforce the magnets with structural material. It is possible in some circumstances that the gap could make the waveform more sinusoidal, but further analysis than what is provided in this thesis would be needed to reach that conclusion [29].

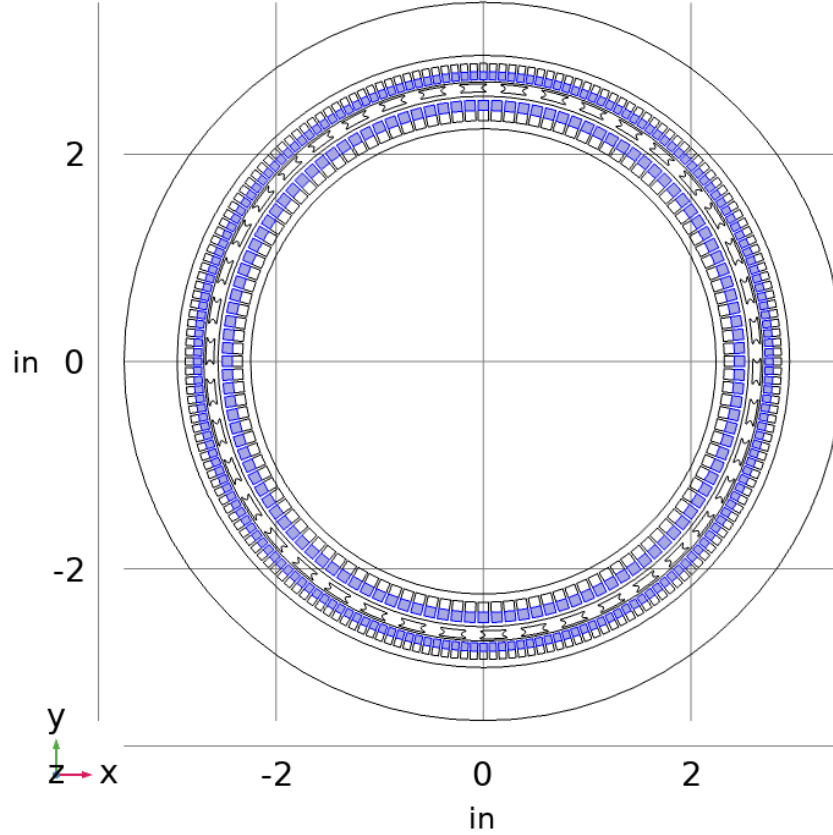


Figure 4.16: Top view of the PT-5 CM-CMG. The cladding magnets are highlighted in blue.

A series of trials were run to determine the optimal cladding magnet geometry for specific torque production. Height ratio and tilt are well understood design variables, so the focus of the trials was on determining optimal depth. Height ratio was set as 50% to completely cover the north or south pole adjacent to the air gap. Tilt was simulated at 45.0°, 47.5°, and 50.0° with very little effect on output torque ( $<0.01$  N\*m). Figure 4.17 shows the optimization trials that were run for depth. Depth for Trial 1 was chosen by applying a linear scaling to the optimal depth of PT-1 Iteration 2 based on the ratio of axial length between PT-1 and PT-5. The Trial 1 depth ended up being relatively close to the optimal value of 0.0925" (2.35 mm), but this study can only conclude that optimal depth scaling has some rough correlation to axial length.

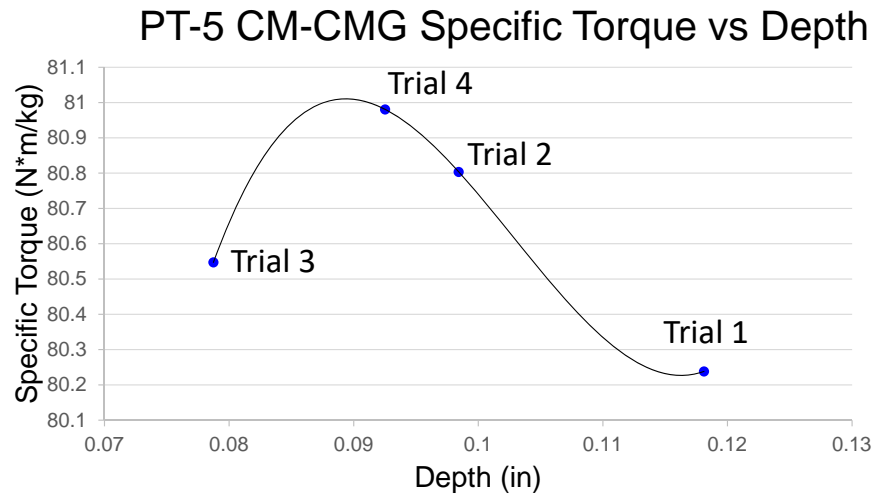


Figure 4.17: Depth trials performed for PT-5 CM-CMG that eventually converge on the depth of maximum specific torque. Optimal depth occurs around 0.09" (2.29 mm).

The combination of CM-CMG design variables shown in Table 4.6 ended up increasing specific torque by 9.76% as compared to the original PT-5. This is roughly

the specific torque improvement that would have been expected considering that PT-1 Iteration 2 increased specific torque by 12.4% for a gear with a slightly worse end-effect factor. The variable sensitivity study proved a useful guide for cladding magnet optimization as a roughly optimal cladding magnet geometry was achieved with less than 10 simulations.

Table 4.6: Design and performance characteristics for the PT-5 CM-CMG.

Characteristic	Metric	English
Height Ratio	50%	
Depth	2.35 mm	0.0925 in
Tilt	47.5°	
Adjusted Axial Length	13.0 mm	0.512 in
Weight	0.379 kg	0.834 lbm
3D COMSOL Torque	30.7 N*m	22.6 ft*lbf
3D COMSOL Specific Torque	81.0 N*m/kg	27.1 ft*lbf/lbm
Specific Torque Improvement over PT-5	9.76%	

## 4.4 Discussion

### 4.4.1 Summary of Results

It has been concluded that the application of Halbach cladding magnets to certain CMGs can improve specific torque. It was found that cladding magnet application to CMGs is directed by three main design variables. These variables include: height ratio, depth, and tilt. Height ratio was found be optimized at around 50%. Optimal depth was found to have a loose correlation to axial length of the magnetic gear. Optimal tilt was determined to be around 45°. Output torque was found to have very low sensitivity to tilt around this value.

Several CMGs were retrofitted with cladding magnets to show specific torque improvement. PT-1 Iteration 1 only shows a mild specific torque improvement of 1.37% and serves to illustrate the importance of Halbach arrays and tilt to the CM-CMG design. PT-1 Iteration 2 has a 12.4% specific torque improvement over the original PT-1 showing that cladding magnets can be used to significantly improve specific torque of CMGs. PT-5 CM-CMG has a specific torque improvement of 9.76% over the original PT-5. The variable sensitivity study provides accurate estimations for the optimal cladding magnet design variables.

#### **4.4.2 General Application of Findings**

As previously mentioned, cladding magnet retrofitting is particularly useful for CMG designs that suffer from extreme end-effect losses. Significant end-effect losses are commonly associated with magnetic gears that have large radii and small axial lengths. This style of CMG is appealing from a scaling perspective because output torque roughly scales as the outer radius squared, something that cannot be said for a design variable like axial length or pole-pair scaling factor. However, increasing outer radius is also shown to increase the significance of end-effects. These scaling trends makes small axial length, large outer radius, magnetic gears an appealing target for CM-CMG conversion. The trends shown in Section 4.2 can be used to reduce the size of the parametric sweeps necessary to optimize cladding magnet design variables.



## Chapter 5: Concluding Remarks

### 5.1 Conclusions

This thesis developed theory for a reduced length modeling method that can decrease the computation time of magnetic gear simulations. The end-effect factor was identified as a predictor of the severity of end-effect losses and design variables were swept to determine the significance of their correlation to the end-effect factor. It was found that the end-effect factor is very sensitive to axial length at relatively small lengths but eventually becomes less sensitive as additions to axial length beyond a certain point do little to change the significance of end-effect losses. Decreasing outer radius and increasing pole-pair scaling factor were found to be correlated with an increasing end-effect factor because the increase of in-plane flux leakage means that axial leakage is less significant. It is concluded that magnetic air gap thickness has a relatively weak correlation to the end-effect factor. These relationships were analyzed for the purpose of estimating the reduced 3D modeling length that would be necessary for reasonably accurate torque results.

The reduced length modeling method was then applied to the NASA PT-1 magnetic gear to demonstrate a reduction in computation time and to relate modeling

inaccuracy to the saved computation time. It was found that for the PT-1 and an axially lengthened version of PT-1, computation time is approximately cut in half while percent error for output torque remains  $<5\%$ . It was found that computation time savings are greater for the axially lengthened model that has a greater end-effect factor. This observation led to the conclusion that magnetic gears with a greater end-effect factor can be accurately modeled with less 3D length and therefore experience greater time savings. Improved time saving for high end-effect factor magnetic gears derives from their characteristic of relatively longer linear regions that can be accurately estimated with 2D COMSOL models.

This thesis developed theory for a cladding magnet-coaxial magnetic gear (CM-CMG) that produces greater torque than an equally massive CMG. A series of cladding magnet design parameters were analyzed for the purpose of understanding their impact on specific torque. A parametric sweep of height ratio and depth concluded that optimal height ratio is 50% for most reasonable depth values. Optimal depth was found to scale to some degree with axial length, while optimal tilt was determined to be approximately  $45^\circ$ . The design variables offset and Tilt<sub>2</sub> were found to have minimal impact on output torque.

Cladding magnet theory was then applied to two CMG designs to increase specific torque. The first iteration of a CM-CMG outfit of PT-1 showed minimal improvement to specific torque because the design lacked Halbach array cladding magnets and the tilt design variable. Once these features were added to the second iteration, specific torque showed a 12.4% increase over the original PT-1 design. The NASA PT-5 CMG was then modified with cladding magnets based on the optimal design parameters listed above. The resulting CM-CMG has a specific torque increase of 9.76% over

the original PT-5, and the entire cladding magnet optimization sweep took less than 10 simulations. The fast optimization process indicates that the developed cladding magnet theory works well to predict optimal design variables. It is noted that all CM-CMG designs had the same mass as their original CMGs.

## 5.2 Future Work

The two topics presented in this thesis are quite new to the field of magnetic gearing, so as a result, there is significant potential for further development. With respect to the reduced length modeling method, there is much work to be done in regards to the understanding of design variable impact on the end-effect factor. Further studies could be conducted to understand the correlation of design variables like gear ratio, flux modulator thickness, and magnet rotor thickness to the end-effect factor. There is also potential for a much more involved, multi-dimensional analysis that relates many design variables to the end-effect factor within a single equation. Accurate prediction of the end-effect factor could be used to define the length of a reduced length model that would likely have greater accuracy and show 3D flux behavior.

Another aspect of reduced length modeling that could use further research is the understanding of flux density profiles with respect to axial length. It could be useful to have a better understanding of these profiles because of how they determine the accuracy of 2D torque estimation. For example, it is known that these profiles have a nonlinear region where flux density decays away due to end effects; however, the exact start of the decay and its rate is not well understood. If flux decay is delayed but has a steep drop-off vs beginning early and decreasing slowly, this could have different implications for how well a 2D model can estimate torque contribution of

the linear region. Understanding the flux density profile shape could also provide the framework for generating a torque adjustment factor which accounts for the fact that the reduced length modeling method always overestimates torque due to the ideal nature of 2D modeling.

With respect to the CM-CMG design, more work could be done to understand the scaling of optimal cladding magnet depth. Furthering the research would likely involve a more rigorous parametric study of depth for multiple gear designs. The depth study in this thesis only varied axial length, but other design variables like rotor and air gap thickness could also have an impact on optimal depth.

The CM-CMG design process in this thesis revolved around retrofitting existing CMGs to improve specific torque, but it would be a useful contribution to the technology if a CM-CMG was designed without the constraints of an existing gear. The proposal is to design a CM-CMG from the ground up while tailoring the standard gear portion to interact optimally with the cladding magnets. The likely outcome of this approach would be a small axial length, large outer radius CM-CMG. Torque roughly scales as outer radius squared, so it is ideal to increase outer radius as opposed to axial length when not considering end-effect losses. End-effect losses would normally be significant for a gear of this design, but the addition of cladding magnets could greatly mitigate these losses.

The final suggestion for future work is to build a CM-CMG prototype. The modeling processes used in this thesis have been reliable in predicting magnetic gear performance, but a CM-CMG model has never been directly validated by an experimental prototype. It is also likely that there will be unique fabrication and assembly

issues (obtaining magnets with unusual magnetization vectors; stacking axially magnetized magnets) that will not be well understood until a prototype has been designed and built.

## Appendix A: Caged Flux Modulator

A caged modulator concept has been modeled for the purpose of quantifying torque and specific torque reduction that results purely from the modulator discretization process. In practice, the caging modification allows for air gap reductions that improve specific torque overall, but this analysis does not account for those air gap reductions due to a lack of magnetic gear models that account for mechanical behavior.

A reduction in air gap thickness can result in significant torque improvement for a magnetic gear by lowering radial reluctance and increasing flux density at the flux modulator. However, the lower limit of air gap thickness is constrained by the radial stiffness of the flux modulator. When the air gap thickness falls below the bottom threshold, the magnetic forces bow the flux modulator which causes it to come into physical contact with the inner rotor. The inner rotor is of greater concern than the outer rotor because the lower number of pole-pairs means that there is more flux density concentration at each pole which leads to greater attractive forces.

In order to stiffen the flux modulator and allow for smaller air gaps, a caged modulator modification is presented in which ribs have been added to a standard flux modulator structure. The caged modulator modification can be seen in Figure A.1. The geometry of the caged modulator is defined by the variables shown in Figure A.2. For the caged modulator trials, the axial length of magnetically active modulator

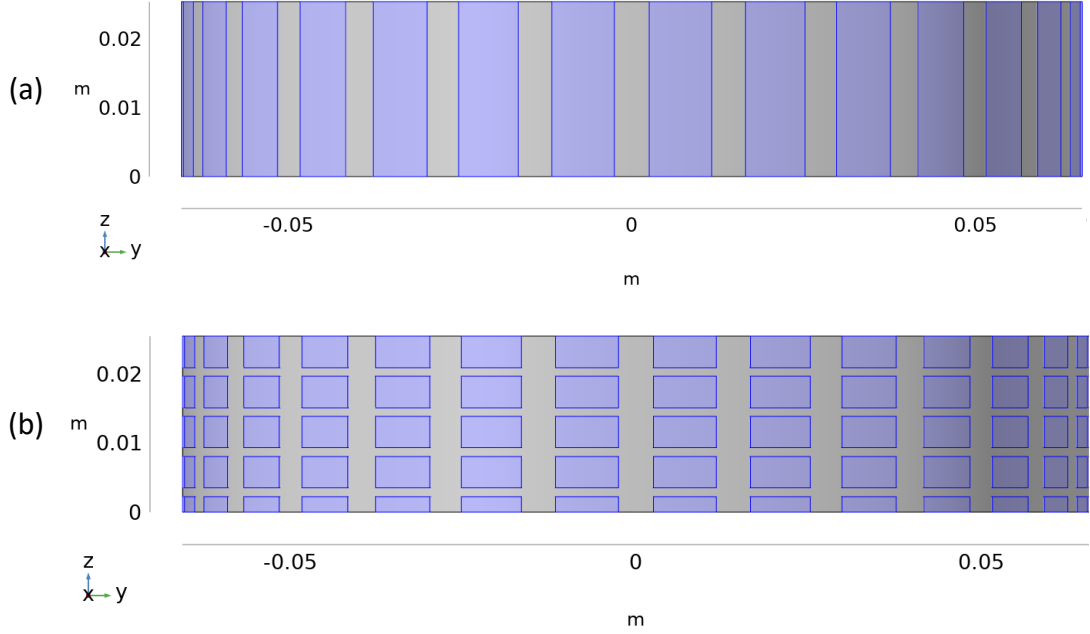


Figure A.1: (a) Front view of a standard flux modulator; (b) front view of a caged flux modulator. The modulator material is highlighted in blue while the structural material is colored gray. Only one axial half of the gear is shown.

material,  $L_{active}$ , has been normalized by,

$$L_{per} = \frac{L_{active}}{L} \quad (A.1)$$

where  $L_{per}$  is the percentage of total length comprised of magnetically active material and  $L$  is the total axial length of the magnetic gear.

A study was done to determine the impact of caged modulator geometry on specific torque. The study was performed using the NASA PT-3 as a baseline, and its results can be seen in Table A.1 [25]. It was found that all trials showed a lower torque and specific torque than the baseline PT-3 due to the lower volume of flux modulator material. A comparison of Trials 1-3 shows that increasing discretization  $\#$  is related to increasing torque and specific torque. It is noted that as discretization  $\#$  becomes

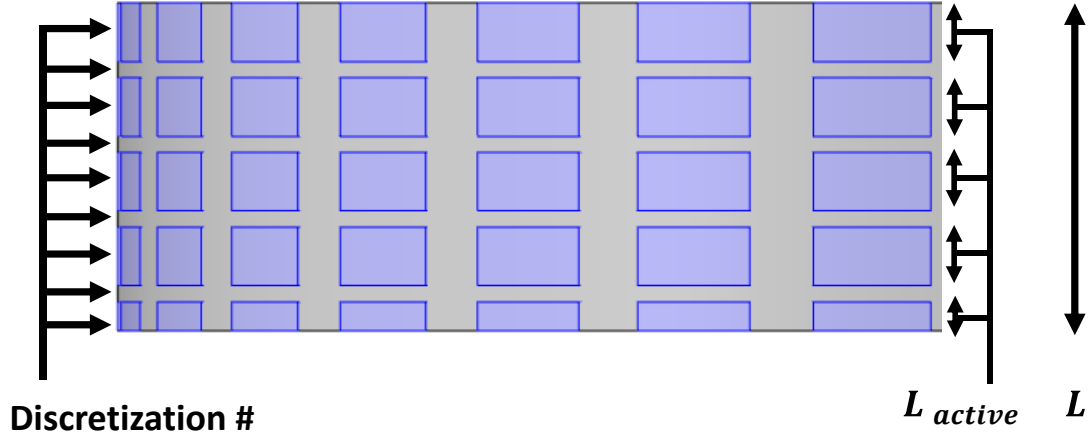


Figure A.2: Design variables that define the caged modulator geometry.

large, the increase in torque and specific torque is relatively less. A comparison of Trials 2, 4, and 5 shows that increasing active length percentage is related to increasing torque and specific torque. It is noted again that as active length percentage becomes large, the increase in torque and specific torque is relatively less.

Table A.1: Torque results for various caged modulator geometries as compared to the baseline PT-3.

Trial	Active Length Percentage	Discretization #	Weight (kg)	Torque (N*m)	Specific Torque (N*m/kg)
PT-3	100%	1	2.38	113	47.4
1	80.0%	19	2.34	107	45.7
2	80.0%	39	2.34	109	46.6
3	80.0%	59	2.34	110	47.0
4	85.0%	39	2.35	111	47.2
5	75.0%	39	2.33	106	45.5
<b>6</b>	<b>80.3%</b>	<b>17</b>	<b>2.34</b>	<b>107</b>	<b>45.7</b>



Trial 6 was performed with specific design variables such that the axial length of each modulator rib would be 1.25 mm (0.0492"). This length was chosen because it is the minimum length required to embed structural enhancing carbon fiber within the modulator ribs. These trials show that the flux modulator can be caged with a minimal reduction to specific torque (3.57% decrease for Trial 6). This decrease is expected to be significantly smaller than the specific torque increase that results from smaller magnetic air gaps.

## Appendix B: 1000 Gear Ratio Magnetic Gear

A 2D COMSOL study was done to determine the best design for a magnetic gear with a gear ratio of 1000 and an output torque of 50 N\*m. The magnetic gears in this study were constrained to CMGs that utilize Halbach array rotors with no back iron. The first design examined by this study is a single stage magnetic gear with 1 inner rotor pole-pair, 1000 modulator pieces, and 999 outer rotor pole-pairs. The four trials of this gear design are shown in Figure B.1.

The outer diameter was varied for these trials because two major constraints of this design are the width of the outer rotor magnets and the significant in-plane leakage that results from a large number of outer rotor pole-pairs. These constraints are both directly linked to the radius of the gear. Magnet width increases as outer radius increases, and in-plane leakage decreases as outer radius increases.

Design and performance characteristics are shown in Table B.1, and a sample mesh for Trial D is shown in Figure B.2. It is noted that a non-discretized Halbach ring is used for the magnet rotors, but that outer rotor magnet widths are provided based on 4 magnet per pole-pair Halbach arrays. The magnet width results indicate that this gear would be impractical to manufacture as neodymium magnets of a width less than 0.050" (1.27 mm) are very difficult, if not impossible, to purchase. The torque results also suggest impractical design features as the gear would have to be at least

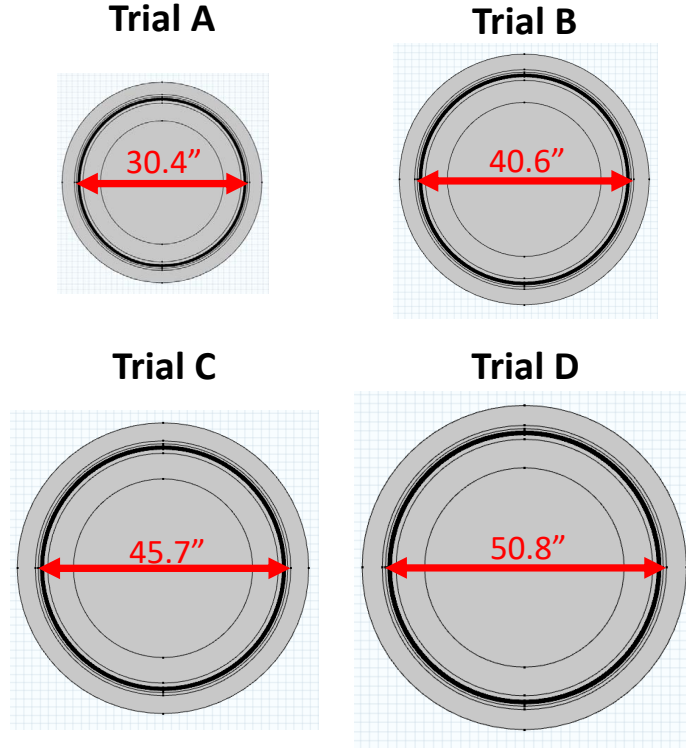


Figure B.1: Four COMSOL trials are run for a magnetic gear with a gear ratio of 1000. Each trial has a different outer diameter.

3.383' (1.031 m) in diameter to allow for a reasonable axial length. The length results reported in this appendix include a 167% increase to roughly account for the torque loss due to end-effects and discretized Halbach arrays. The magnet width and torque findings have led to the conclusion that a single stage gear is not an effective design to achieve a gear ratio of 1000 with an output torque of 50 N\*m.

Post-processing was performed to verify that in-plane leakage was a significant factor in the low torque production of Trial A. The radial and tangential flux densities were measured around the circumference of the magnetic gear at the inner air gap for each trial. If in-plane leakage is significant for Trial A, then it is expected that the

Table B.1: Torque and approximate length results for the 1000 gear ratio trials.

Trial	Outer Diameter (in)	Outer Rotor Magnet Width (in)	Pole Piece Width (in)	Torque per Unit Length (N*m/in)	Approximate Axial Length for 50 N*m Considering Losses (in)
A	30.4	0.023	0.046	0.26	315
B	40.6	0.032	0.062	5.32	31.3
C	45.7	0.036	0.070	11.7	14.3
D	50.8	0.040	0.078	22.0	7.58

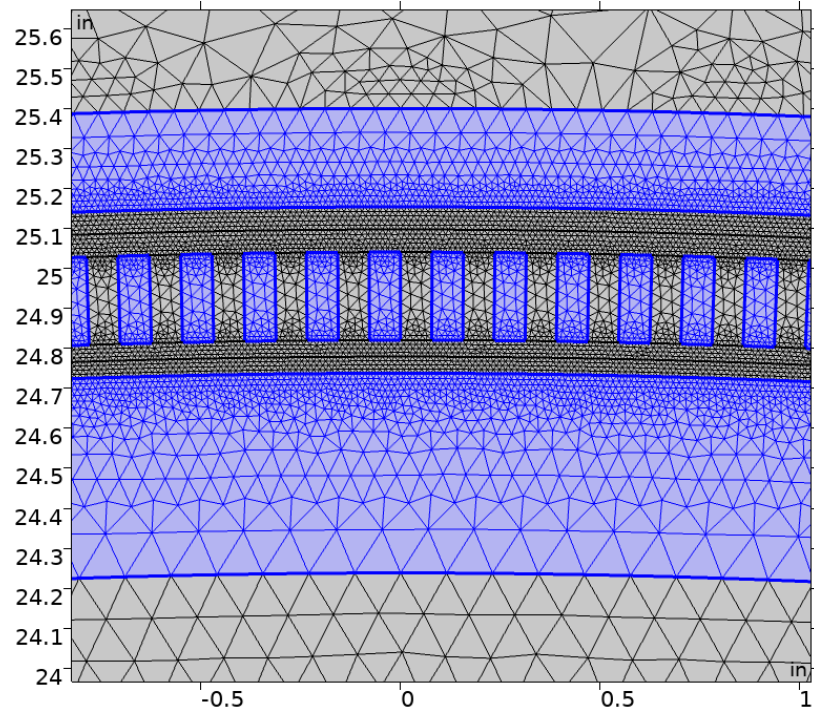


Figure B.2: A close-up on the mesh of Trial D. The magnetically active components are highlighted in blue.

flux density frequency component associated with the outer rotor will be smaller for Trial A than Trials B-D. Figure B.3 shows the source and measurement locations. It

is noted that the distance between the source and measurement locations is the same for all trials.

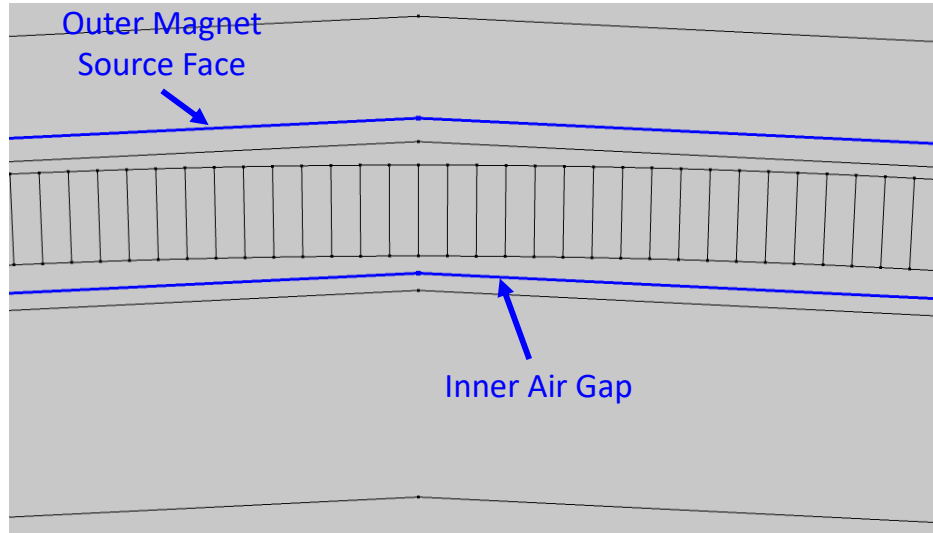


Figure B.3: Location of the flux density measurement and the source of interest.

Figures B.4-B.6 show the flux density waveform and fast Fourier transform (FFT) results for Trial A. It is noted that the high frequency harmonic resulting from the outer rotor magnets is relatively small. The waveform shape is dominated by the primary inner rotor harmonic.

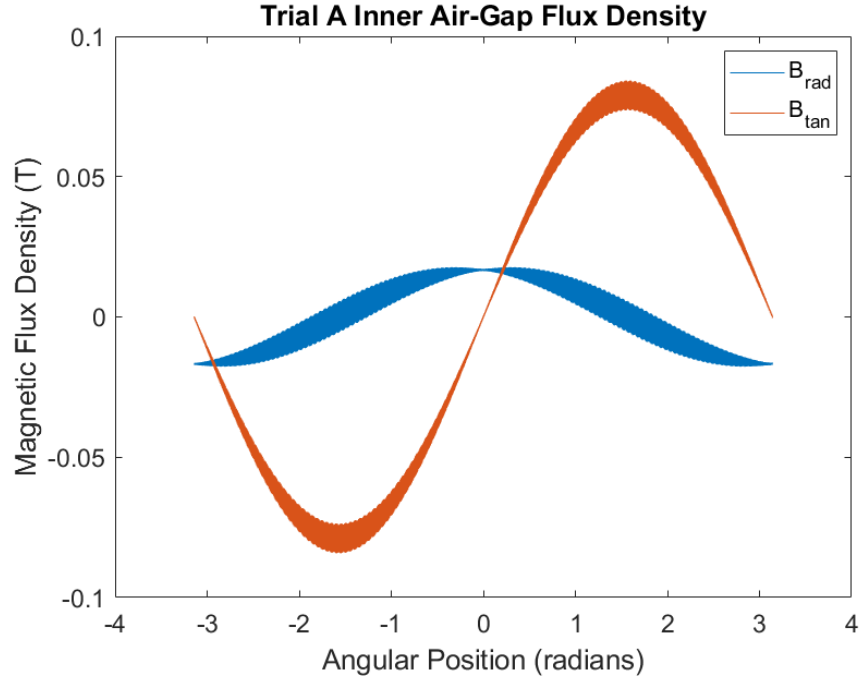


Figure B.4: Radial and tangential flux density waveforms at the inner air gap of Trial A.

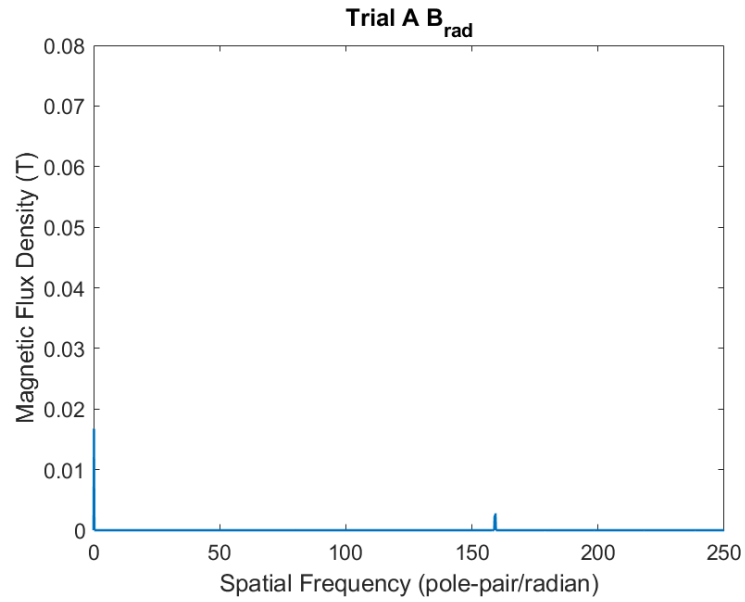


Figure B.5: FFT for the radial flux density waveform of Trial A.

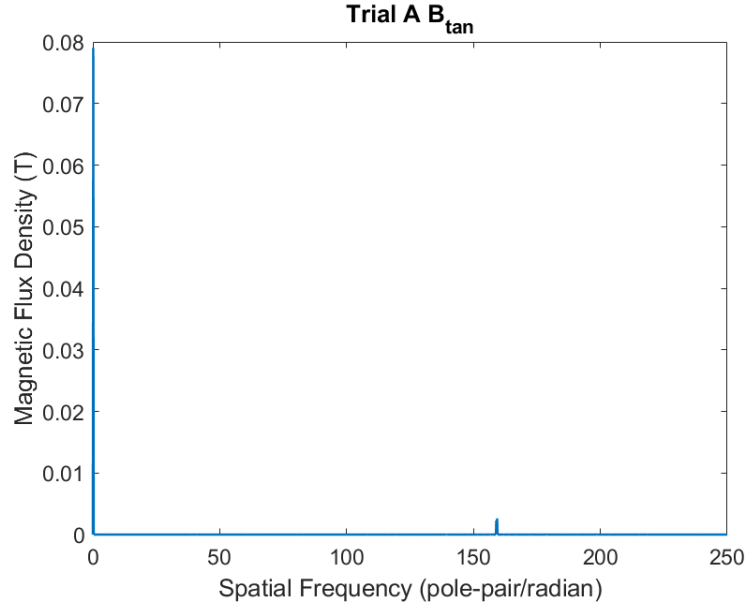


Figure B.6: FFT for the tangential flux density waveform of Trial A.

Figures B.7-B.9 show the flux density waveform and fast Fourier transform (FFT) results for Trial D. It is noted that the high frequency outer rotor harmonic is significantly larger in amplitude for Trial D than Trial A despite being the same distance from the source.

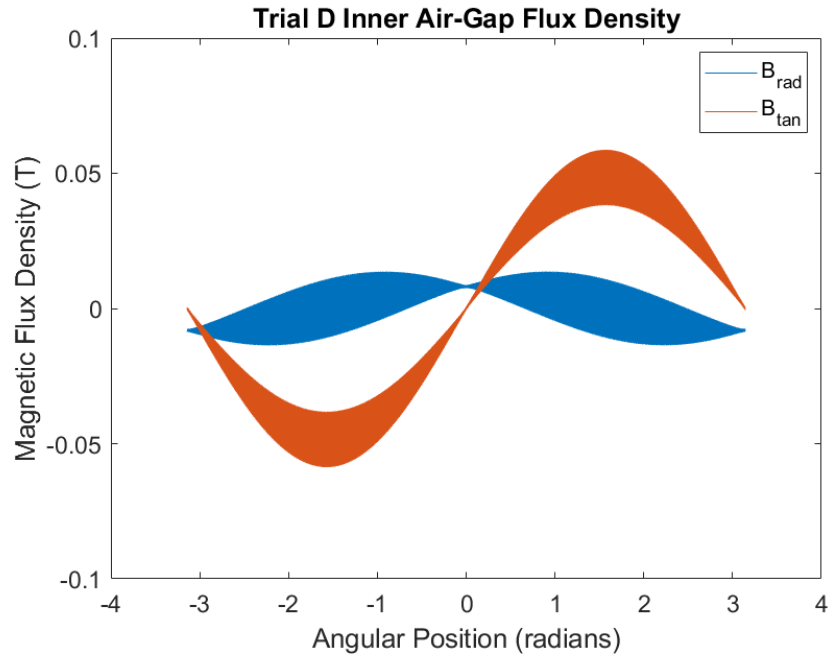


Figure B.7: Radial and tangential flux density waveforms at the inner air gap of Trial D.

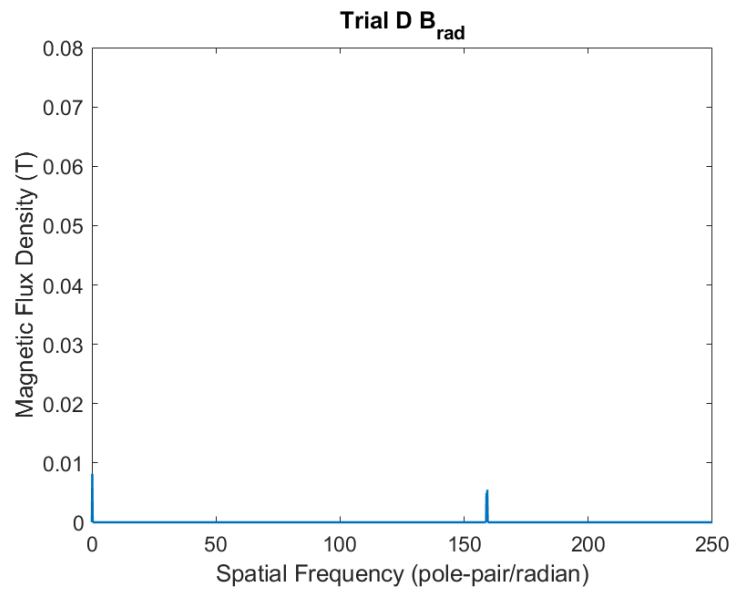


Figure B.8: FFT for the radial flux density waveform of Trial D.



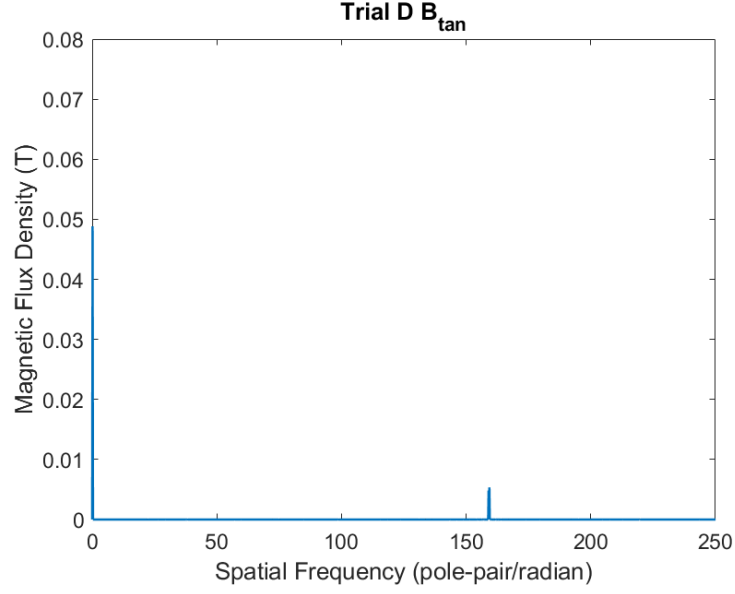


Figure B.9: FFT for the tangential flux density waveform of Trial D.

Table B.2 shows the FFT results for Trials A-D. The table shows that amplitude for both the radial and tangential flux density harmonics decreases as the outer radius decreases. The trials are 2D models and the inner air gap is the same distance from the outer rotor in all trials, so this amplitude decrease can only be attributed to in-plane leakage.

Table B.2: FFT amplitude results for the outer rotor magnets at the inner air gap.

Trial	Outer Diameter (in)	Outer Rotor $B_{rad}$ Amplitude (T)	Outer Rotor $B_{tan}$ Amplitude (T)
A	30.4	0.00242	0.00227
B	40.6	0.00381	0.00368
C	45.7	0.00438	0.00426
D	50.8	0.00492	0.00481

The second design examined by this study is a multi-stage magnetic gear design in which the output of the previous stage becomes the input of the next stage. This topology is shown in Figure B.10 along with the relative torque and angular velocity relationships for each stage.

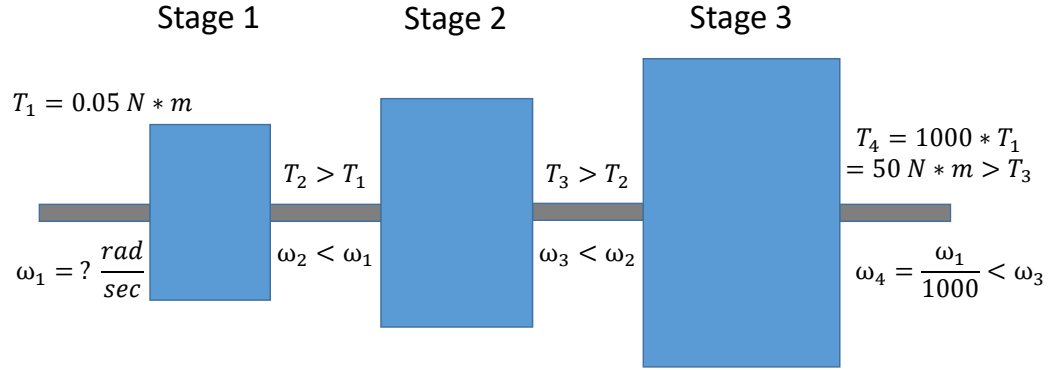


Figure B.10: Torque and angular velocity behavior for a multi-stage magnetic gear with a gear ratio of 1000 that produces 50 N\*m of output torque.

A preliminary 2D study was performed to generate approximate sizes for each stage of a three stage magnetic gear design. The study was performed using multi-stage design theory from Gardener et al. [14]. The results for each of the stages is shown in Table B.3. The outer rotor magnet width is listed because it can be a significant constraint when designing high gear ratio magnetic gears. A higher gear ratio is used for the initial stage because the torque requirement of this stage is very low (1 N\*m). A high gear ratio requires a large number of outer rotor pole-pairs, so the radius of Stage 1 was made relatively large as compared to the axial length to fit the 20 outer rotor pole-pairs. Halbach arrays were not used for this stage because non-Halbach arrays use less magnets, and they were not necessary to meet the torque

requirement of the stage. A low gear ratio was used for Stage 3 because Stage 3 has the strictest torque requirement, and lower gear ratios allow for higher output torque.

Table B.3: Design and performance characteristics for each stage of a 1000 gear ratio, 50 N\*m output torque magnetic gear.

Stage	Gear Ratio	Outer Radius (in)	Axial Length (in)	Outer Rotor Magnet Width (in)	Output Torque (N*m)
1	20	1.02	0.161	$\sim 0.125$	$\sim 1.0$
2	10	1.78	0.898	$\sim 0.250$	$\sim 10$
3	5	1.78	1.70	$\sim 0.250$	$\sim 50$

A 50% torque reduction was applied to all torque results in Table B.3 to approximate the end-effect and Halbach discretization losses. The reasonable axial lengths, outer radii, and outer magnet widths of the three stages shown in Table B.3 indicate that a multi-stage magnetic gear design would be best to achieve a magnetic gear with a gear ratio of 1000 and an output torque of 50 N\*m.

## Appendix C: COMSOL Tutorial: Magnetic Gears

The following appendix serves as a tutorial for the FEM modeling of magnetic gears with the COMSOL AC/DC module. Figure C.1 shows the primary tree of categories to be discussed that define all characteristics of the magnetic gear model.

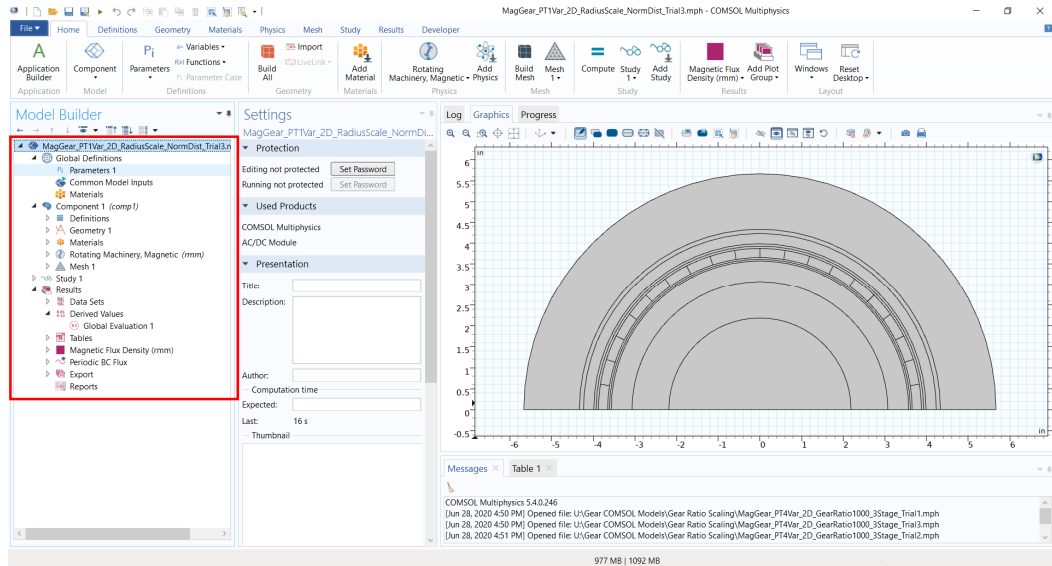


Figure C.1: The tree that defines all geometric, physical, mesh, solver, and post-processing characteristics of a COMSOL magnetic gear model.

Figure C.2 shows the “Parameters” tab. This section should be used to define magnetic gear design variables like outer radius, component thicknesses, pole-pair numbers, etc.

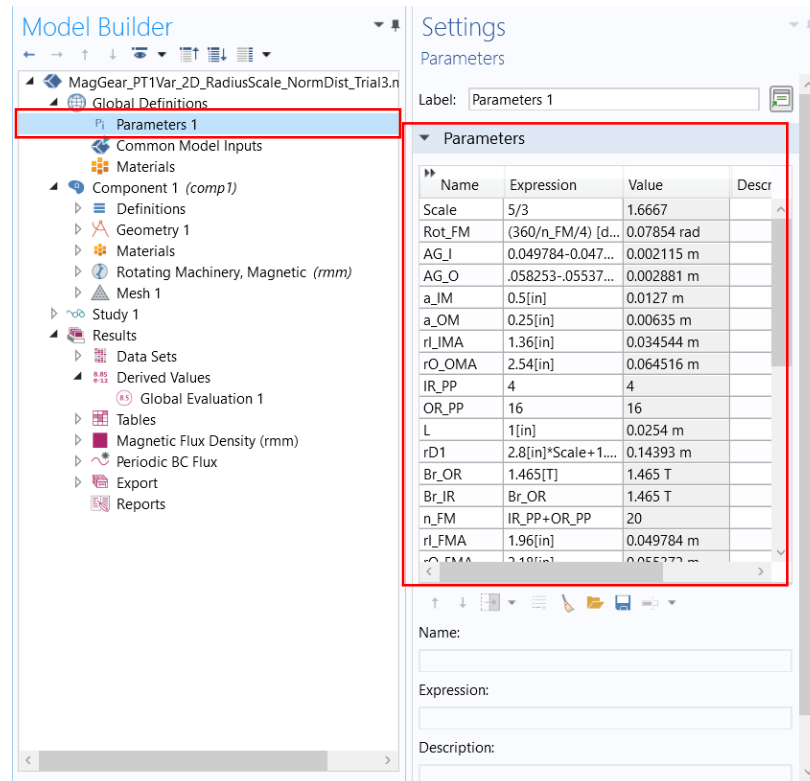


Figure C.2: Parameter tab where magnetic gear design parameters are defined.

The “Definition” tab is used to define coordinate systems and geometric selections that have material and physical properties assigned to them later in the modeling process. These definitions can be made by explicitly selecting the domains or by setting up definitions around certain geometric parameters. Explicit selection is simpler, but can sometimes misidentify regions when design parameters change in a drastic way.

For example, if modulator piece number is changed, the explicit selection often cannot track the new flux modulator domains. Figures C.3-C.5 show three definitions that should be included in all magnetic gear models.

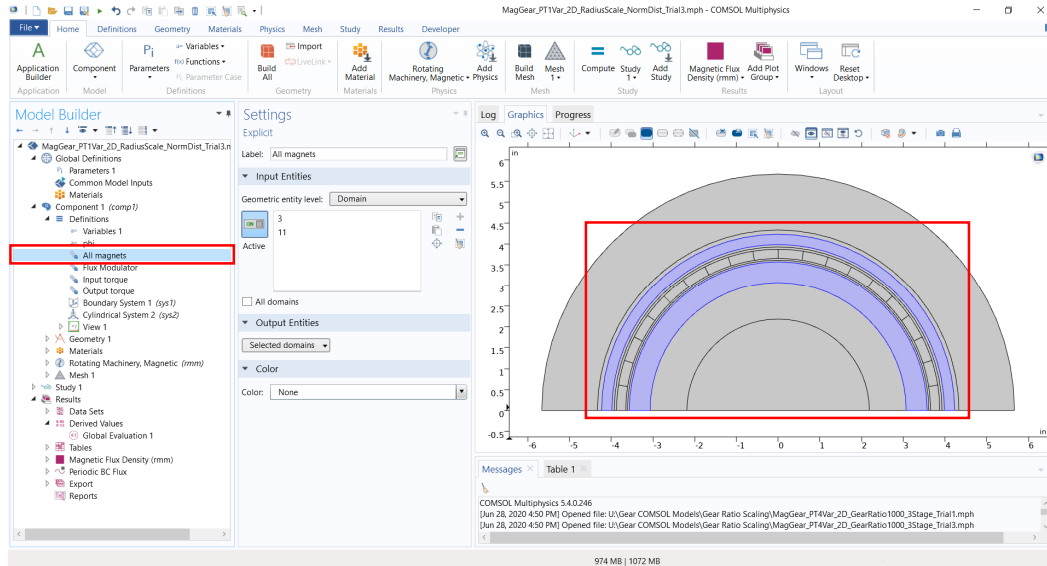


Figure C.3: Explicit definition of “All magnets”.

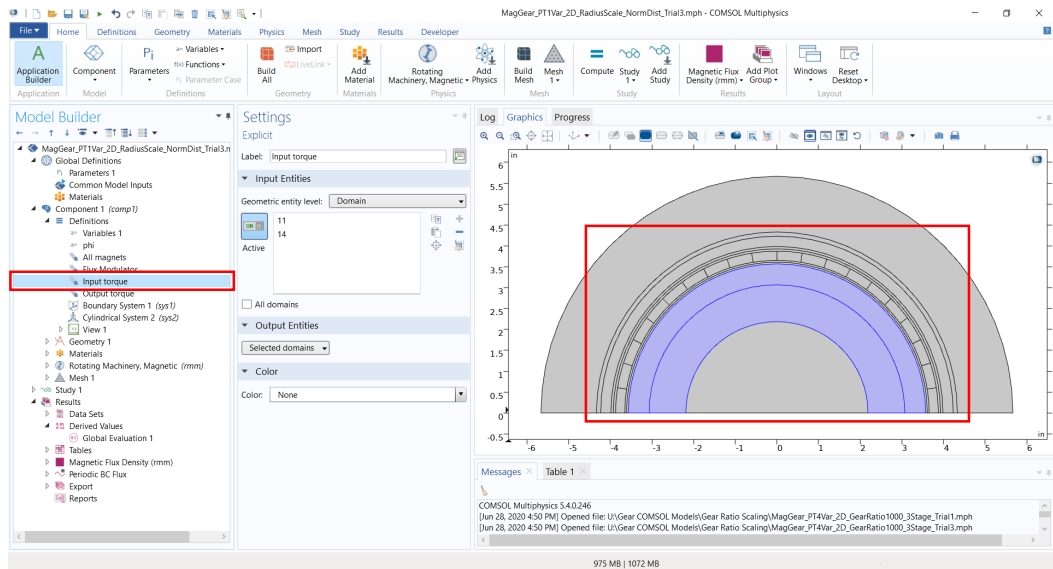


Figure C.4: Explicit definition of the “Input torque” region.

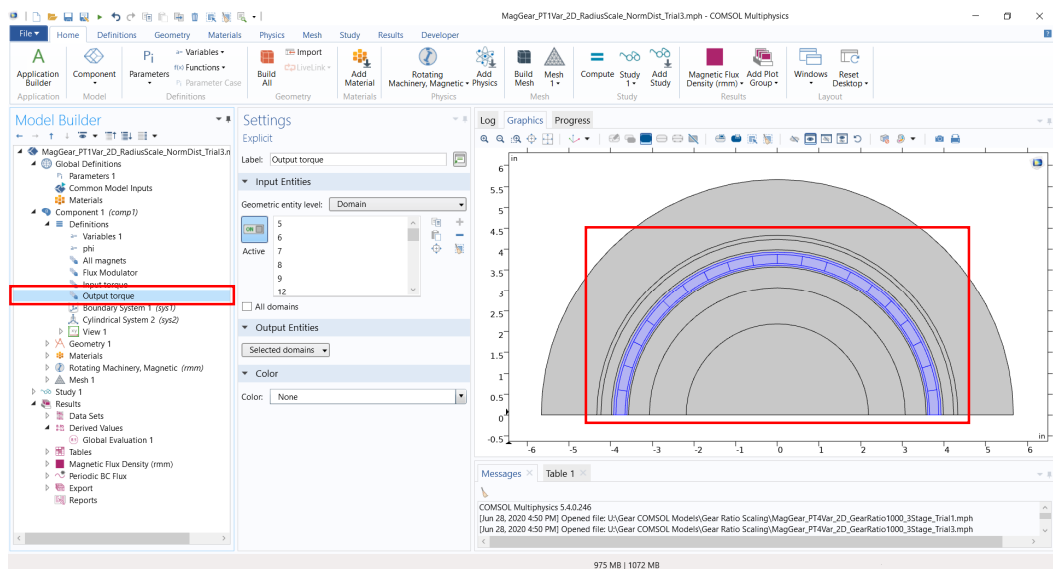


Figure C.5: Explicit definition of the “Output torque” region.

It is helpful to define both a Cartesian and cylindrical coordinate system. Figure C.6 shows the Cartesian coordinate system feature. It is sometimes necessary to define a second coordinate system with a reversed normal vector to assign continuity to a periodic boundary condition.

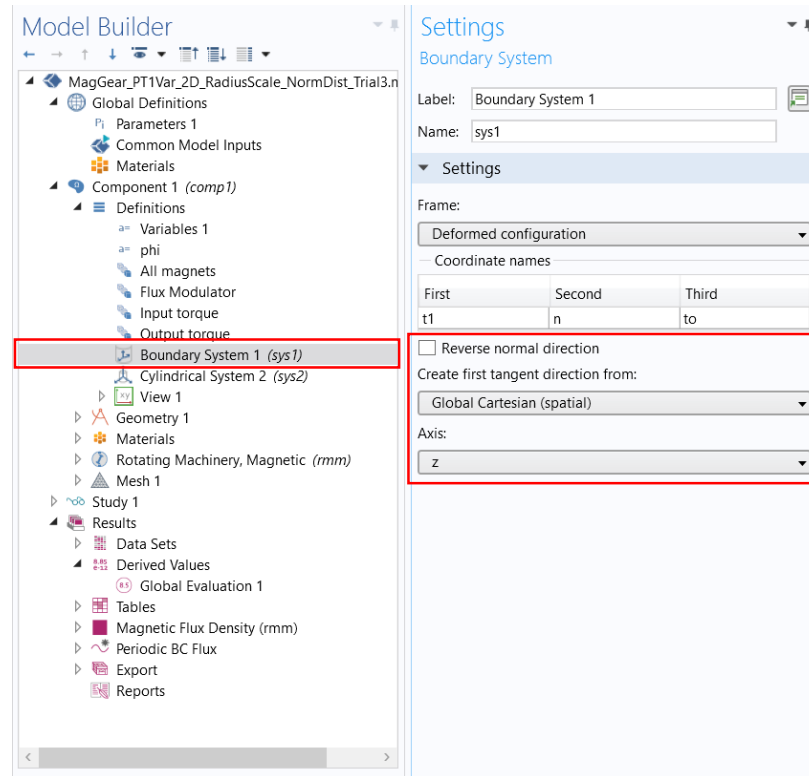


Figure C.6: Definition of a Cartesian boundary system.

The “Geometry” tab is used to establish domains that have different physical and mesh characteristics assigned later in the modeling process. All magnetic gear geometry can be defined using geometric objects and boolean logic. Figure C.7 shows the range function which can be used to step a geometric domain into a circular array.



By checking the “Resulting objects selection” the resulting entity will be available for selection in the material and physics tabs. This is especially useful for the flux modulator pieces because it is exceptionally difficult to consistently define them as a selection in the “Definition” section.

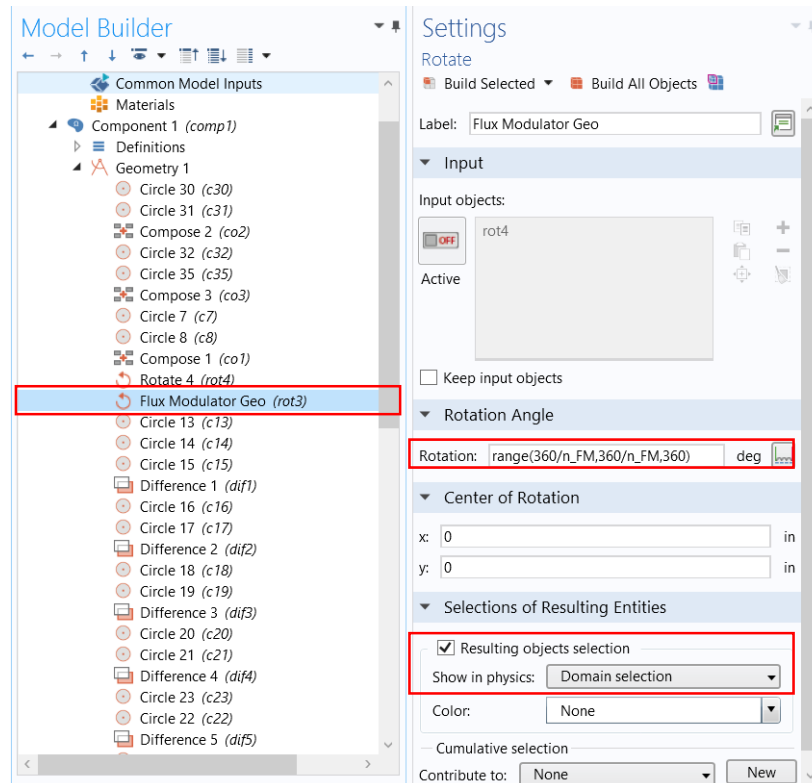


Figure C.7: Command to create a circular array of flux modulator pieces. “Resulting objects selection” is checked to make the resulting object selectable in the material and physics sections.

The “Materials” tab is used to assign material properties to the domains that were defined in the “Geometry” tab. Figure C.8 shows how the entire geometry should

initially be defined as air. The initial air definition will be overridden by later material definitions.

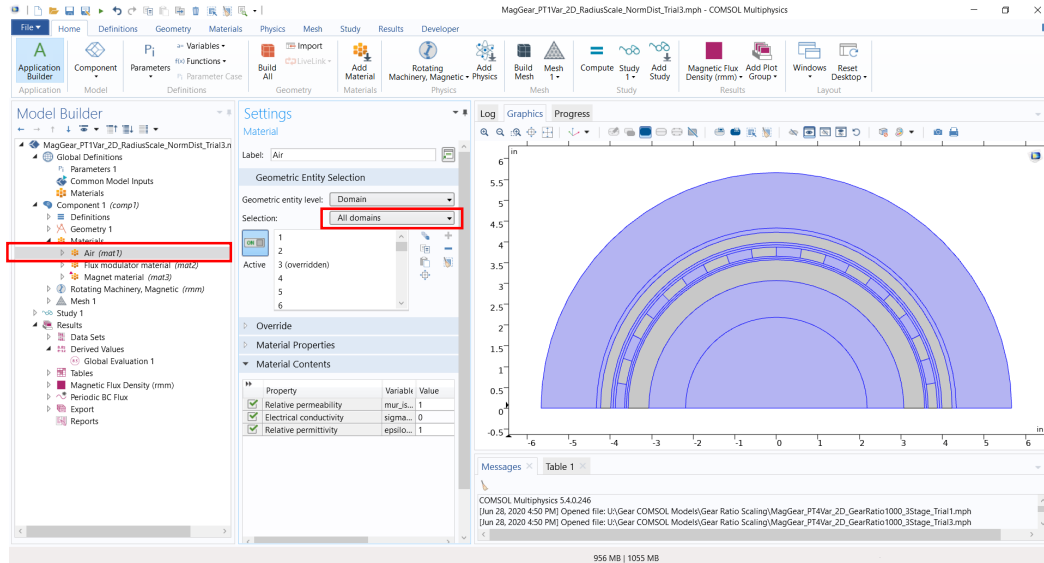


Figure C.8: The entire simulation is initially defined as air.

Figure C.9 shows how the flux modulator domains are assigned the flux modulator material using the selection established in the “Geometry” tab. Figure C.10 provides instruction for assigning the flux modulator material a nonlinear B-H curve.

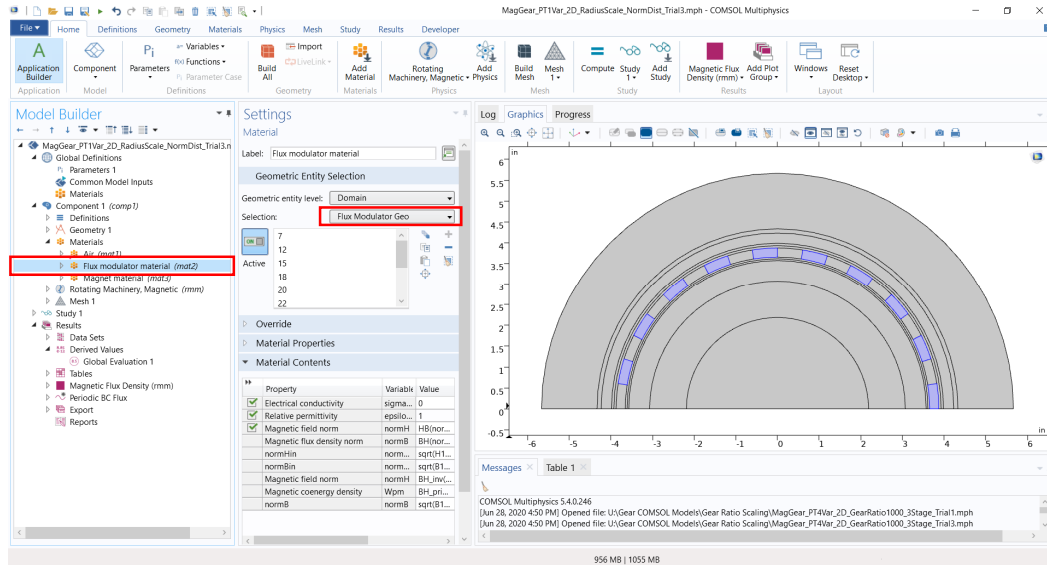


Figure C.9: The flux modulator material is assigned to the flux modulator using the selection defined in the “Geometry tab”. This overrides the initial air definition.

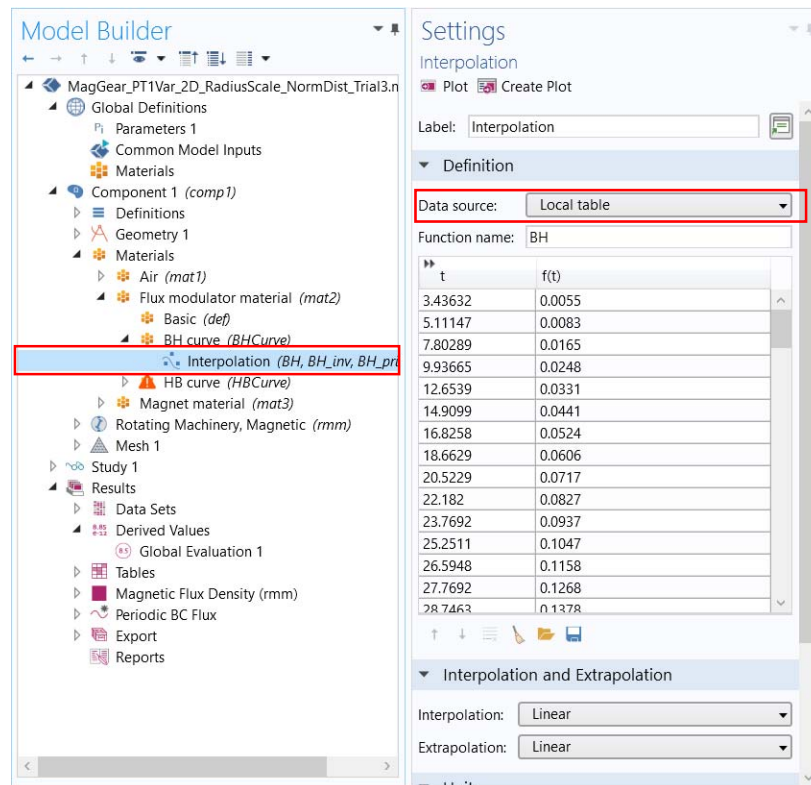


Figure C.10: The B-H curve for flux modulator material is defined using a local table.

The “Rotating Machinery, Magnetic” tab is used to assign magnetic behavior to the domains that were defined in the “Geometry” tab. Figure C.11 identifies where the out-of-plane thickness is assigned for a 2D COMSOL model and where the discretization scheme should be changed to linear for a 3D model.

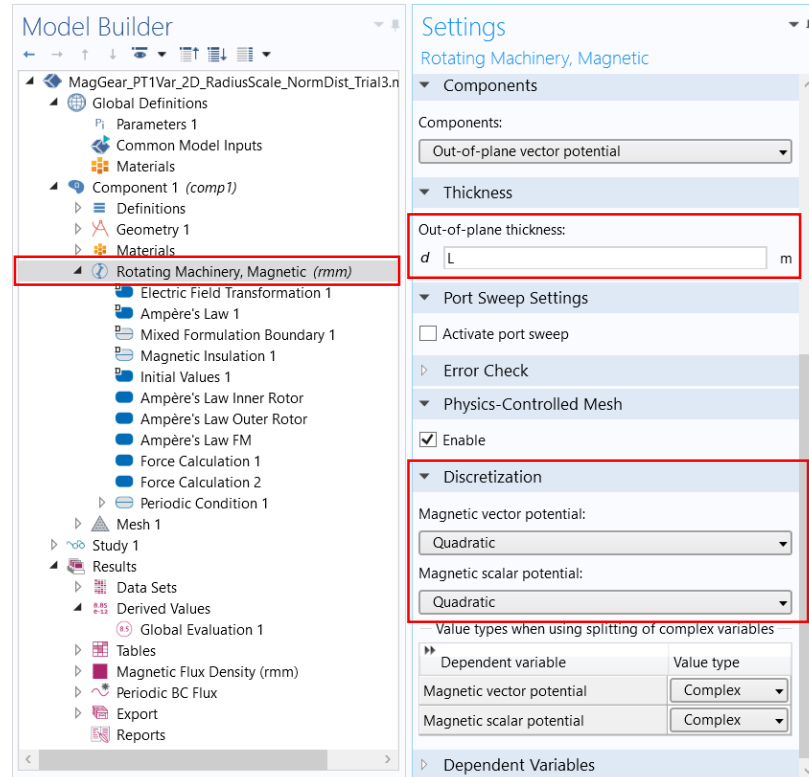


Figure C.11: The out-of-plane thickness and dependent variable discretization scheme is defined.

Figure C.12 shows how permanent magnet material should be assigned magnetic behavior using remanent flux density. Figure C.13 illustrates how the flux modulator material is assigned magnetic behavior in accordance with its material’s B-H curve. Figure C.14 provides an example of the output torque calculation. A separate torque

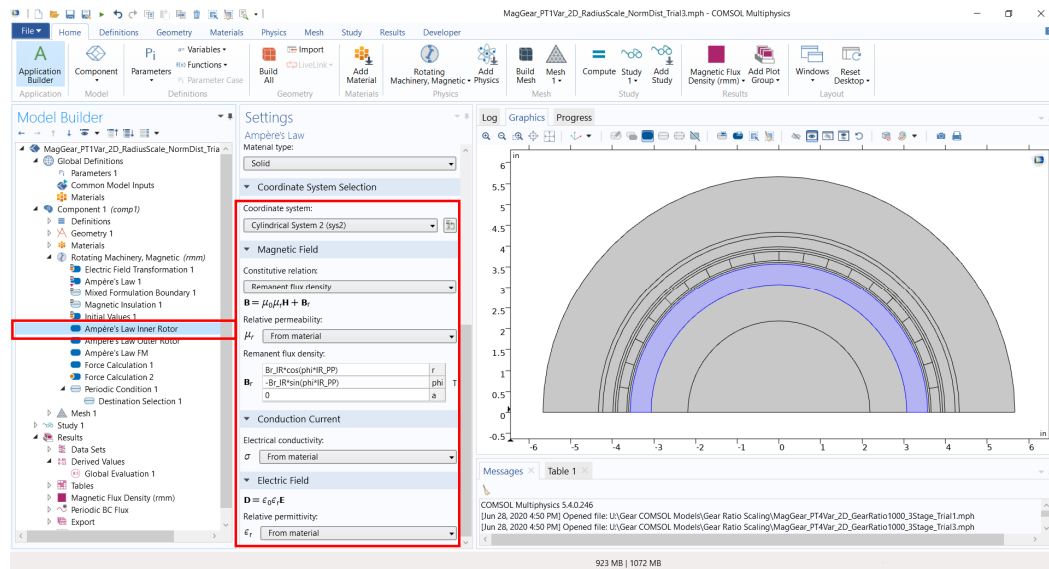


Figure C.12: Ampère's Law is set for the permanent magnets using a remanent flux density vector.

calculation is also applied to the input torque selection. Figure C.15 highlights the periodic boundary condition used to exploit sector symmetry for solution of a smaller magnetic gear model. The highlighted blue face is divided into a source and destination face. Figure C.16 shows the destination face definition. It is noted that the coordinate system used for this face has a flipped normal from the source face to establish continuity.

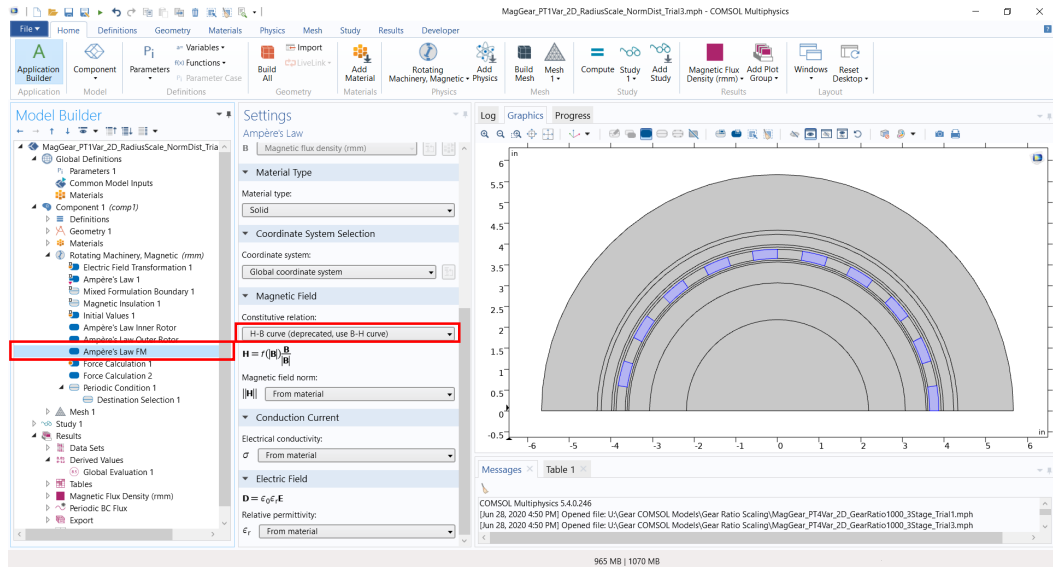


Figure C.13: Ampère's Law is set for the flux modulator pieces using the specified H-B curve.

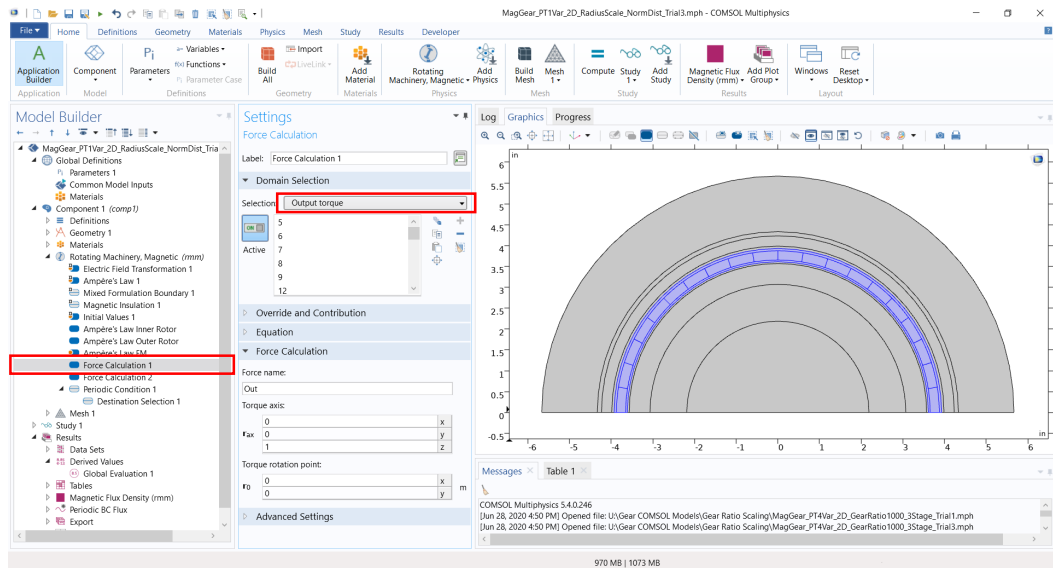


Figure C.14: Torque is calculated at the “Output torque” selection.

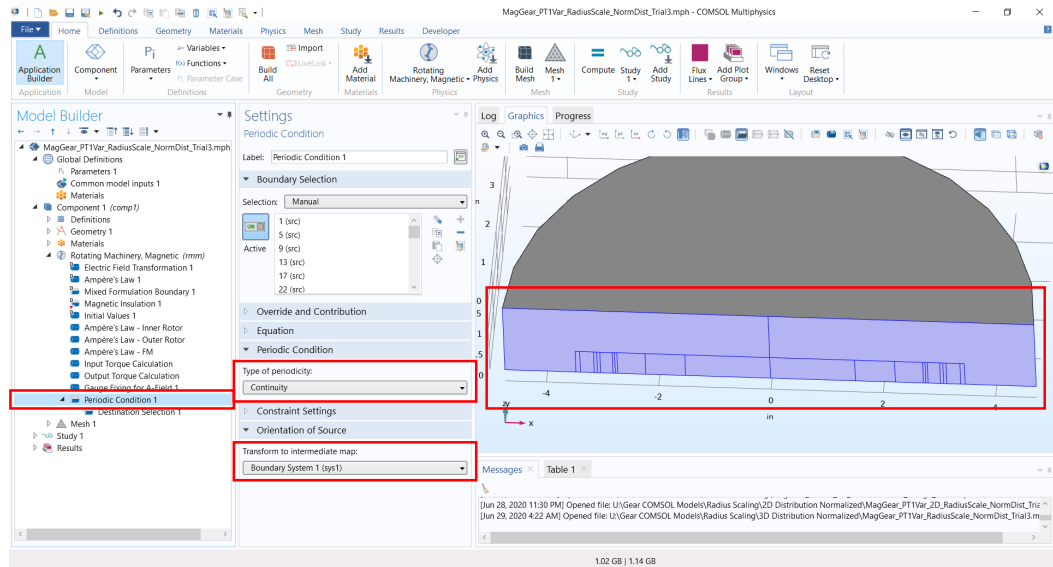


Figure C.15: A continuous periodic boundary condition is defined for a magnetic gear.

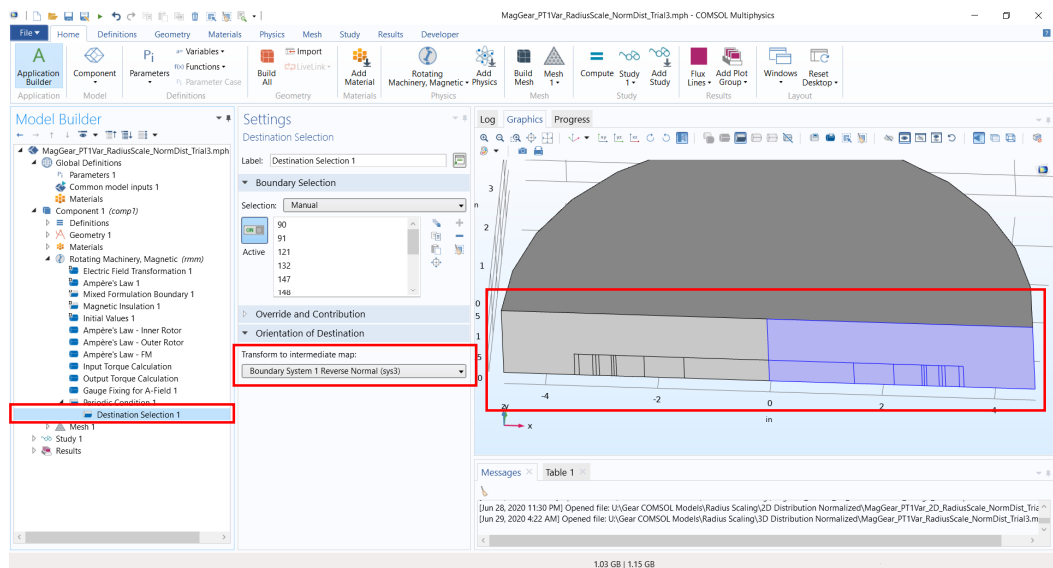


Figure C.16: The destination boundary is explicitly defined and set to use a boundary system with a reversed normal.

The “Mesh” tab is used to divide the domains that were defined in the “Geometry” tab into discrete elements for FEM solution. It is noted that when using a periodic boundary condition, the source and destination faces must have the same mesh. Figure C.17 shows how the “Copy mesh” feature is used to accomplish mesh symmetry.

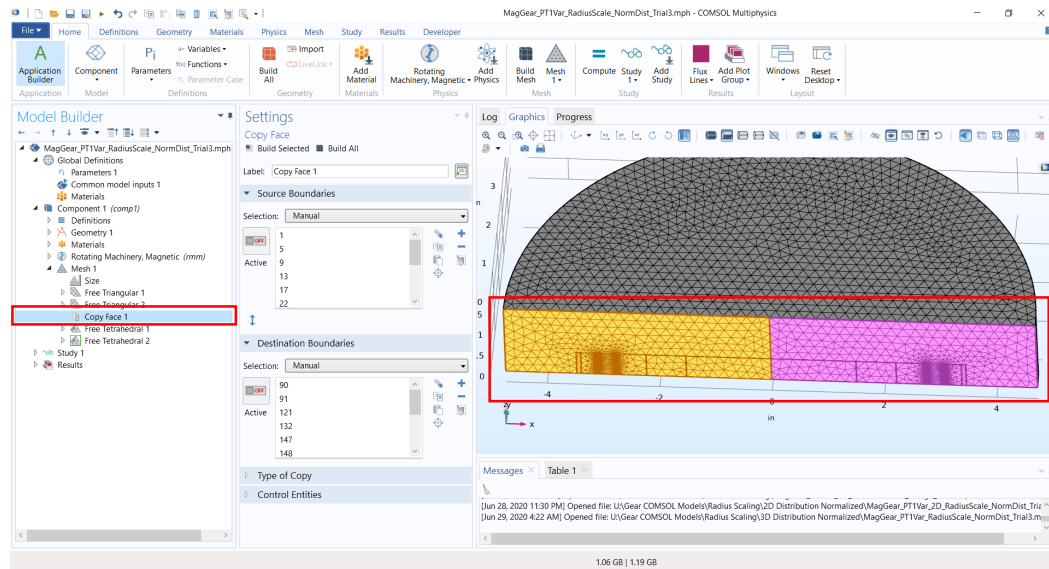


Figure C.17: A mesh is defined on the source boundary and copied to the destination boundary.

It is recommended that most mesh refinement be focused around the air gaps because this is where the flux density behavior is most nonlinear. The mesh should first be defined for the air gaps as in Figure C.18. It is recommended to use the custom element sizing feature to adjust mesh resolution. Figure C.19 establishes a mesh for the rest of the model. By defining the air gap mesh first, this step naturally generates a mesh that decreases in resolution as distance from the air gap increases.



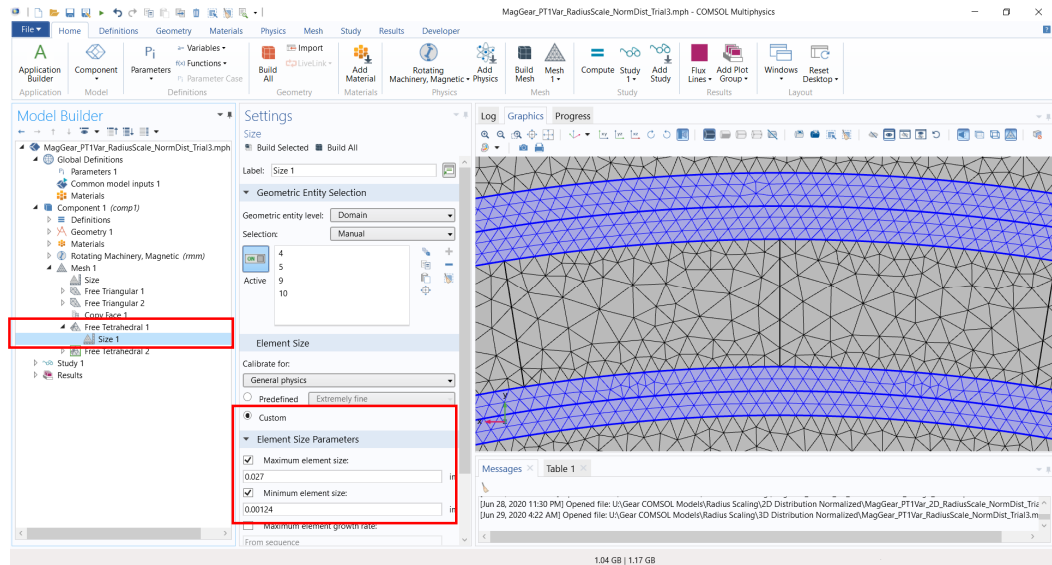


Figure C.18: Tetrahedral mesh resolution is defined for the air gaps.

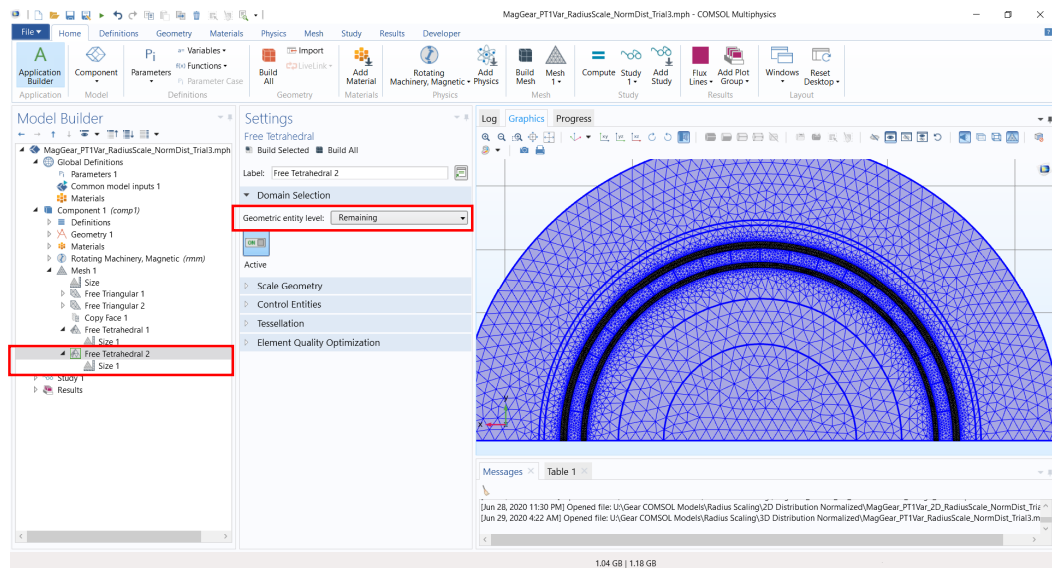


Figure C.19: A tetrahedral mesh is defined for the rest of the model geometry.

The “Study” tab is used to define solver parameters and get degree of freedom (DOF) information as shown in Figure C.20. One must right click on “Compile Equations: Stationary” and select “Statistics” to get a DOF printout for the model.

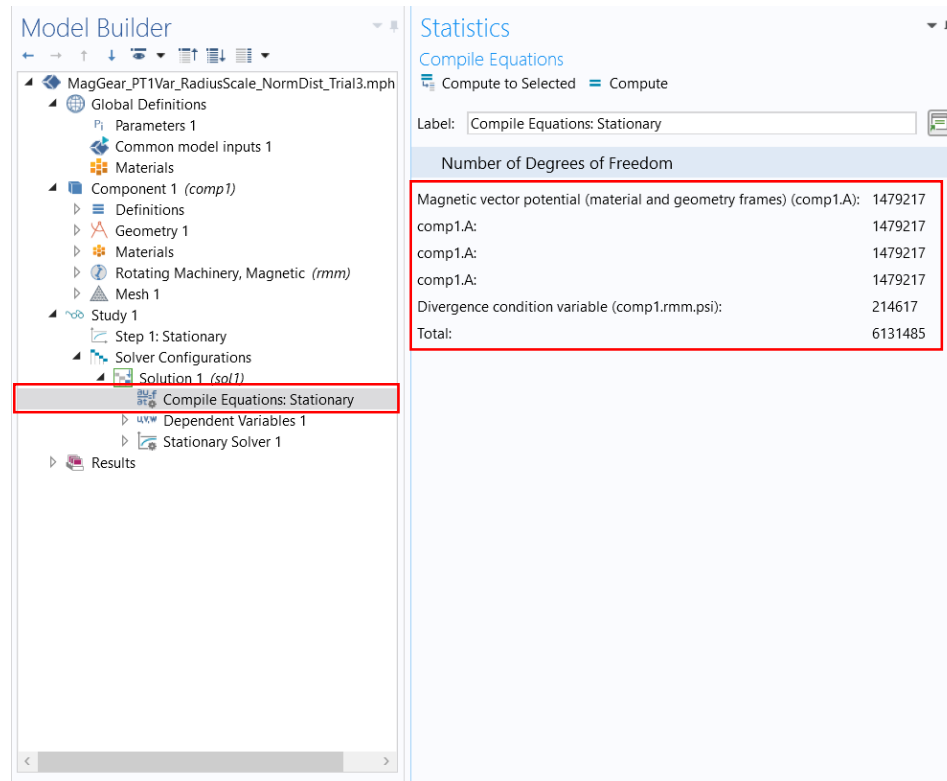


Figure C.20: Statistics of “Compile Equations: Stationary” which show the model DOFs.

Figure C.21 illustrates the parametric sweep that can be set up by right clicking on “Study”.

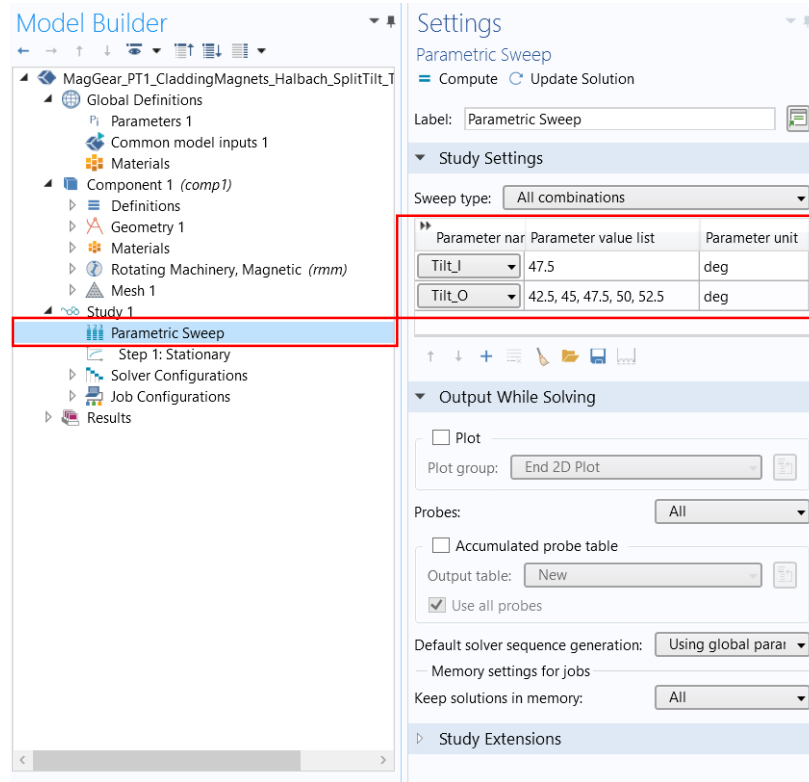


Figure C.21: Parametric sweep of tilt for Study 1.

The “Results” tab is used to post-process data from the model solution. The torque results are shown in Figure C.22. It is noted that the torque variables assigned in the “Rotating Machinery, Magnetic” tab must be scaled by an integer based on the symmetry used in the model.

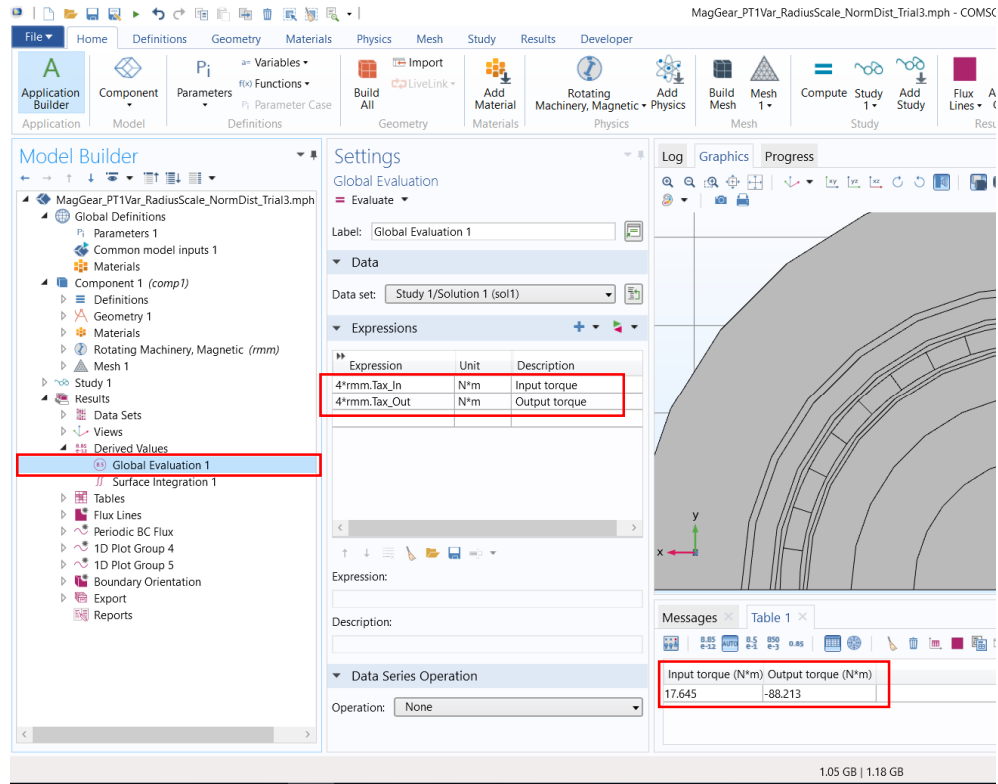


Figure C.22: Global evaluation of input and output torque as defined in the physics section.

Figure C.23 shows the “Data Sets” feature where geometric locations of interest must be defined before solution data can be plotted.

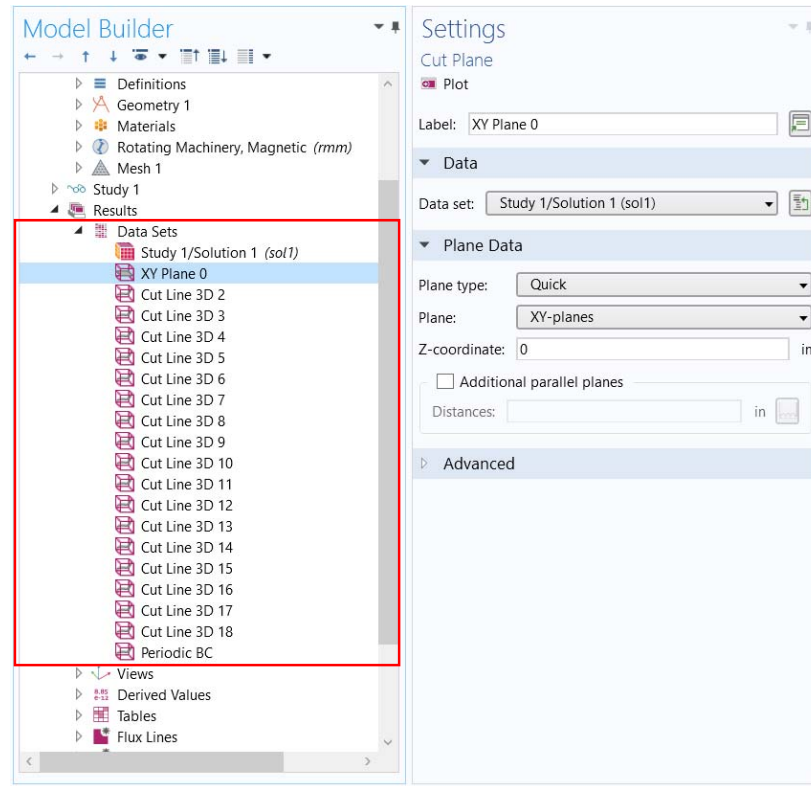


Figure C.23: Geometric locations of interest that have been defined for post-processing.

One of the most necessary plots to understanding magnetic behavior of the gear is the flux density arrow surface plot. This type of plot is displayed by Figure C.24. Flux components can also be plotted on a simple line graph as in Figure C.25.

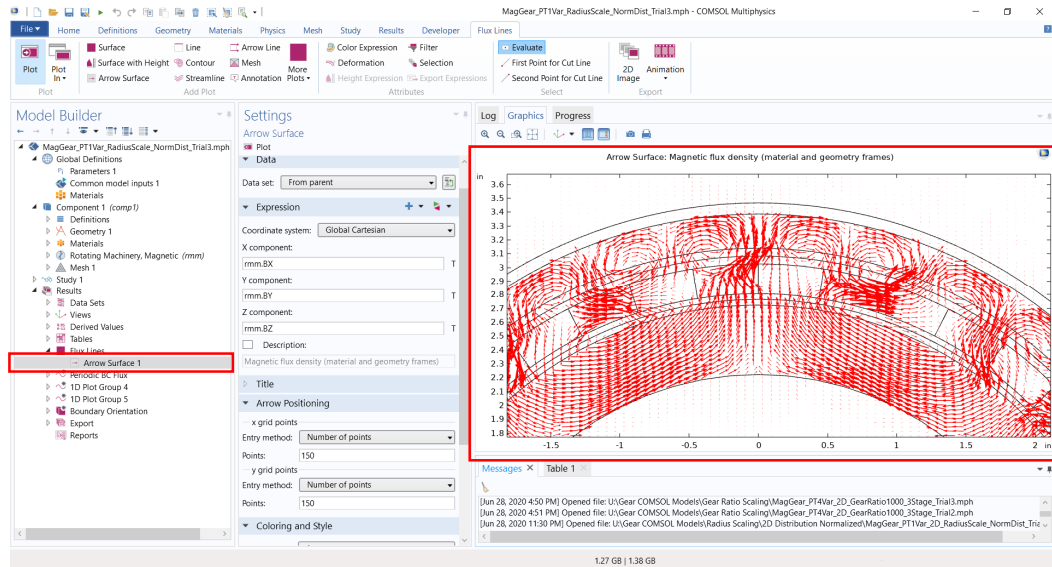


Figure C.24: Arrow surface of a plane to visualize flux lines.

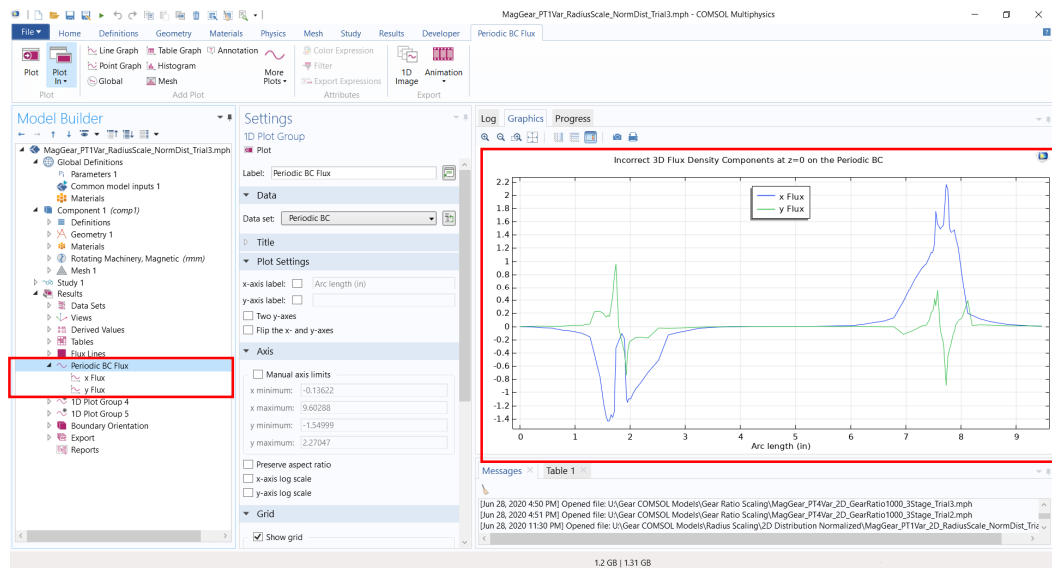


Figure C.25: Line graph of flux components at the periodic boundary condition.

Figure C.26 provides a way to visual the coordinate systems being used by boundaries of the gear. This tool is especially helpful when using the periodic boundary condition to ensure that coordinate systems of the source and destination boundaries have continuity. Figure C.27 shows the tool to be used when exporting raw data from the model.

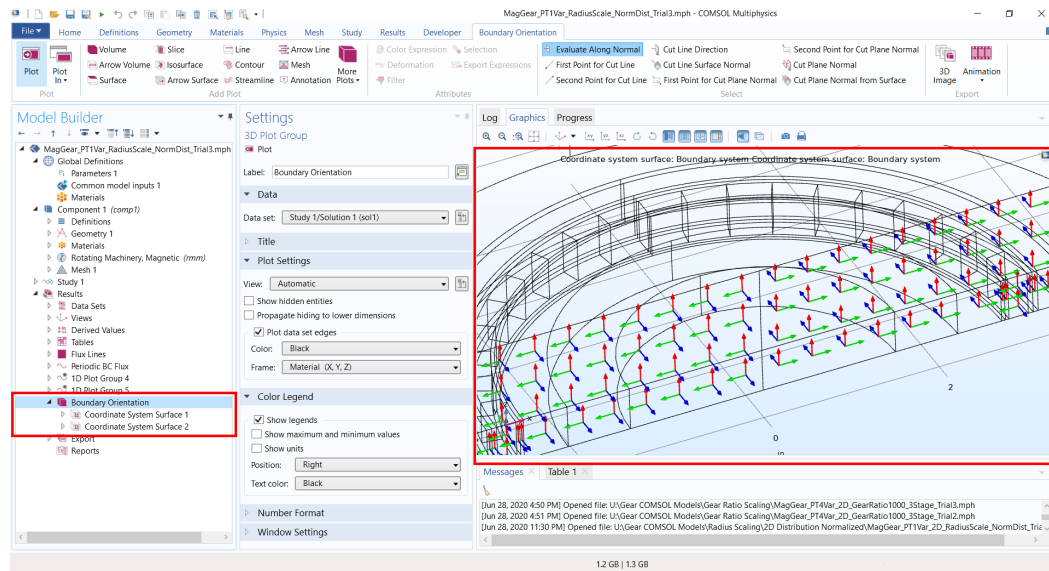


Figure C.26: Boundary systems used at the source and destination faces of the periodic boundary condition.

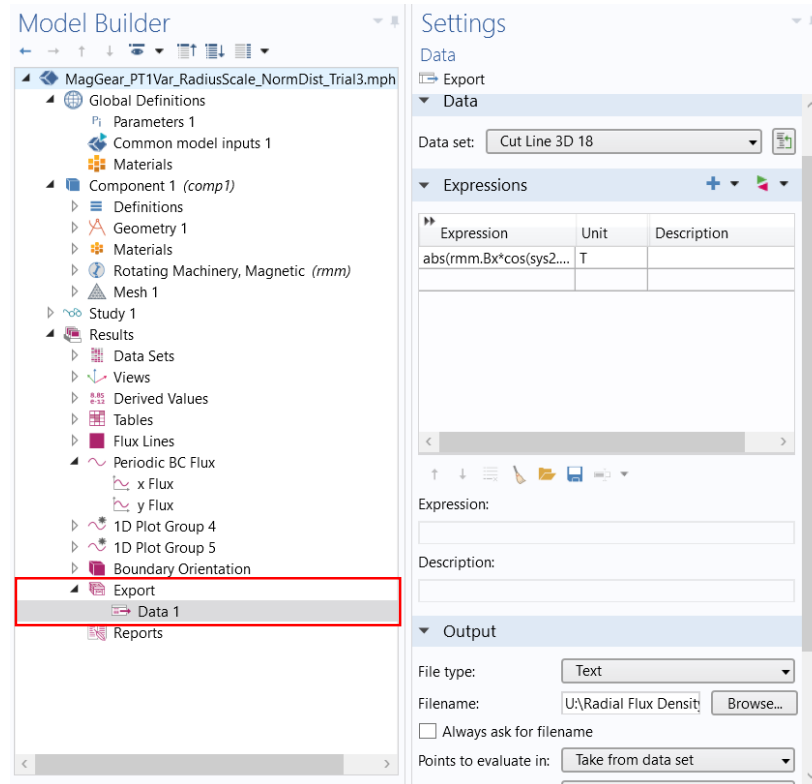


Figure C.27: Export feature used to extract raw data from the COMSOL simulation.



## Bibliography

- [1] C. G. Armstrong. Power transmitting device, u.s. pat. 687 292, 1901.
- [2] V. Asnani, J. Scheidler, and T. Tallerico. Magnetic gearing research at nasa. In *AHS Int. 74th Annual Forum*, Phoenix, AZ, 2018.
- [3] K. Atallah and D. Howe. A novel high-performance magnetic gear. *IEEE Transactions on Magnetics*, 37(4):2844–2846, 2001.
- [4] K. Atallah, J. Rens, S. Mezani, and D. Howe. A novel “pseudo” direct-drive brushless permanent magnet machine. *IEEE Transactions on Magnetics*, 44(11):4349–4352, 2008.
- [5] C. A. Balanis. *Advanced Engineering Electromagnetics*. Don Fowley, second edition, 2012.
- [6] R. Bjørk, C. R. H. Bahl, A. Smith, and N. Pryds. Optimization and improvement of halbach cylinder design. *Journal of Applied Physics*, 104(1):013910, 2008.
- [7] What does degrees of freedom (dofs) mean in comsol multiphysics? <https://www.comsol.com/support/knowledgebase/875>.
- [8] COMSOL Multiphysics, Stockholm, Sweden. *AC/DC Module User’s Guide*, v. 5.4. comsol ab edition, 2018.
- [9] Z. Deng, I. Nas, and M. J. Dapino. Torque analysis in coaxial magnetic gears considering nonlinear magnetic properties and spatial harmonics. *IEEE Transactions on Magnetics*, 55(2):1–11, 2019.
- [10] D. J. Evans and Z. Q. Zhu. Influence of design parameters on magnetic gear’s torque capability. In *2011 IEEE International Electric Machines Drives Conference (IEMDC)*, pages 1403–1408, 2011.
- [11] N. W. Frank and H. A. Toliyat. Gearing ratios of a magnetic gear for wind turbines. In *2009 IEEE International Electric Machines and Drives Conference*, pages 1224–1230, 2009.

- [12] W. Frei. How much memory is needed to solve large comsol models?, 2014. <https://www.comsol.com/blogs/much-memory-needed-solve-large-comsol-models/>.
- [13] B. Funieru and A. Binder. Simulation of electrical machines end effects with reduced length 3d fem models. In *2012 XXth International Conference on Electrical Machines*, pages 1430–1436, 2012.
- [14] M. C. Gardner, M. Johnson, and H. A. Toliyat. Analysis of high gear ratio capabilities for single-stage, series multistage, and compound differential coaxial magnetic gears. *IEEE Transactions on Energy Conversion*, 34(2):665–672, 2019.
- [15] S. Gerber. *Evaluation and Design Aspects of Magnetic Gears and Magnetically Geared Electrical Machines*. PhD thesis, Stellenbosch University, 2015.
- [16] S. Gerber and R. Wang. Analysis of the end-effects in magnetic gears and magnetically geared machines. In *2014 International Conference on Electrical Machines (ICEM)*, pages 396–402, 2014.
- [17] E. Gouda, S. Mezani, L. Baghli, and A. Rezzoug. Comparative study between mechanical and magnetic planetary gears. *IEEE Transactions on Magnetics*, 47(2):439–450, 2011.
- [18] K. Halbach. Design of permanent multipole magnets with oriented rare earth cobalt material. In *Nuclear Instruments and Methods*, volume 169, 1980.
- [19] H. Leupold and E. Potenziani. Novel high-field permanent-magnet flux sources. *IEEE Transactions on Magnetics*, 23(5):3628–3629, 1987.
- [20] L. Liu. What is the curl element (and why is it used)?, 2019. <https://www.comsol.com/blogs/what-is-the-curl-element-and-why-is-it-used/>.
- [21] J. Mallinson. One-sided fluxes – a magnetic curiosity? *IEEE Transactions on Magnetics*, 9(4):678–682, 1973.
- [22] T. B. Martin. Magnetic transmission, u.s. pat. 3 378 710, 1968.
- [23] B. McGilton, M. Mueller, and A. McDonald. Review of magnetic gear technologies and their applications in marine energy. In *5th IET International Conference on Renewable Power Generation (RPG) 2016*, pages 1–6, 2016.
- [24] E. Potenziani, J. P. Clarke, and H. A. Leupold. The production of laminar fields with permanent magnets. *Journal of Applied Physics*, 61(8):3466–3467, 1987.
- [25] J. Scheidler, Z. Cameron, and T. Tallerico. Dynamic testing of a high-specific-torque concentric magnetic gear. In *VFS 75th Annual Forum*, Philadelphia, PA, 2018.

- [26] J. J. Scheidler, V. M. Asnani, and T. F. Talerico. Nasa’s magnetic gearing research for electrified aircraft propulsion. In *2018 AIAA/IEEE Electric Aircraft Technologies Symposium (EATS)*, pages 1–12, 2018.
- [27] T. F. Talerico, Z. A. Cameron, and J. J. Scheidler. Design of a magnetic gear for nasa’s vertical lift quadrotor concept vehicle. In *2019 AIAA/IEEE Electric Aircraft Technologies Symposium (EATS)*, pages 1–21, 2019.
- [28] G. Wimmer, M. Clemens, and J. Lang. Calculation of magnetic fields with finite elements. *From Nano to Space: Applied Mathematics Inspired by Roland Bulirsch*, pages 111–124, 2008.
- [29] C. Xia, L. Guo, and H. Wang. Modeling and analyzing of magnetic field of segmented halbach array permanent magnet machine considering gap between segments. *IEEE Transactions on Magnetics*, 50(12):1–9, 2014.
- [30] Y. D. Yao, D. R. Huang, C. M. Lee, S. J. Wang, D. Y. Chiang, and T. F. Ying. Magnetic coupling studies between radial magnetic gears. *IEEE Transactions on Magnetics*, 33(5):4236–4238, 1997.
- [31] L. Zhu, N. Li, and P.R.N. Childs. Lightweighting in aerospace component and system design, 2019. <https://www.techbriefs.com/component/content/article/tb/pub/features/articles/33914>.